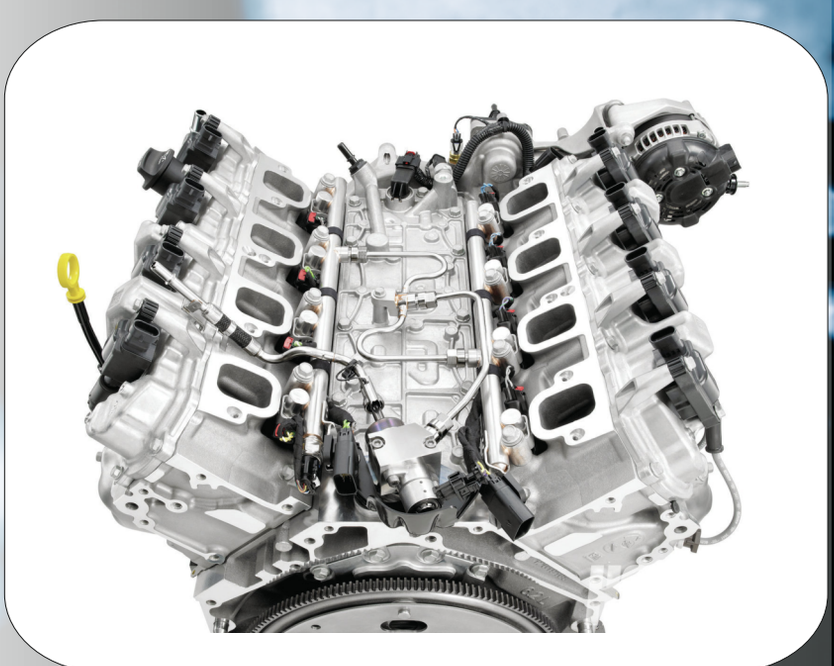
International virtual journal for science, technics and innovations for the industry

# MTM

# MACHINES TECHNOLOGIES MATERIALS

YEAR VIII Issue 11 / 2014 ISSN 1313-0226



Published by
Scientific technical
Union of Mechanical Engineering

# MACHINES, TECHNOLOGIES, MATERIALS

## INTERNATIONAL VIRTUAL JOURNAL

PUBLISHER

## SCIENTIFIC TECHNICAL UNION OF MECHANICAL ENGINEERING

108, Rakovski Str., 1000 Sofia, Bulgaria
**tel.** (+359 2) 987 72 90,
**tel./fax** (+359 2) 986 22 40**,**
journal@mech-ing.com,
www.mech-ing.com/journal

**ISSN 1313-0226**
**YEAR VIII ISSUE 11 / 2014**



### EDITORIAL BOARD

**Editor-in-chief**: Prof. Dr. Mitko Mihovski – Chairman of the Scientific Council of the STUnion of Mechanical Engineering

**AKADEMIC CONCEPTIONAL BOARD**
Acad. Vassil Sgurev
Acad Yachko Ivanov
Acad Vladimir Klyuev
Acad. Rivner Ganiev
Corr. mem. Georgi Mladenov
Corr. mem. Dimitar Buchkov
Corr. mem. Stefan Hristov
Corr. mem. Venelin Jivkov
Corr. mem. Anatoliy Kostin
Corr. mem. Edward Gorkunov

**EDITORIAL COUNCIL**
Prof. D.Sc. Georgi Popov
Prof. D.Sc. Alexander Skordev
Prof. D.Sc. Nikola Rashkov
Prof. D.Sc. Dimitar Stavrev
Prof. D.Sc. Hristo Shehtov
Prof. Dr. Todor Neshkov
Prof. Dr. Dimitar Damianov
Prof. Dr. Kiril Arnaudov
Prof. Dr. Snejana Grozdanova
Prof. Dr. Vassil Georgiev
Assoc. Prof. Lilo Kunchev

### EDITORIAL BOARD – EXPERTS AND REVIEWERS

**FROM BULGARIA**
Prof. D.Sc. Nyagol Manolov
Prof. D.Sc. Vitan Galabov
Prof. D.Sc. Emil Momchilov
Prof. D.Sc. Emil Marinov
Prof. D.Sc. Dimitar Katzov
Prof. D.Sc. Stavri Stavrev
Prof. D.Sc. Georgi Raychevski
Prof. D.Sc. Ivan Yanchev
Prof. D.Sc. Marin Stoychev
Prof. D.Sc. Roman Zahariev
Prof. D.Sc. Vassil Mihnev
Prof. D.Sc. Valentin Abadjiev
Assoc. Prof. Dimitar Stanchev
Assoc. Prof. Milcho Angelov
Assoc. Prof. Mihail Mihovski
Assoc. Prof. Radi Radev
Assoc. Prof. Georgi Todorov
Assoc. Prof. Simeon Petkov
Assoc. Prof. Petar Dobrev
Assoc. Prof. Nikolay Piperov

**FOREIGN MEMBERS**
PD. D. PE Assoc. Prof D.Midaloponlas
Prof. Dr. Athanasios Mihaildis
Prof. Amos Notea
Prof. Dr. Eng. Airon Kubo
Prof. Dr. Eng Georg Dobre
Prof. Dr. Dimitrov Dimitar
Prof. Dr. Mohora Cristina
Prof. Dr. Popa Marcel
Prof. Dr. Sobczak Jerzy
Prof. Dr. Tamosiuniene Rima
Prof. Alexander Dimitrov
Prof. dr. Marian Tolnay
Prof. dr. Mikolas Hajduk


The current issue and the first issue of journal and the conditions for publication can be find on www.mech-ing.com/journal

# CONTENTS

**ADVANCED DESIGN AND TECHNOLOGY FOR PRODUCTION OF SENSOR ELEMENTS IN DEVICES BASED ON SURFACE PLASMON RESONANCE**
Maslov V.P., G.V. Dorozinsky ..... 3

**PLASMA SURFACE TECHNOLOGY PROMOTING CAPILLARY IMPREGNATION OF WOOD: XPS ANALYSIS OF DIFFERENT PLASMA PRE-TREATED WOOD SURFACES**
Ivanov I., D. Gospodinova, P. Dineff, L. Veleva ..... 7

**INFLUENCE OF THE POSITION OF THE SWASH PLATE ROTATION AXIS ON THE VOLUMETRIC EFFICIENCY OF THE AXIAL PISTONS PUMPS**
Zaluski P. ..... 12

**MODELING AND OPTIMIZATION OF THE PROPERTIES AND COMPOSITION OF TITANIUM-BASED ALLOYS**
Tontchev N., Y. Kalev, R. Lazarova ..... 16

**INTELLIGENT DECISION-MAKING FOR ENERGY AND ECONOMIC EFFICIENCY OF INNOVATIVE MANUFACTURING PROCESSES BASED ON MULTI-ATTRIBUTE KEY PERFORMANCE INDICATORS**
Grzelak D., R.Freund, H. Wiemer, K. Großmann ..... 20

**INVESTIGATION OF MECHANICAL PROPERTIES OF TITANIUM ALLOYS BASED ON GENETIC OPTIMIZATION AND PARETO FRONT**
Ivanov M., N. Tontchev ..... 24

**SOFWARE MODEL FOR SELECTION OF THE APPROPRIATE CHEMICAL COMPOSITION OF TITANIUM ALLOYS UNDER DEFINES REQUIREMENTS FOR MECHANICAL CHARACTERISTICS**
Ivanov M., N. Tontchev ..... 27

**THERMAL STRESSES IN THE BLADES WITH AND WITHOUT TBC BASED ON THE TEMPERATURE DISTRIBUTIONS MEASURED USING THERMAL IMAGING CAMERA**
Maś K., M. Woźny, S. Dudek, M. Marchewka, D. Płoch, W. Bochnowski,.E. M. Sheregii ..... 31

**APPLICATION OF EA SIGNAL TO EVALUATE THE DEGRADATION OF X6CrNiTi18-10 STEEL DURING TENSILE TEST**
Bochnowski W., A. Dziedzic, S Adamiak, E. Szeregij ..... 34

**PVD DEPOSITION OF HAFNIUM IN ALUMINIDE COATINGS**
Romanowska J. ..... 38

**CVD AND EB-PVD AS A METHODS OF THE ZIRCONIUM INTRODUCING TO THE ALUMINIDE COATINGS**
Zagula-Yavorska M., J. Sieniawski ..... 42

**THE TERMOGRAPHIC ANALYSIS OF THE WELDING BY TIG**
Maś K., M. Woźny, M. Marchewka, D. Płoch, E. M. .Sheregii ..... 46

**THE SCANING NOZZLE HOT AIR SYSTEM FOR THERMOGRAPHIC DETECTION OF THE SURFACE INCORPORATED HIDDEN DEFECTS**
Prokhorenko S., K. Maś, M. Woźny, E. M. Sheregii ..... 49

**BELT CONVEYOR DESIGN AND ANALYSIS**
Gerdemeli İ., S. Kurt, E. T. Dayan ..... 52

**LATTICE (CAGE) BEAM DESIGN AND FINITE ELEMENT ANALYSIS OF GANTRY CRANE**
Gerdemeli İ., S. Kurt, B. Bige ..... 56

# ADVANCED DESIGN AND TECHNOLOGY FOR PRODUCTION OF SENSOR ELEMENTS IN DEVICES BASED ON SURFACE PLASMON RESONANCE

Doc.Sc. Maslov V.P., Phd-student Dorozinsky G.V.
V. Ye. Lashkaryov Institute of Semiconductor Physics, National Academy of Sciences of Ukraine, Kiev, Ukraine

vladmaslov@mail.ru, gvdorozinsky@isp.kiev.ua

**Abstract:** *Results of researches are showed, that fabrication technology of sensor elements are used in devices based on surface plasmon resonance significantly affects on the increasing uptime of measuring and substantially increases the sensitivity to low concentrations of analytes. The results of investigations have shown that deposition of plasmonexciting metal layer on glass substrate at the chosen angle enables to enhance sensitivity of the surface plasmon resonance sensor by 1.5 times for liquid media and 2 times for gas-like media as compared with standard gold chips as well as improve uniformity of deposition and durability of ligand binding to the sensitive layer. Diagnostic facilities based on surface plasmon resonance possess a high sensitivity to low concentrations of studied substances, which enables one to use them as precise analytical devices in lab investigations in industry, agriculture, medicine, and ecology.*

**Keywords**: SURFACE PLASMON RESONANCE, NANOTECHNOLOGY, SENSOR ELEMENT, PRECISE ANALYTICAL DEVICES

## *1. Introduction*

The *objective*s of the research are advanced sensor elements, their production technology and their sensor properties for use in devices based on surface plasmon resonance for accurate measurements. Optical measurements are based on the phenomenon of surface plasmon resonance (SPR) is widely used for chemical and biological analyzes based on detection of adsorption of gaseous or liquid media. Surface plasmon resonance is an optical excitation of surface plasmons or a charge density wave on the interface between the conductor (e.g., gold or silver) and a dielectric (insulator may be a gas, liquid or solid). The resonance wave vector related to the optical excitation of surface plasmon waves is dependent on the refractive index of the metal and the dielectric contacting them. SPR occurs in a thin metal film with a negative dielectric constant (high conductivity), which is arranged on a transparent dielectric substrate. The phenomenon of SPR is that at the corners corresponding to total internal reflection within the thin metal film by laser radiation conduction electrons in the metal film are excited, that is observed as a sharp decrease in the intensity of reflected light at a specific (resonance) angle of incidence. For analytical instrumentation is important that the magnitude of the resonance angle depends on the concentration of the substance on the surface of the sensor element. Most sensitive as the metal layer is used as the gold metal layer with a high conductivity and a high chemical inertness. Based on the SPR phenomenon refractometric method has been successfully used for the analysis of the optical properties of a wide range of substances, from gases (e.g., anesthetic gases) [1] to liquids (e.g., analysis of the binary system of methanol in water), [2] and the solids (e.g. inorganic solid particles [3] and the organic film Langmuir-Blodgett [4]). Diagnosing the devices working on the phenomenon of SPR is highly sensitive to low concentrations of analytes, allowing them to be used not only as a gas analyzer [5], but also as high-precision analytical instruments for laboratory analysis in the food, chemical and pharmaceutical industry, in agriculture, medicine, environment [6-11]. At the same time, up to date the influence of state and topology of sensor element surface on accuracy and stability in operation of SPR sensor appliance is investigated insufficiently. As known, increasing the area of the excitation surface plasmon layer SPR sensor affects to growing response and the adhesion surface to immobilize ligands (receptors) or adsorbers.

## *2. Preconditions and means for resolving the problem*

Sensitivity of detection change of refractive index is determined by the lowest minimum SPR angular shift, which can be registered. This shift corresponds to the minimum value of the minimum detectable change in refractive index. Some manufacturers of devices, that use the phenomenon of SPR, are using values shift SPR curve minimum relative angular values RU (RU = $8.3 \times 10^{-5}$ angular degrees, which is equivalent to one picogram substance on the surface of the sensor SPR) to estimate the sensitivity, while others are measuring the absolute sensitivity values of the refractive index RIU (refractive index unit) [12]. And the change of the angle is proportional to the concentration of the substance analyzed volume. Therefore, in liquids such sensor responds only to changes of refractive index and absorption of the medium. In a gas medium components of admixture adsorption on the surface of the sensor is observed, which leads to higher concentration in the zone of sensitivity in compared to the volume. So, sensor responds as to changes of refractive index and absorption, as to thickness of the adsorbed layer on a surface of the sensor element. The quantity of adsorption depends on the material and surface properties (roughness, porosity, etc.). The increasing of sensing element`s surface porosity allows to increase the response of the sensor as in the gas medium analysis [13, 14], as in the aqueous solutions analysis [15].

Sensitivity of the method also determined by SPR`s width and shape of the absorption curve, which determines the accuracy of detecting the position of its minimum. Therefore, a possible way to significant increase (by orders of magnitude) the sensitivity of SPR sensors is to apply the methods of narrowing the resonance spectrum. This can be achieved by placing on a sensitive area holographic and diffraction structures that produced on the sensor surface [16]. Narrowing of the resonance spectrum is also possible through the using of bimetallic silver-gold layers on the sensor surface [17] and increasing the laser wavelength excitation SPR [18].

Evolution of increasing sensitivity of SPR instruments looks like follows. In 1998, the company a BIACORE reported of achieving sensitivity of $2 \times 10^{-5}$ RIU, three years later, the sensitivity increased to $1 \times 10^{-5}$ RIU. At the same time, other authors [19] reported of sensitivity $1.2 \times 10^{-6}$ RIU. In 2014, the BIACORE reported of achieving sensitivity of 10 RU, and the company Reichert reported of achieving sensitivity of $1 \times 10^{-7}$ RIU [20].

Further increase in sensitivity is limited by frequency stability and spectral width of semiconductor lasers [21], noise and thermal drift of photo detectors equipment. Reducing the influence of temperature on the sensitivity of devices based on SPR thermostatization achieved not only the sensor but also the whole

device together with receptacles for the test substances [22]. In addition, as a result of experimental studies suggested that optimization of thermal temperature regimes of the device [23].

Increasing the sensitivity of SPR measurement devices is possible by modifying the surface of the sensor and optimization of manufacturing technology. Depending on the particular problem to be solved, the simplest way is to use highly selective sorbents, or mixtures deposited on the sensing surface.

It follows from the mentioned above that it is necessary to determine and investigate experimentally the influence of plasmon exciting layer topology that provides increasing response of sensor transducer in optical measurements based on SPR when performing measurements in various media.

## *3. Solution of the investigated problem*

To solve the problem was used optical measurement equipment developed in Ukraine [24]. The equipment measures the change in the refractive index of the test substances on which to judge the processes of deterioration, adsorption processes, etc. In V. Lashkaryov Institute of Semiconductor Physics, NAS of Ukraine, performed for many years are experimental investigations of applied aspects for designing biosensors based on SPR. One of the designed models is the spectrometer "Plasmon-71" (Fig. 1) suitable for operation in labs of biochemical and biophysical profiles. This device allows you to measure the refractive index over a wide range from 1 to 1.5 RIU, refractive index shift measuring range 5 RU (relative units) to 130 000RU with an accuracy $\pm 3\times10^{-6}$ RIU (refractive index unit).




***Fig. 1.*** *Appearance of the SPR spectrometer Plasmon-71*

Devices based on the SPR allow quickly determining the optical properties and monitoring processes in real time.

Within the frameworks of these investigations, developed and manufactured was the thermostat that enables to keep the set temperature with rather high stability. The thermostating, offered after performed investigations, were not only of the studied object but also of all the measuring equipment including boxes with the studied substances. This approach enabled to minimize the temperature error in measurement results and, in addition, temperature loading the measuring equipment, which prolongs its functioning term [25].

The investigations were carried out to optimize the geometry of the deposition layers on the surface of bimetallic sensing elements. As a material used gold layers. Alternating layers sprayed onto a glass substrate F1 in a vacuum depositing device VUP-5M (Fig. 2) with vacuum of $5 \times 10^{-5}$ mmHg. Depositing a first layer of a thickness of 35 nm, produced at the location of the substrate parallel to the surface of the evaporator (typically sputtering), a second layer was sprayed on the first layer at the location of the substrate at an angle to the evaporator. The thickness of the second layer, considering deposition at an angle, was of approximately 30 nm. The thickness of the deposited layer was monitored by a quartz thickness indicator by change of its oscillation frequency.




***Fig.2.*** *Appearance of the vacuum depositing device VUP-5M*

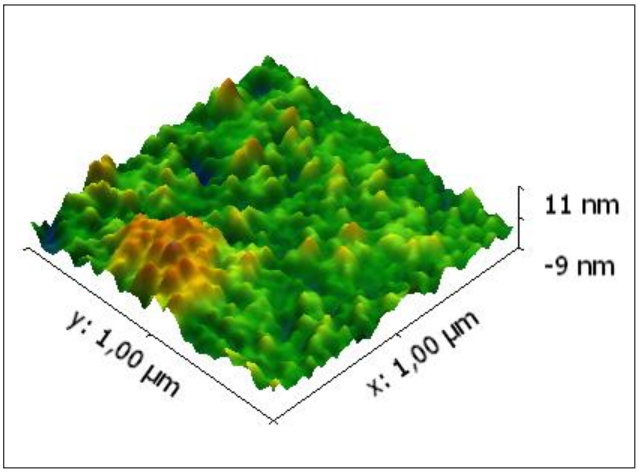
The two test sample of sensing elements was used in a experiment: a typical plated gold layer thickness of 50 nm on the substrate (structure number 1) and the modified geometry deposition (structure number 2). Experiments were carried out in the Multiple mode. In this mode, the minimum of SPR curve was determined and recorded at each scan. To determine the sensitivity of the sensory of structures known aqueous solutions used in the tow-channel flow cell that provide contact of fluid with the structure number 1 or number 2. Flow cell was equipped by injection and removal of tested liquid or gas tubes. The study was conducted on a samples of two liquids with different refractive indices: distilled water (n = 1,33154) and 0.6% potassium chloride solution (KCl) in water (n = 1,33241). A substitution of fluid sample was performed by a peristaltic micro-pump, which also produced in V. Lashkaryov Institute of Semiconductor Physics NAS of Ukraine (Fig. 3). The room air and ethanol vapor in flow cell was used as gas-sensing. The changes of the refractive index in time were recorded on the moment when distilled water was in the cell, and after the substitution with solution. Likewise, sample gas substitution was carried out. Kinetics shift SPR minimum recorded by developed program.



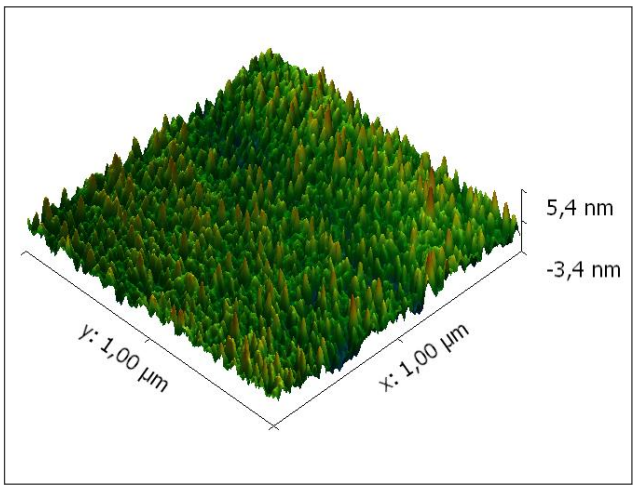

***Fig.3.*** *Appearance of the peristaltic micro-pump*

## 4. *Results and discussion*

Surface topology of the samples number 1 and number 2 was studied by atomic force microscope (AFM) using [26]. It has been found that the structure of the gold layer number 2 obtained by spraying angle has a developed surface and hence it in compare to a large surface area compared to the structure number 1 (Fig.4). SPR curves for this samples performance on Fig.5.




A)




B)

***Fig.4.*** *AFM images of researching sample: structure number 1(A) and structure number 2 (B)*

After two fluid replacement procedures on 24 minutes of measurement by using structure number 1 refractive index of liquids significantly changed the in compare to its initial value (Fig. 5, curve №2). To the structure number 2 the refractive index of distilled water and salt solution remained almost unchanged during the measurement (Fig. 5, curve №1). Furthermore, the response to the replacement fluid in the flow cell structure number 2 was 1.5-fold greater than the response to the structure of number 1, and the refractive index of the salt solution potassium chloride (KCl) is closer to the theoretical value (n = 1,33248), than in the case of using the structure number 1 (n = 1,33219). Kinetics of substitution in the measuring cuvette SPR spectrometer PLASMON room air ethanol vapor concentrations varying shown in Fig. 7. Shows the kinetics of the samples for the two sensitive elements of the SPR sensor: standard topology (line 1) and modified (line 2). From Fig. 7 shows that the technology of production of modified topology can increase response sensor 2 times.

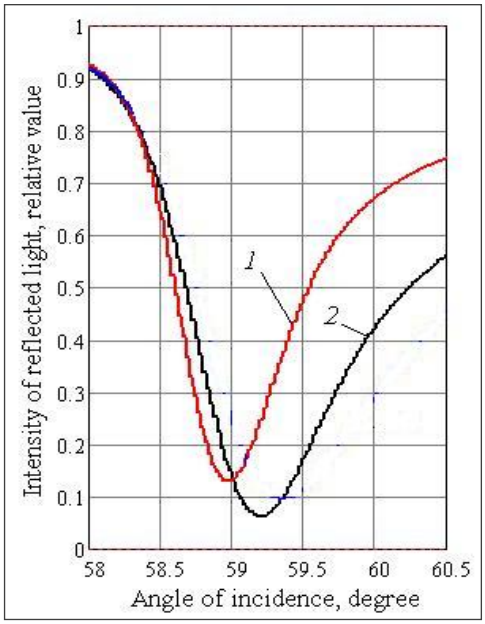



***Fig. 5.*** *SPR curves of measured samples: structure number 1(red line) and structure number 2 (black line)*

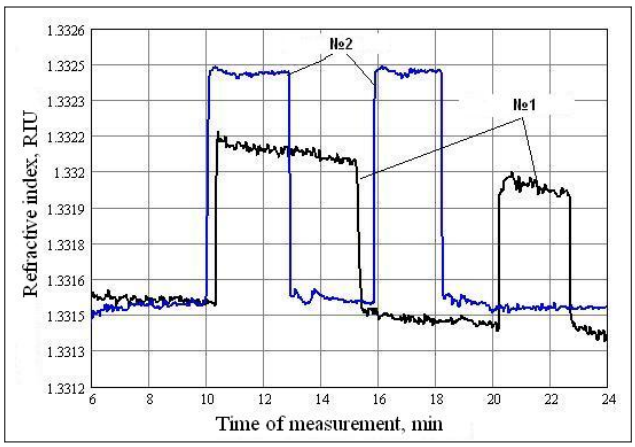



***Fig. 6.*** *Measured curve kinetic process in liquid media*

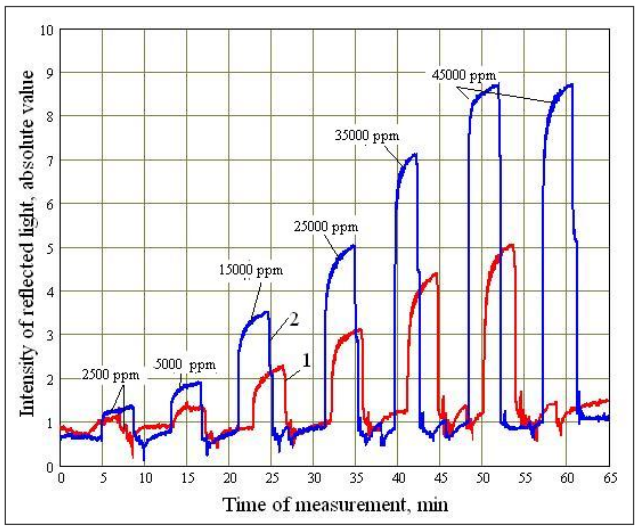



***Fig. 7.*** *Measured curve kinetic process in gas-like media*

## 5. Conclusion

The geometry of gold sputtering films with optimum thickness, which provides a 1.5-fold greater response to changes of the refractive index of the liquid medium above the SPR sensor, and a 2-fold greater response with a change in the refractive index of a gaseous medium, in comparison with the standard gold chips was proposed. This will improve precision of measurement and increase the use of surface plasmon resonance in the industry and ecology for diagnosis and monitoring structures and elements of goods, manufacturing processes and for monitoring production safety.

## References


[1] Liedberg B., Nylander C., Lundstrom I. Surface Plasmon Resonance For Gas Detection and Biosensing // Sensors and Actuators. — 1983. — N 4. — P. 299–304.

[2] Matsubara K., Kawata S., Minami S. Optical Chemical Sensor Based on Surface Plasmon Measurement // Applied Optics. — 1988. — **27**. — P. 1160–1163.

[3] H. Xu and M. Kall Modeling the optical response of nanoparticle-based surface plasmon resonance sensors // Sensors and Actuators. — B Vol. 87, N 2. — P. 244-249.

[4] Rella R., Siciliano P., Quaranta F., Primo.T., Valli.L., Schenetti L., Mucci A., Iarossi D. Gas Sensing Measurements and Analysis of the Optical Properties of Poly [3-(butylthio)thiophene] Langmuir-Blodgett films Sensors and Actuators B68 (2000) 203-209

[5] A.V. Samoylov, V.M.Mirsky, Q. Hao, C. Swart, Y.M. Shirshov, O.S.Wolfbeis. Nanometer-thick SPR sensor for gaseous HCl // Sensors and Actuators B Chem. – 2005. – Vol.106. – P.369-372.

[6] Gridina N., Dorozinsky G., Khristosenko R., Maslov V., Samoylov A., Ushenin Yu., Shirshov Yu. Surface plasmon resonance biosensor // Sensors & Transducers Journal. – 2013. – Vol.149, № 2. – P.60-68.

[7] A. V. Samoylov, Yu. V. Ushenin, R. V. Khristosenko. Application of surface plazmon resonance spectrometer for determination of optical parameters of the thin polyaniline films.. “International Conference «Functional Materials» ICFM ’ 2007”.

[8] N.Ya.Gridina, A.V.Samoilov, Yu.V.Ushenin, Yu.M.Shirshov, Diagnostic possibility demonstration’ of cerebrum oncologic diseases by biosensor based on surface plazmon resonance, International Conference “Functional MAterial” ICFM-2009, 5-10 October, 2009, Partenit, Ukraine.

[9] Shirshov Yu.M., Samoylov A.V., Zinyo S.A., Surovceva E.R., Mirskiy V. Bimetallic Layers Increase Sensitivity of Affinity Sensors Based on Surface Plasmon Resonance // Sensors – 2002.– Vol.2, – 62-70.

[10] K.V. Kostyukevych, R.V. Khristosenko, Yu.M. Shirshov, S.A. Kostyukevych, A.V. Samoylov, V.I. Kalchenko Multi-element gas sensor based on surface plasmon resonance: recognition of alcohols by using calixarene films // Semiconductor Physics, Quantum Electronics and Optoelectronics.- 2011. – V.14, N3. P. 313-320.

[11] A. Rachkov, Yu. Holodova, Yu. Ushenin, D. Miroshnichenko, G. Telegeev, A. Soldatkin, „Development of Bioselective Element of SPR Spectrometer for Monitoring of Oligonucleotide Interactions and Comparison with Thermodynamic Calculations”, *Sensor Letters*, 2009, Vol. 7.

[12] Кобзева И.Н. Оптические сенсоры для биосенсорных диагностических систем на основе поверхностно-плазмонного резонанса // Вісник КДПУ імені Михайла Остроградського. Випуск 4/2009 (57). Частина 2..

[13] Ушенин Ю.В., Христосенко Р.В., Самойлов А.В., Дорожинский Г.В., Каганович Э.Б., Манойлов Э.Г., Снопок Б.А. Оптоэлектронные сенсорные структуры на основе пленок пористого оксида алюминия, полученных импульсным лазерным осаждением // Оптоэлектроника и полупроводниковая техника. – 2012 – № 47. – С.40-45.

[14] Ushenin Yu.V., Khristosenko R.V., Samoylov A.V., Kaganovich E.B., Manoilov E.G., Snopok B.A., Dorozinsky G. W., Maslov V.P. Porous alumina films obtained by pulsed laser deposition for sensors applications // International Conference “Functional Material” (ICFM-2013). – Partenit: Ukraine. – 2013. – P.451.

[15] Вакарюк Т.Є., Громовой Ю.С., Данько В.А., Дорожинський Г.В., Зиньо С. А., Індутний І.З., Самойлов А.В., Ушенін Ю.В., Христосенко Р.В., Шепелявий П. Є. Використання поруватих плівок SiOx в сенсорах на основі поверхневого плазмонного резонансу // Оптоэлектроника и полупроводниковая техника. – 2013 – № 48. – С.89-95.

[16] Palagushkin A.N., Prokopenko S.A., and Sergeev A.P. Plasmonic Holographic Nanostructures // Optical Memory and Neural Networks (Information Optics). 2009. Vol. 18. No. 3, pp. 156–163. Allerton Press, Inc.

[17] Shirshov Yu.M., Samoylov A.V., Zinyo S.A., Surovceva E.R., Mirskiy V. Bimetallic Layers Increase Sensitivity of Affinity Sensors Based on Surface Plasmon Resonance // Sensors – 2002.– Vol.2, – 62-70.

[18] Ю.В. Ушенін, А.В. Самойлов, Р.В. Христосенко. Увеличение чувствительности сенсоров изменения показателя преломления среды на основе поверхностного плазмонного резонанса // Технология и конструирование в электронной аппаратуре -2011.- №1-2(90) - С. 12-14.

[19] Dostalek J., Ctyroky J., Homola J., Nekvindova P., Spikova J., Skvor J., Schrofel J. Surface plasmon resonance biosensor based on integrated optical waveguide // Sensors and Actuators, B. –2001. – Vol.76. – P.8-12.

[20] www.reichertspr.com

[21] Байбородин Ю.В. Основы лазерной техники. – 2-е изд. перераб. И доп. – К.: Выща шк. Головное изд-во, 1988. – 383 с.

[22] Dorozinsky G., Maslov V., Samoylov A., Ushenin Yu. Reducing measurement uncertainty of instruments based on the phenomenon of surface plasmon resonance // American Journal of Optics and Photonics. – 2013. - Vol.1, № 3. – P.17-22.

[23] Dorozinsky G., Dunaevsky V., Maslov V. Thermal-vision method of investigations and control of device based on surface plasmon resonance // Universal Journal of Control and Automation. – 2013. - Vol.2. – P.34-39.

[24] www.plasmon.org.ua

[25] Gleb Dorozinsky. Surface plasmon resonance as a tool for research in nanotechnology and industry // 10th International Congress “Machines.Technologies.Materials’13” (MTM-2013). – Varna: Bulgaria. – 2013. – P.59-62.

[26] www.microscopy.org.ua

# PLASMA SURFACE TECHNOLOGY PROMOTING CAPILLARY IMPREGNATION OF WOOD: XPS ANALYSIS OF DIFFERENT PLASMA PRE-TREATED WOOD SURFACES

Assist. Prof. Ivanov I. [1], Assoc. Prof. Gospodinova D. Ph.D. [1], Prof. Dineff P. Ph.D. [1], Prof. Veleva L. Ph.D. [2]
Faculty of Electrical Engineering - Technical University of Sofia, Bulgaria [1]
CINVESTAV - Merida, Yucatan, Mexico [2]
E-mail: dilianang@abv.bg

***Abstract:*** *X-ray Photoelectron Spectroscopy (XPS) also referred to as Electron Spectroscopy for chemical analysis (ESCA) was used to characterize the surfaces of plasma-chemical treated wood in air by dielectric barrier discharge (DBD). The plasma-surface pre-treatment of wood, wooden products and cellulosic fibrous materials has been developed for promoting capillary impregnation and plasma-aided flame retardency. In this study, XPS has been used since it has proved to be suitable investigation method to characterize the composition of a plasma pre-treated material surface. This method is a powerful analytical and non-destructive technique which has already been used for the analysis of plasma modified wood surfaces and in the characterization of wood's reactions. Changes due to the plasma-chemical process were identified from the survey large spectra as well as from the detailed $C_{1s}$ and $O_{1s}$ spectra. The oxidative changes were quantified with the atomic ratio of oxygen to carbon and with a detailed analysis of the contributions to the $C_{1s}$ and $O_{1s}$ peaks.*

**Keywords**: ATMOSPHERIC DIELECTRIC BARRIER DISCHARGE (*DBD*), FLAME RETARDANT, CAPILLARY IMPREGNATION, TROPICAL (RAIN-FOREST) WOOD, X-RAY PHOTOELECTRON SPECTROSCOPY (*XPS*).

## *1. Introduction*

*The plasma aided flame retardation* of wood and wood products has been developed as a result of a new plasma-aided process of *capillary impregnation* that comprises a surface plasma pre-treatment for alteration of the chemical, electrical (ionic), and capillary activities of wood surface, in general for improvement the technological characteristics of the capillary impregnation process. This study has been developed as part of a large research on plasma-chemically activated wood surface and flame retardant treated rain-forest wood.

A technological system of air plasma device and applicators has been created to produce cold technological plasma through dielectric barrier discharge (*DBD*) at atmospheric pressure and room temperature. The cold plasma pre-treatment by non-equilibrium *DBD* of wood, like rain-forest woods - *Tzalam*, *Caoba Mahogany*, and *Mexican White Cedar* (Mexico, Yucatán), improves technological characteristics such as solution spreading and wicking speed, as well as specific amount of the sorbed flame retardant. Due to its fine-texture and surface inactivation it is difficult to apply flame retardants directly through capillary impregnation. In this way, the plasma pre-treatment of wood and wooden products improves its flame retardation. The plasma-chemical surface pre-treatment by dielectric barrier air discharge at atmospheric pressure (*DBD*) was specified as a new good way for wood surface functionalization and activation [1, 2, 3, and 4].

Wood is a complex material constituted mainly of three biopolymers: lignin, cellulose and hemicelluloses. In addition to these polymeric components, wood may contain extractives in more or less large quantities including several classes of organic compounds like sugars, flavonoids, tannins, terpenes, fats or waxes. Well-suited for the study of surface chemistry of complex organic materials, *X-ray photoelectron spectroscopy* (*XPS*) also referred to as *Electron Spectroscopy for chemical analysis* (*ESCA*) has been widely used in order to investigate the surface chemical composition of numerous lignocellulosic materials especially in the field of pulp and paper, where the surface chemistry is of considerable importance for the properties of the final products. Similarly, some reported studies investigate the changes of surface chemistry after different wood transformation processes and processing [4 and 5].

*X-ray photoelectron spectroscopy* is a surface chemical analysis technique that can be used successfully to analyze the surface chemistry of a material in its "*as received*" state, or after some treatment such as plasma-chemical surface pre-treatment. The binding energy is a characteristic of the atoms, which can be used for elemental identification on the plasma chemically modified wood surface.

The interpretation of the curve fit of the carbon C 1s peak after *Kazayawoko* (1998) was used to interpret the changes of wood surface chemistry after plasma *DBD* pre-treatment. To obtain a deeper insight into the various functional groups, the C 1s signal is usually deconvoluted into four components according to the number of oxygen atoms bonded to *C*, [5]:

□ The $C_1$ class corresponds to carbon atoms bonded only with carbon or hydrogen atoms (C-C or C-H), and it is usually pointed out at a *binding energy* (*BE*) of 284.6 eV (some also use 285.0 eV as the nominal value for the binding energy of carbon);

□ The $C_2$ class reveals the carbon atoms bonded with one oxygen atom (C-O or C-OH), and it appears at a higher binding energy compared to $C_1$ ($\Delta_{BE}$ = + 1.5 ± 0.2 eV) - 286.1 ± 0.2;

□ The $C_3$ class corresponds to carbon atoms bonded to a carbonyl (C=O) or two non-carbonyl oxygen atoms (O-C-O), and it appears at a higher binding energy compared to $C_1$ ($\Delta_{BE}$ = + 2.8 ± 0.2 eV) - 287.4 ± 0.2 .

□ And finally, the $C_4$ class is associated with carbon atoms bonded to a carbonyl and a non-carbonyl oxygen atom (O-C=O) - it appears at a higher binding energy compared to $C_1$ ($\Delta_{BE}$ = + 3.75 ± 0.2 eV) - 288.35 ± 0.2.

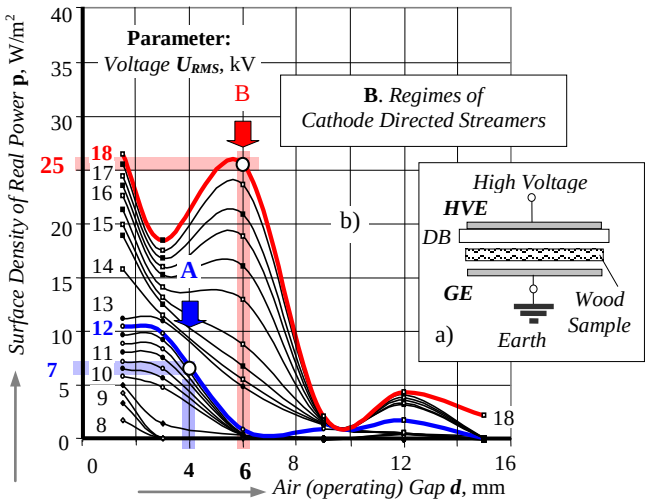



**Fig. 1.** Plasma-chemical surface pre-treatment of wood sample by non-equilibrium dielectric barrier air discharge at atmospheric pressure in asymmetric coplanar system with one glass barrier (**a**), technological regimes (*A* and *B*) of cathode directed streamers (**b**).

**Table 1:** Elemental surface composition of three heartwood species before (*K*) and 2 hours after plasma pre-treatment (*DBD*: 12/18 kV) determined from wide *XPS*-spectra.

| *Wood* | *Samples* | *Peaks on the Wide XPS-spectra - Chemical Surface Composition*, at. % | | | | | | |
|---|---|---|---|---|---|---|---|---|
| | *Peaks* | **C** | **O** | **N** | **P** | **Si** | **nO/nC** |
| **Tzalam** Heartwood | *K* (Non-Treated) | **83.71** | **14.49** | 1.53 | - | 0.27 | **0.17** |
| | *DBD* Pre-treated | 12 kV (50 Hz) | 66.55 | 32.43 | 1.03 | - | - | 0.49 |
| | | 18 kV (50 Hz) | 61.38 | 37.63 | 0.99 | - | - | 0.61 |
| **Caoba Mahogany** Heartwood | *K* (Non-Treated) | **81.12** | **18.39** | 0.49 | - | - | **0.23** |
| | *DBD* Pre-treated | 12 kV (50 Hz) | 78.25 | 20.17 | 1.58 | - | - | 0.26 |
| | | 18 kV (50 Hz) | 71.06 | 28.21 | 0.73 | - | - | 0.40 |
| **Mexican White Cedar** Heartwood | *K* (Non-Treated) | **79.86** | **17.75** | 1.41 | - | 0.98 | **0.22** |
| | *DBD* Pre-treated | 12 kV (50 Hz) | 61.34 | 35.17 | 1.44 | 2.05 | - | 0.57 |
| | | 18 kV (50 Hz) | 66.83 | 29.92 | 2.24 | 1.01 | - | 0.45 |

This is a necessary condition to get better knowledge of the chemical transformations occurring during plasma-chemical surface pre-treatment and to propose an interpretation in terms of existing and known mechanisms.

*The objective* of this paper was to study the effect of plasma chemical surface pre-treatment of *DBD* in air (oxidative atmosphere) at atmospheric pressure and room temperature at industrial frequency (50 Hz) and two voltages - 12 and 18 kV (RMS), on the wood surface functionalization monitored by surface chemical composition change. Therefore, we focused mainly on the O/C ratio evolution and on the changes in the various components of the C (1s) and O (1s) lines.

## *2. Experimental Investigation*

On basis of prior art, as well as on our own experience in plasma-aided impregnation of wood and wooden materials, [1, 2], an oxidative surface plasma pre-treatment has been applied on the test samples for 60 sec in a non-equilibrium cold plasma of *DBD* at atmospheric pressure. Similar changes are the basis of the expected *DBD*-surface functionalization effect on the three species of rain-forest wood samples, plasma pre-treatment in two types of *DBD* in air was performed: *i*) *A - DBD* at industrial frequency (50 Hz) and relatively low voltage (12 kV RMS; 16.9 kV PV) at which the discharge regime is transitionally from electron avalanche to cathode directed streamers; *ii*) *B - DBD* at industrial frequency and relatively high voltage (18 kV RMS; 25.4 kV *PV*) characterizing the regime of cathode directed streamers, Fig. 1.

*X-ray photoelectron spectroscopy analysis* was carried out by using a photoelectron spectrometer *VGS ESCALAB Mk II* with monochromatic *AlKα* radiation source (*FWHM* = 0.5 eV). *XPS-spectra* were obtained by irradiating a wood sample with a beam of *X-rays*. The angle between the directions of the incident *X-ray* and that of the observations (fixed by analyzer entrance slit) was 50.

Studies of *cold plasma functionalization phenomena on wood*, i.e. interactions of oxidative cold plasma with wood surface, may add valuable information about the capillary impregnation, gluing and coating properties of wood. Such information is essential in the development of efficient processing methods, and for the prediction of the functionality and durability of wood products.

Three species of Mexican rain-forest heartwood were investigated: *i - Tzalam* (*Lysiloma bahamensis*); *ii - Caoba Mahogany* (*Swietenia macrophylla*); and *White Cedar* (*Cupressus Lusitanica*).

## *3. Results and Discussion*

The results from the wide *XPS* survey spectra of investigated wood samples before (*DBD* non-treated) and two hours after plasma chemical treatment (*DBD* pre-treated) are presented in Table 1. Analysis of the survey spectra indicates the presence of carbon (*C*), oxygen (*O*) and small amounts of nitrogen (*N*), phosphor (*P*) and silicon (*Si*) which represent the expected elements in wood.

High-resolution scans of the *XPS* spectra of C (1s) and O (1s) levels are also presented with their decomposition into components, respectively Fig. 2 and 3.

Using the total areas of these peaks and the respective photoemission cross-sections, a quantitative determination of the O/C ratio can be calculated. By knowing the chemical composition of each of these components, it is possible to calculate *a priori* the theoretical O/C ratio characteristic of non-treated wood samples [5].

**Table 2.** *Carbon peak C (1s) components or proportions of oxygen (O) and carbon (C) functional groups of heartwood surfaces before (K) and 2 hours after plasma surface pre-treatment (DBD:*12/18 kV*) determined from high-resolution XPS-spectra.*

| *Woods* | *Samples* | *Carbon peak $C_{s1}$ components*, area % | | | | | | | | |
|---|---|---|---|---|---|---|---|---|---|---|
| | | **C1** (C-C or C-H) | **C2** (C-O or C-OH) | **C2-3** (ND) | **C3** (C=O or O-C-O) | **C4** (O-C=O) | **C4-** (ND) | nC1/ nC2 | **Sum** (nC2+ nC3 | nC2/ (nC2+nC3) |
| | | (**285.0** ±0.4 eV) | (**286.0** ±0.4 eV) | (287.0 ±0.4 eV) | (**288.7** ±0.4 eV) | (**289.5** ±0.4 eV) | (292.8 ±0.4 eV | - | - | - |
| Tzalam Heartwood | *K* (Untreated) | 56.79 | **15.20** | 0.00 | **4.14** | 0.00 | 0.00 | **5.31** | **19.34** | **0.79** |
| | *DBD* Pre-treated 12 kV | 35.04 | 27.12 | 22.01 | 15.27 | 0.00 | 0.56 | 1.29 | 42.39 | 0.64 |
| | *DBD* Pre-treated 18 kV | 42.33 | 30.92 | 15.35 | 9.23 | 0.00 | 2.17 | 1.40 | 40.15 | 0.77 |
| Caoba Mahogany Heartwood | *K* (Untreated) | 57.22 | **12.67** | 0.00 | **6.23** | 0.00 | 0.00 | **6.40** | **18.90** | **0.67** |
| | *DBD* Pre-treated 12 kV | 49.65 | 26.14 | 0.00 | 14.71 | 9.50 | 0.00 | 1.90 | 40.85 | 0.64 |
| | *DBD* Pre-treated 18 kV | 51.69 | 22.92 | 0.00 | 12.29 | 13.10 | 0.00 | 2.26 | 35.12 | 0.65 |
| Mexican White Cedar Heartwood | *K* (Untreated) | 54.22 | **17.40** | 0.00 | **4.60** | 0.00 | 0.00 | **4.48** | **22.00** | **0.79** |
| | *DBD* Pre-treated 12 kV | 45.94 | 27.96 | 15.05 | 5.98 | 0.00 | 5.07 | 1.64 | 33.94 | 0.82 |
| | *DBD* Pre-treated 18 kV | 50.23 | 20.74 | 15.22 | 13.10 | 0.00 | 0,71 | 2.42 | 33.84 | 0.61 |

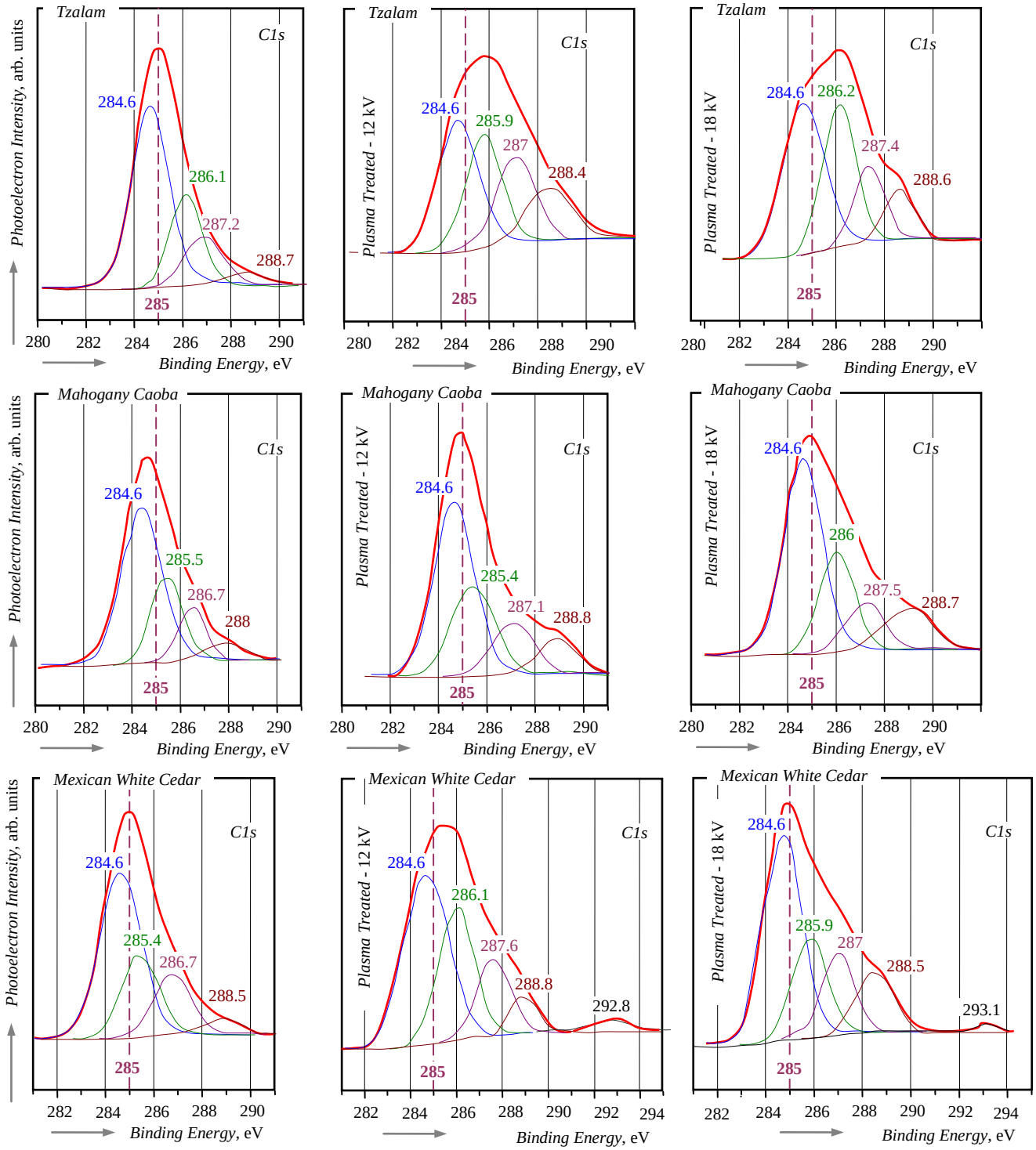



**Fig. 2.** Carbon *C (1s)* peak in photoelectron *XPS/ESCA* spectra of bare samples of heartwood and 2 hours after plasma surface pre-treatment in atmospheric dielectric barrier discharge in air at industrial frequency (50 Hz) and 12 and 18 kV (RMS) voltage.

*Cellulose* comprises five carbon atoms of $C_2$ and one of $C_3$ with an O/C of **0.83**. *Hemicelluloses*, which are mainly represented by glucuronoxylans, are constituted of fewer than five carbon atoms of $C_2$, less than one carbon atom of $C_4$ for the acetyl and carboxylic groups and one atom of $C_3$ with an O/C of approximately **0.8**0. The contribution of *lignin* is more complex and therefore more difficult to quantify. Four types of carbons are present in its structure with a greater contribution from the $C_1$ and $C_2$ classes and an O/C ratio of roughly **0.33.** *Extractives* are also present in very small quantities in wood and their contribution to the overall *XPS* spectrum is relatively low - for example carbon atoms of $C_4$ class are present in *linolic* and *abietic* acid with an O/C of 0.11/0.10, respectively [**5]**.

From the data of untreated wood samples, it appears that carbon atoms bonded with one oxygen atom ($C_2$ class) are the most abundant. Carbon atoms bonded with other carbon or hydrogen ($C_1$ class) or bonded with two oxygen atoms ($C_3$ class) are present in smaller proportions, while those bonded with three oxygen atoms are less abundant Table 2.

The O/C ratio may be estimated from the individual ratio and abundance of each component, or from the elemental composition determined experimentally in the case of untreated wood samples. According to these methods, the O/C ratios are found to be of and 0.17, 0.22 and 0.23, respectively,Table 1.

The O/C ratio and distribution of carbon atoms of plasma treated samples differ considerably from those obtained for untreated wood: 0.49, 0.26 and 0.57 (*DBD*:12 kV); 0.61, 0.40 and 0.45 (*DBD*: 18 kV). The increased O/C ratio is attributed to the important oxidation occurring during cold plasma-treatment: the $C_1$ (C-C; C-H) contribution decreased considerably while

**Table 3.** *Oxygen peak O (1s) components or proportions of oxygen (O), carbon (C) and hydrogen (H) functional groups of heartwood surfaces before (Tzalam-K) and after plasma surface pre-treatment (DBD*: 12/18 kV*) determined from high-resolution XPS-spectra.*

| *Woods* | *Samples* | **O1** (O=C) | **O2** (O-H) | **O3** (O-C; H-O-H) | Sum1 ($O_1$;$O_3$) | Sum2 ($C_2$;$C_3$) | Sum1 ($O_1$;$O_3$) - Sum2 ($C_2$;$C_3$) (H-O-H) | **O3'** (O-C) |
|---|---|---|---|---|---|---|---|---|
| | *Binding energy*, eV | **531.5**±0,4 | **532.5**±0,4 | **533.0**±0,4 | | | | |
| Tzalam (*Lysiloma bahamensis*) | *K*: untreated | 0.00 | **58.48** | **41.51** | 41.51 | 19.34 | **22.17** | **19.34** |
| | *DBD*: 12 kV (50 Hz) | 0.00 | 56.21 | 43.79 | 43.79 | 42.39 | 1.40 | 42.39 |
| | *DBD*: 18 kV (50 Hz) | 0.00 | 58.74 | 41.26 | 41.26 | 40.15 | 1.11 | 40.15 |
| Caoba Mahogany (*Swietenia macrophylla*) | *K*: untreated | 0.00 | **58.00** | **42.00** | 42.00 | 18.90 | **23.10** | **18.90** |
| | *DBD*: 12 kV (50 Hz) | 0.00 | 58.62 | 41.38 | 41.38 | 40.85 | 0.53 | 40.85 |
| | *DBD*: 18 kV (50 Hz) | 0.00 | 56.72 | 43.28 | 43.28 | 35.12 | 8.16 | 35.12 |
| Mexican White Cedar (*Cupressus Lusitanica*) | *K*: untreated | 0.00 | **53.22** | **46.78** | 46.78 | 22.00 | **24.78** | **22.00** |
| | *DBD*: 12 kV (50 Hz) | 0.00 | 61.43 | 38.57 | 38.57 | 33.94 | 4.63 | 33.94 |
| | *DBD*: 18 kV (50 Hz) | 0.00 | 56.70 | 43.30 | 43.30 | 33.84 | 9.46 | 33.84 |

the $C_2$ (C-O; C-OH), $C_3$ (C=O; O-C-O) contribution increased, and $C_4$ (O=C-O) appears in *Caoba Mahogany*, indicating that the content of C-O, C-OH, C=O, O-C-O and O=C-O groups becomes more important. This plasma modification can not be attributed to an increase of the lignin content due to preferential degradation of hemicellulose.

Figures 2 and 3 show typical *XPS* survey spectra and high resolution C (1s) and O 1s spectra of plasma-treated Tzalam, Caoba mahogany and White cedar wood. When comparing C 1s spectra presented in Fig. 2, it is clear that the contribution of the different types of carbons differs strongly between untreated and plasma-treated wood samples. $C_3$ and $C_2$ contributions increased highly, while the $C_1$ contribution (attributed to lignin) decreased seriously after plasma-treatment.

The contribution of the different types of oxygen atoms is much more difficult to analyze, Fig. 3. $O_1$ and $O_3$ classes report the contribution of two types of carbon atoms - O=C and O-C while $C_2$ and $C_3$ classes report the contribution similarly of different types of oxygen atoms - C-O, C-OH, C=O and O-C-O. The difference between *Sum1* ($O_1$ + $O_3$) and *Sum2* ($C_2$ + $C_3$) can be attributed to the amount of water on the wood surface (H-O-H), Table 3.

The plasma chemical surface modification removes successfully the water (H-O-H) from the wood surfaces. The difference (*Sum1-Sum2*) was decreased highly two hours after plasma pre-treatment: *Tzalam* - form 22.17 to 1.40/1.11; *Caoba Mahogany* - from 23.10 to 0.53/8.16; and *Mexican white cedar* - from 24.78 to 4.63/9.46, respectively, Table 3.

The $O_3$ class reveals the oxygen atoms bonded with one carbon atom and two hydrogen atoms (O-C and H-O-H). A new difference between $O_3$ class and the difference (*Sum1-Sum2*) reveals the abundance of oxygen atoms bonded with other carbon atom (O-C). From the data of untreated and plasma treated wood samples, it appears that carbon atoms bonded with one oxygen atom ($C_2$ or $O_3$' class) increase essentially its quantity after plasma treatment: *Tzalam* - form 19.34 to 42.39/40.15; *Caoba Mahogany* - from 18.90 to 40.85/35.12; and *Mexican white cedar* - from 22.00 to 33.94/33.84, respectively, Table 3.

When using high energy resolution experiment settings on *XPS* equipped with a monochromatic Al K-alpha X-ray source, the *Full Width at Half Maximum* (*FWHM*) of the main investigated *XPS*-peaks range from:

□ The $C_1$, $C_2$, $C_3$ and $C_4$, or C (1s) component, peaks of untreated (bare) woods have *FWHM*s that, in general, range from 1.3 eV to 2.0 eV: *Tzalam* - from 1.6 to 2.0; *Caoba Mahogany* - from 1.3 to 2.0; and *Mexican white cedar* - from 1.8 to 2.0;

□ The $C_1$, $C_2$, $C_3$ and $C_4$ peaks of plasma treated (*DBD*: 12 kV) woods have *FWHM*s that, in general, range from 1.4 eV to 2.34 eV: *Tzalam* - from 1.8 to 2.2; *Caoba Mahogany* - from 1.98 to 2.16; and *Mexican white cedar* - from 1.4 to 2.34.

□ The $C_1$, $C_2$, $C_3$ and $C_4$ peaks of plasma treated (*DBD*: 18 kV) woods have *FWHM*s that, in general, range from 1.4 eV to 2.34 eV: *Tzalam* - from 1.42 to 2.1; *Caoba Mahogany* - from 1.75 to 2.38; and *Mexican white cedar* - from 1.0 to 1.91.

□ The $O_1$, $O_2$, and $O_3$, or O (1s) component, peaks of untreated woods have *FWHM*s that, in general, range from 1.8 eV to 2.44 eV: *Tzalam* - 2.38; *Caoba Mahogany* - from 1.97 to 2.44; and *Mexican white cedar* - from 1.8 to 2.0;

□ The $O_1$, $O_2$, and $O_3$, or O (1s) component, peaks of plasma treated (*DBD*: 12 kV) woods have *FWHM*s that, in general, range from 2.24 eV to 2.67 eV: *Tzalam* - from 2.45 to 2.67; *Caoba Mahogany* - from 2.40 to 2.63; and *Mexican white cedar* - from 2.24 to 2.25;

□ The $O_1$, $O_2$, and $O_3$, or O (1s) component, peaks of plasma treated (*DBD*: 18 kV) woods have *FWHM*s that, in general, range from 1.3 eV to 2.0 eV: *Tzalam* - from 2.17 to 2.37; *Caoba Mahogany* - from 2.53 to 2.57; and *Mexican white cedar* - from 2.3 to 2.58;

## *Conclusion*

Processes of woods preservation and bonding are usually achieved through the application of impregnation solution or adhesive on wood surface. Among the different mechanisms involved in the impregnation and bonding of woods, two synergistic effects seem essential in order to achieve good results:

□ The penetration and anchoring of the impregnation solution or adhesive in the void spaces of the wood surface;

□ The occurrence of a strong interaction or chemical reaction between the impregnate or adhesive and the major constituents of wood.

These conditions are governed by the surface properties that depend not only on the bulk composition, but also on the surface building and modification process.

*X*-ray photoelectron spectroscopy is a suitable investigation method to characterize the composition of wood surface. *XPS* is the most widely used surface analysis technique because of its relative simplicity in use and data interpretation. It was used successively to investigate the interaction of three rain-forest wood surfaces with cold non-equilibrium plasma of *DBD* in air at atmospheric pressure and room temperature.


## *Acknowledgments*

The authors gratefully acknowledge the financial support of Technical University - Sofia, for the Research Project 132ПД0051-01.

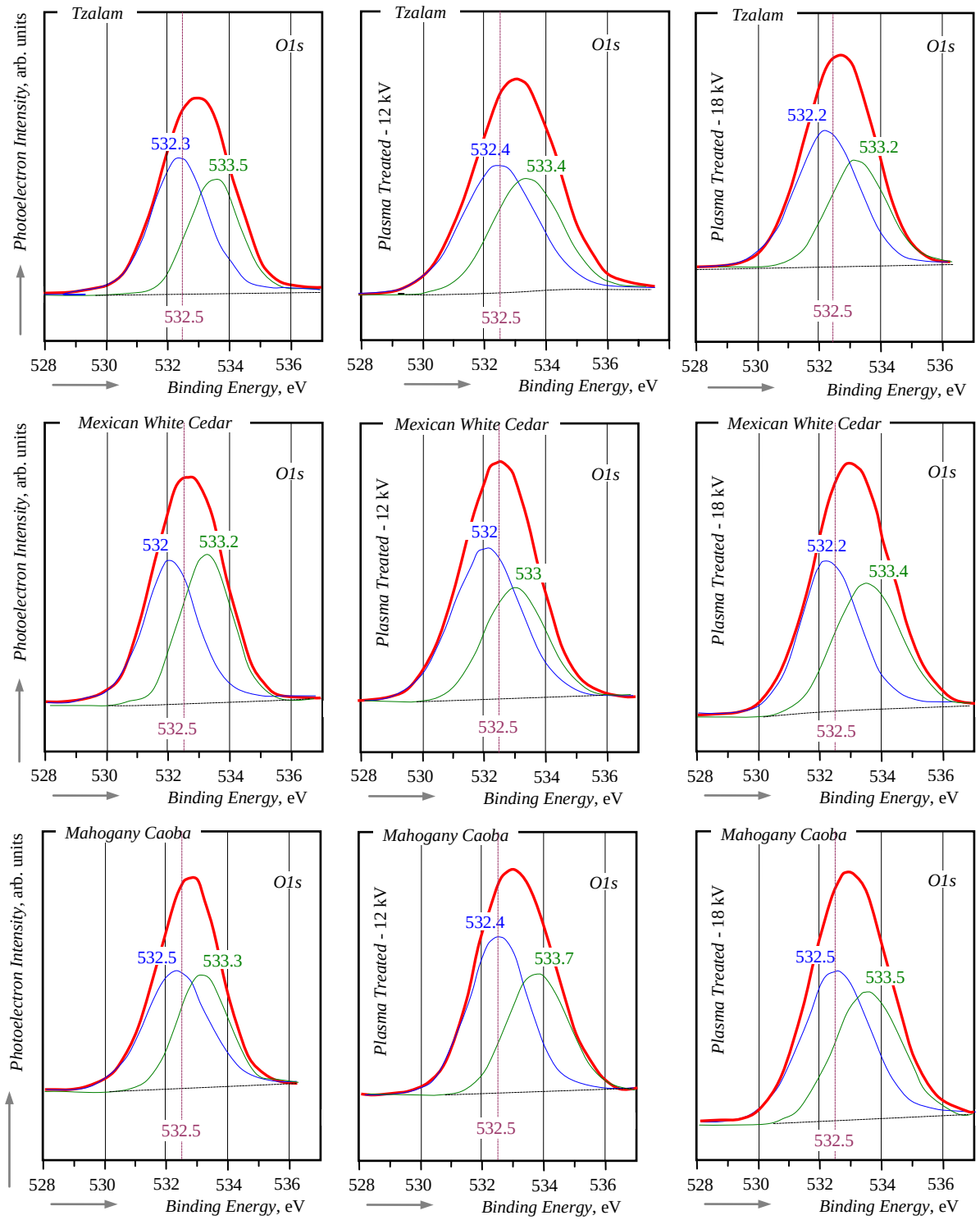



**Fig. 3.** Oxygen *O1s* peak in photoelectron *XPS/ESCA* spectra of bare sample of heartwood and 2 hours after plasma surface pre-treatment in atmospheric dielectric barrier air discharge at industrial frequency (50 Hz) and 12 and 18 kV (RMS) voltage.

## *References*


[1] Dineff, P., D. Gospodinova, L. Kostova, T. Vladkova, and E. Chen., *Plasma aided surface technology for modification of materials referred to fire protection*, Problems of Atomic Science and Technology, Series Plasma Physics (14), 2008, 6, pp. 198÷200.

[2] P. Dineff, L. Kostova. *Method for Plasma Chemical Surface Modification*. H05H 1/24, Bulgarian Patent Publication No.: BG 66022 B1; International Patent Publication No.: WO Patent 2006/133524 A2; Priority Date: 14.06.2005 (BG No. 109189).

[3] D. Gospodinova, I. Ivanov, P. Dineff, L. Veleva, and A. Gutierrez. *Plasma-aided flame retardation of Tzalam wood (Lysiloma bahamensis) - I and II*. Proceedings of Technical University of Sofia, 2012, vol. 62, issue 4, pp. 103÷122, ISSN 1311-0829.

[4] P. Dineff, I. Ivanov, D. Gospodinova, and L. Veleva. *Thermal behavior criteria of flame retarded wood obtained by simultaneous thermal analysis: I. New thermal behavior criteria of wood, and III. Thermal behavior criteria of plasma-aided flame retardancy wood*, XVIII-th International Symposium on electrical apparatus and technologies "SIELA'2014", May 29÷31, 2014, Bourgas, Bulgaria; P r o c e e d i n g s of full papers (in press).

[4] G. Nguila Inari, M. Petrissans, J. Lambert, J. J. Ehrhardt and P. Gérardin. *XPS characterization of wood chemical composition after heat-treatment.* Surface and Interface Analysis, 2006; vol.: 38: pp. 1336÷1342.

[5] G. Sinn, A. Reiterer, E. Stanzl-Tschegg. *Surface analysis of different wood species using X-ray photoelectron spectroscopy (XPS).* Journal of materials science, Springer, Heidelberg, Allemagne, 2001, vol.: 36, n°19, pp. 4673÷4680.

# INFLUENCE OF THE POSITION OF THE SWASH PLATE ROTATION AXIS ON THE VOLUMETRIC EFFICIENCY OF THE AXIAL PISTONS PUMPS

MSc. Eng. Zaluski P.
Gdansk University of Technology, Faculty of Mechanical Engineering, Hydraulic and Pneumatic Team – Gdansk, Poland

gorgopothamos@wp.pl

***Abstract:*** *The article describes the influence of the position of the swash plate axis of rotation on the size of the dead space and the volumetric efficiency of the axial pistons pump. Superposition of the two motions have been proposed - the rotation of the swash plate with respect to axis intersecting the axis of rotation of the pump shaft and the shifts of swash plate yielding a result of the rotation axis offset effect. In the article it is also made the comparison of the volumetric efficiency of the pump with the axis intersecting with the axis of rotation, and the construction with the shifted axis.*

**Keywords**: HYDRAULIC DRIVE, HYDRAULIC PUMPS, FLUID COMPRESSIBILITY

## *1. Introduction*

Axial piston pumps are one of pomp types used in power hydraulics. Such pumps are widely used due to their advantages – easy delivery control and high delivery pressures. Depending on structure, these pumps may be divided to pump types with swinging rotor and with swinging swash plate. Figure 1 shows the pump with swinging swash plate. When the shaft 1 rotates, the cylinder drum 5, which is mounted to the shaft, moves pistons 4. Piston feet 3 touch the swinging disk 2, thus forcing the reciprocating movement of pistons, when the cylinder drum rotates. Fixed timing gear 6 touches the cylinder drum, and it connects proper cylinders to either suction or delivery manifold. Pump delivery is controlled by changing disk 2 swing angle.

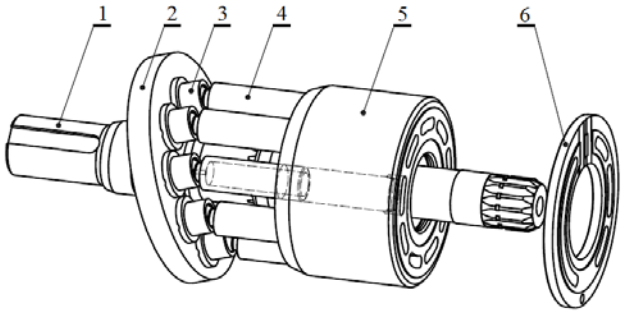



***Fig. 1*** *Construction of axial piston pump with swinging swash plate: 1-shaft; 2-swinging swash plate; 3-feet; 4-piston; 5-cylinder drum; 6-timing plat*[3].

For all solutions of serially produced pumps, the disk centre line intersects with the shaft centre line[1]. That is forced by structural demands – moments of forces balance with each other for such positions of centre lines only, therefore, relatively small force is needed to adjust the disk position. Such solution has one relatively serious disadvantage – when the disk angle is reduced, so called dead space increases, negatively influencing the volumetric efficiency, which, in particular, is well seen for small disk swing angles[3]. However, the effect of shifted centre line may be obtained by composition of two movements – rotation of the disk around its original centre line and additional disk movement. This is a subject matter of this article.

## *2. Volumetric efficiency*

The volumetric efficiency is a relation of actual flow intensity to theoretical flow intensity, which depends on piston travel and diameter and number of pistons, as well as on pump shaft rpms.

$$\eta_v = \frac{Q_{rz}}{D \cdot tg\varphi \cdot \frac{\pi \cdot d^2}{4} z \cdot n} \qquad (1)$$

Where $\eta_v$ is the volumetric efficiency, $Q_{rz}$ – actual flow, D – pistons spacing, φ – angle of the swash plate, d – diameter of the piston, z – number of pistons, n – speed of rotation.

Leakages are the first and main source of volume losses (see Fig. 2). These include, first of all, leakages supplying hydrostatic supports between piston feet and keep plate and between cylinder drum and timing gear disk. The leakages mentioned above are necessary for pump operation. They depend on delivery pressure and medium viscosity.

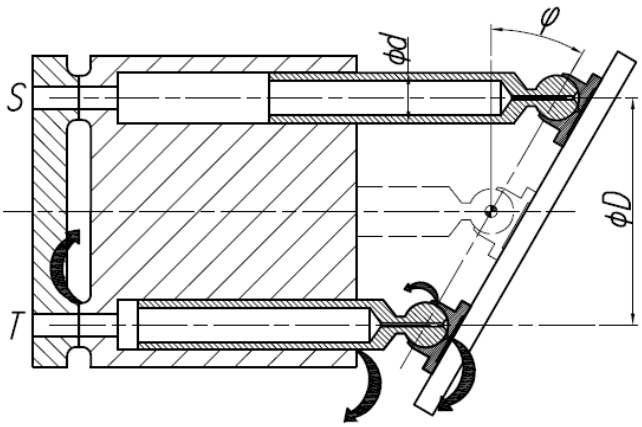



***Fig. 2*** *Main sources of leakages in the axial piston pump: S- suction manifold, T- delivery manifold.*

Medium compressibility is the other factor influencing the volumetric efficiency. It is seen for high pressures. The coefficient of compressibility β (formula 2)[2] determines the change in oil volume for increasing pressure. The bulk modulus K is a reverse of coefficient of compressibility, and it reaches the value of 1700 MPa for hydraulic oils[1].

$$\beta = -\frac{dV}{V_0} \cdot \frac{1}{dp} \qquad (2)$$

Where β is the coefficient of compressilibity, dV – variation of volume, dp – variation of pressure, $V_0$ – initial volume

### *3. Influence of compressibility of fluid in the dead space on the volumetric efficiency*

The dead space is the working chamber volume at the end of delivery phase. When the pump runs, each piston makes a reciprocating movement. During suction phase, the piston moves backward and the cylinder chamber is connected to suction manifold, and the medium is sucked. Then, for the extreme backward piston position, the suction manifold is disconnected and the delivery manifold is opened. The piston starts to move the timing gear plate and removes the medium from the cylinder. For the other extreme piston position, oil outflow is disconnected. The residual oil under high pressure is located in the dead space. Thus, when the suction manifold opens, the medium cannot be sucked at the beginning of cycle, because the oil contained in the dead space expands, causing back-flow to the suction duct (figure 3).

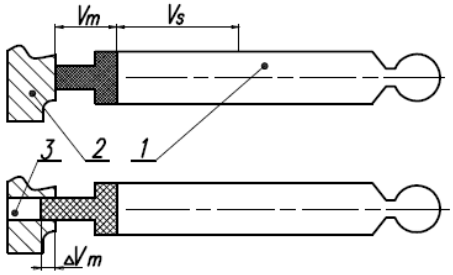



***Fig. 3*** *Back-flow of expanding fluid to the suction manifold: 1-piston; 2-timing plate; 3-suction manifold; $V_s$-displacement volume; $V_m$-death space volume; $\Delta V_m$-volume of the expanded fluid.*

Therefore, the volume of actually sucked oil is reduced, thus reducing the volumetric efficiency. The higher delivery pressure and the larger dead space, the higher influence of the phenomenon mentioned above. When neglecting leakages and focussing on phenomena resulting from liquid compressibility in the dead space, the pump volumetric efficiency is as follows[2]:

$$\eta_{vp}^{s} = 1 - \frac{V_m}{V_s} \cdot \frac{\beta \cdot \Delta p}{1 - \beta \cdot \Delta p} \quad (3)$$

Where $\eta_{vp}^{s}$ is volumetric efficiency without the impact of leaks, $V_m$ – volume of the death space, $V_s$ – displacement volume, β – compressilibity factor, Δp – increase of pressure.

### *4. Change the position of the axis of rotation of the swash plate*

For traditional axial-flow piston pumps, minimum dead space capacity corresponds to maximum disk swing angle. When reducing disk swing angle φ, the capacity of dead space increases according to the formula[4]:

$$V_m(\varphi) = V_{mmin} + \frac{\pi \cdot D \cdot d^2}{8} \cdot (tg\varphi_{max} - tg\varphi) \quad (4)$$

Where $V_m$ is volume of the death space, $V_{m\,min}$ – minimal volume of the death space for $\varphi_{max}$ [mm$^3$], D – pistons spacing, d – diameter of the piston

The relative dead space capacity ε may be defined by comparing the dead space capacity to the displacement volume[2]:

$$\varepsilon = \frac{V_m}{V_s} \quad (5)$$

For small disk swing angle values, the dead space capacity is even few dozen times larger than the displacement volume, resulting in considerable influence of medium compressibility in the dead space on volumetric efficiency.

Figure 4 shows three positions of swinging disk – position A with centre line (axis of rotation) in point 1 and swing angle $\varphi_{max}$, which corresponds to maximum pump delivery, position B with axis of rotation in point 1 and swing angle φ, and position C with shifted axis of rotation located in point 3 and swing angle φ. In case of traditional solution – i.e. when the disk axis of rotation crosses with shaft axis of rotation (point 1) – minimum dead space capacity $V_{m\,min}$ corresponds to maximum disk swing angle $\varphi_{max}$. When the disk axis of rotation is located in point 2, the dead space capacity is always constant, and it is $V_{m\,min}$. From meeting the condition that the dead space capacity is not less than $V_{m\,min}$ independently of disk swing angle value, it results that the disk axis of rotation may be located in any point of the straight line section, which connects points 1 and 2. Then, independently of position of disk axis of rotation, the dead space capacity will be $V_{m\,min}$ for disk swing angle value of $\varphi_{max}$.

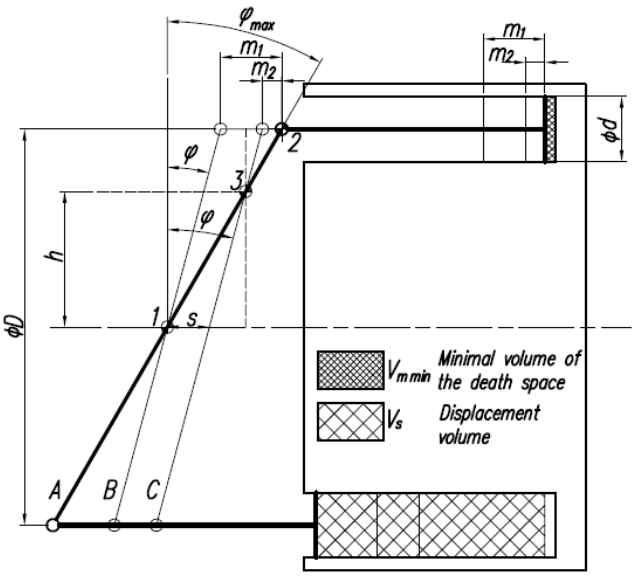



***Fig. 4*** *Influence of shifted axis and rotation of the swash plate on death space volume : A-swash plate with axis of rotation in point 1 and maximum swing angle; B-swash plate with axis of rotation in point 1 and swing angle φ; C-swash plate with axis of rotation in point 3 and swing angle φ.*

When the disk axis of rotation is located in point 1, the dead space capacity versus disk swing angle φ is described with formula (3). When the parameter h is introduced, which describes the location of disk axis of rotation:

$$h \in \langle 0, \frac{D}{2} \rangle \quad (6)$$

the formula for dead space capacity versus disk swing angle φ and position of disk axis of rotation h is obtained:

$$V_m = V_{mmin} + m_2 \cdot \frac{\pi \cdot d^2}{4} =$$

$$= V_{mmin} + \left(\frac{D}{2} - h\right) \cdot [tg\varphi_{max} - tg\varphi] \cdot \frac{\pi \cdot d^2}{4} \quad (7)$$

In order to obtain position C of the disk, where disk axis of rotation is located in point 3, the disk shall be rotated around axis of rotation 1 by an angle φ and move the disk towards the cylinder drum by s value:

$$s = h[tg\varphi_{max} - tg\varphi] \quad (8)$$

## 5. Object of research

The subject matter of testing is the pump, which is modified so that the disk swing angle may be changed and the disk may be shifted in the direction parallel to shaft centre line independently on each other. Combination of those two movements – disk swing angle, when the disk rotates around the axis crossing shat axis of rotation, and disk movement parallel to shaft axis of rotation – gives the effect of shift of disk axis of rotation. The basic parameters of the pump:

- spacing pistons D = 58mm
- piston diameter d = 14,15mm
- maximum swing angle of swash plate 15,56°
- minimal volume of the death space 4,274cm$^3$

The pump is shown in Figure 5. Swinging disk necks (3) are located in bearing half-sleeves mounted in a cradle (2). The disk axis of rotation crosses the shaft axis of rotation. The cradle may be moved in parallel to the drive shaft axis of rotation along the guides located in the front body part, cradle position is adjusted with the use of two adjusting screws (4). The disk swinging mechanism (1) is independent of disk shifting mechanism. The swinging disk is pressed against bearing half-sleeves with the use of pressing spring (5). Such pump structure makes possible testing the influence of position of disk axis of rotation on volumetric efficiency. Testing to compare traditional and modified positions of disk axis of rotation are made for the same pump model.

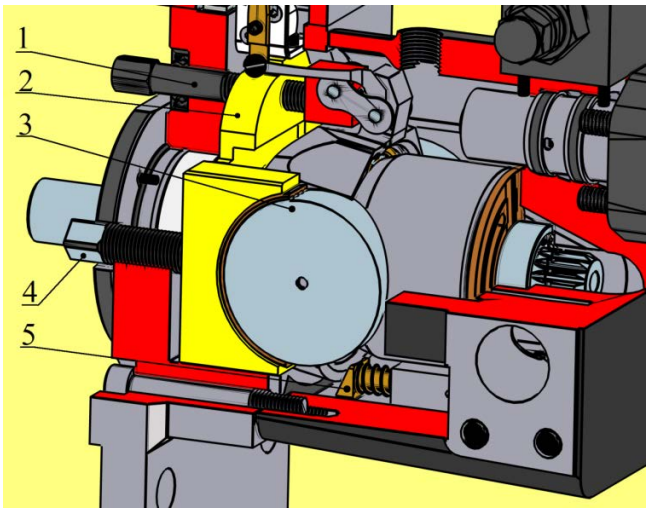



***Fig. 5*** *The pump, in which the swash plate may be moved in the direction paralel to the shaft centre line: 1-screw angle adjustment; 2-cradle; 3-swash plate; 4-screw adjustment of the cradle; 5-pressing spring*[4].

The diagram of testing station is shown in Figure 6. The tested pump is pre-supplied, so, overpressure of 0.2 MPa is in the suction duct. The pressure is measured upstream and downstream the pump. The intensity of flow is measured by means of the piston flow meter, and the pump is loaded with the use of relief valve. The disk swing angle is determined by measurement of adjusting screw projection. The results are compared with calculated disk swing angle for the lowest pumps delivery pressure (0.2 MPa), where the volumetric efficiency equal to 1 is assumed for that case.

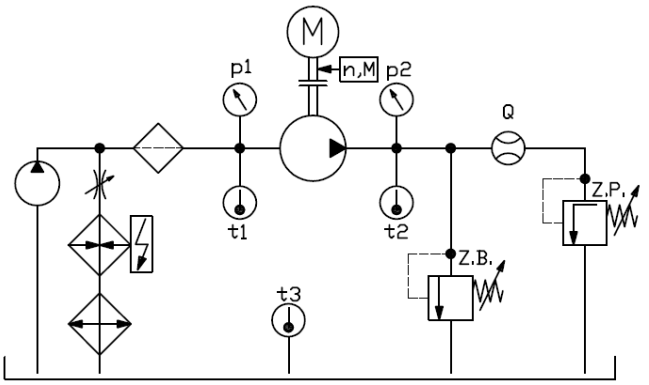



***Fig. 6*** *The diagram of testing station: p1, p2, p3- manometers; Q- piston flow meter; n- rpm measurement; M- torque measurement; t- termocouple; Z.B.- safety valve; Z.P.- relief valve.*

## 6. Research methodology and results

The testing is a comparative one, and its aim is to prove that the position and location of swing disk axis of rotation influences the volumetric effectiveness. The testing is carried out as follows – first, measurements of flow and rpms for traditional location and position of disk axis of rotation is carried out, while the pump load is increased gradually. Then, the disk is, without changing the disk swing angle, shifted towards the cylinder drum by such a value of s so that the effect of shifted axis of rotation is obtained (h = D/2). By shifting the disk towards the cylinder drum the dead space volume is reduced to obtain the value of $V_{m\,min}$ = 4.274 cm$^3$. The change of dead space volume depending on disk swing angle and location of its axis of rotation is shown in Figure 7. When the disk axis of rotation, which crosses the shaft centre line, the volume of dead space increases, when the disk swing angle is reduced. For the disk axis of rotation as shown at the right-hand side in Figure 7 (h = D/2), the volume of the dead space is constant and it does not depend on disk swing angle.

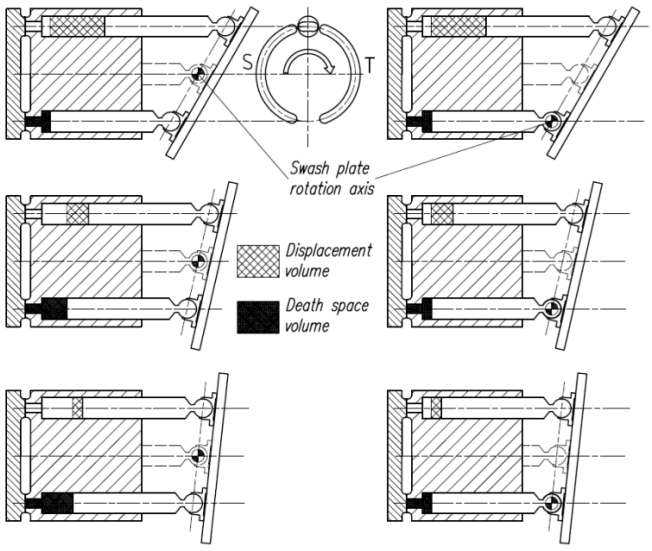



***Fig. 7*** *Influence of swing angle of swash plate and position of rotation axis of swash plate on death space.*

On the basis of formula (2), theoretical volumetric efficiency curves (see Figure 8) have been determined for parameters of the pump tested (with hollow pistons). Those values have been compared with pump version with solid pistons, for which minimum dead space capacity is reduced from 4.274 to 1.06 cm$^3$.

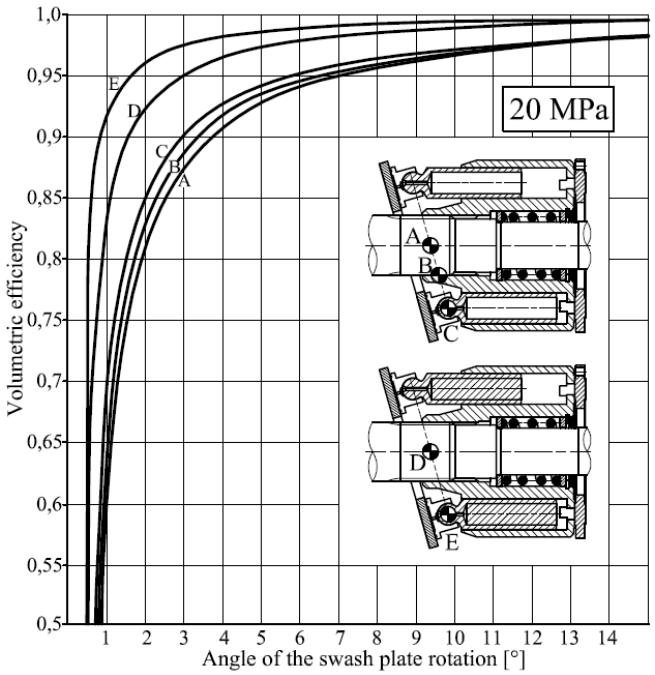



***Fig. 8*** *Influence of disk axis of rotation shift on the volumetric efficiency component resulting from medium compressibility in the dead space for the pressure of p = 20 MPa and oil bulk modulus of K = 1800; A-E – the positions of the axis of rotation of swash plate.*

At the beginning, measurements of flow intensity versus load pressure for constant rpms were carried out. On the basis of those measurements volumetric efficiency curves as a function of load were determined for various disk swing angles, as shown in Figure 9. For small disk swing angles, the volumetric efficiency is reduced considerably. For the swing angle of 1.2$^o$ and delivery pressure of 25 MPa, the volumetric efficiency is just 15 %. The data mentioned above are for disk axis of rotation, which crosses the shaft centre line.

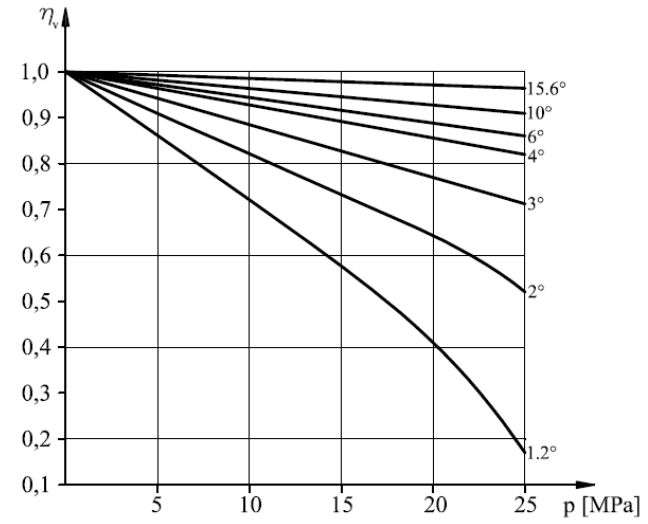



***Fig. 9*** *Volumetric efficiency versus delivery pressure for various disk swing angles for the pump tested. Intersecting the axis of rotation of the swash plate with the axis of shaft . 1000 rpm, viscosity 60cSt.*

Then, the results obtained were compared with the results of measurements obtained for disk axis of rotation shifted by the value of h = D/2. The comparison of the results mentioned above is shown in Figure 10.

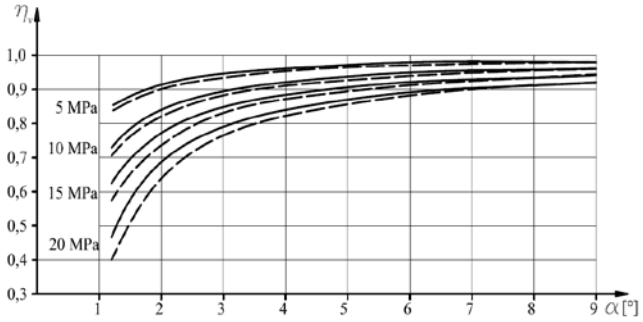



***Fig. 10*** *Comparison between volumetric efficiencies of the pump with disk axis of rotation crossing the shaft centre line (broken line) and the pump with the disk axis of rotation shifted by the value of h = D/2 (full line) in relation to disk swing angle and delivery pressure. Measurements for n = 1000 rpm and oil viscosity of 80 cSt.*

## *7. Conclusions*

The testing made as above shows that the volumetric efficiency increases, when the disk axis of rotation is shifted. In particular, the volumetric efficiency increase is seen for small disk swing angles and high delivery pressures. For a given pressure and oil viscosity, leakages do not depend on location and position of the disk axis of rotation. Therefore, the increase in efficiency is connected with reduced dead space capacity. Further testing was made for delivery pressures up to 35 MPa for various oil viscosity and rpms. The measurements already made confirm the influence of oil compressibility in the dead space on the volumetric efficiency.

## *8. References*

[1] Osiecki A., *Hydrostatyczny naped maszyn*, WNT, Warszawa 2004

[2] Osiecki L., *Mechanizmy rozrzadu hydraulicznych maszyn wielotloczkowych osiowych*, Wydawnictwo Politechniki Gdanskiej, Gdansk 2006

[3] Zaluski P., *Zaleznosc sprawnosci objętosciowej pompy z wychylna tarcza od przemieszczenia osi obrotu tarczy*. Wspolczesne technologie i konwersja energii, Wydawnictwo Politechniki Gdanskiej, Gdansk 2012

[4] Zaluski P.,*Wpływ położenia osi obrotu tarczy wychylnej na sprawnosc objetosciowa pomp wielotloczkowych osiowych*, Hydraulika i Pneumatyka nr 1/2014

# MODELING AND OPTIMIZATION OF THE PROPERTIES AND COMPOSITION OF TITANIUM-BASED ALLOYS

Nikolay Tontchev Yordan Kalev Rumyana Lazarova*
University of Transport – Sofia tontchev@vtu.bg *IMSET with CHA - BAS

***Abstract:*** *The possibilities of regression analysis to model the properties and the related to it multicriteria optimization of the composition of titanium alloys are introduced in the presented research. This is done after performing characteristics of established applications of various titanium alloys. To predict elongation in this paper there have been obtained nonlinear regression models that allow to estimate the strength properties and the plasticity depending on the equivalents for aluminum and molybdenum for titanium alloys.*

**Key words**: METALLURGICAL DESIGN, TENSILE PROPERTIES, COMPOSITION-PROCESSING-PROPERTY CORRELATION

## *1. Introduction*

Analysis of international trends and forecasts in the use of metal alloys up to year 2020 shows that titanium alloys are promising materials of general-purpose worldwide engineering [1].

Despite the economic uncertainty in the world economy, over the past years there was a steady demand for titanium products, which was a result of high rates of development of the aerospace sector – the main consumer of titanium products. In the international scientific community there is a continuous research of new ideas about the applications of titanium alloys in various industries, and, above all, the emphasis is put on areas with importance of the quality of the final product, but not in commercial aerospace and aeromechanics [2, 3], military industry (Figure 1)

A lot of attention in the development and improvement of titanium alloys for various applications is dedicated to the problem of effective alloying materials the solution of which leads to improved basic operating parameters of the alloys. The structural strength of materials plays an important role in ensuring a reliable long-term operation of machine parts and assemblies. Creation of new equipment in aviation, engineering, oil-, gas- and other industries imposes more stringent requirements for higher performance of the designs. This necessitates the use of materials with a higher set of physical and mechanical properties. For metallic materials, this problem is solved either by creating new alloy compositions, or by the development of new high-performance thermomechanical methods targeting the structure of industrial production of alloys.

Over the years, the research of titanium and its led to much experimental, theoretical and practical experience in the metal science, thermal and mechanical treatment, such as: basic principles of alloying titanium alloys were well-grounded, the methods and modes of heat treatment were developed, the basic dependencies of various mechanical properties were established on the chemical composition, structure, modes of thermal, thermo-mechanical, etc. operation.

The results of these studies are summarized in a series of monographs and reference works [4]. As a result, to date there is collected extensive material for statistical research that can be used to elaborate methods for predicting mechanical and technological properties of titanium alloys according to different criteria, such as the chemical composition.

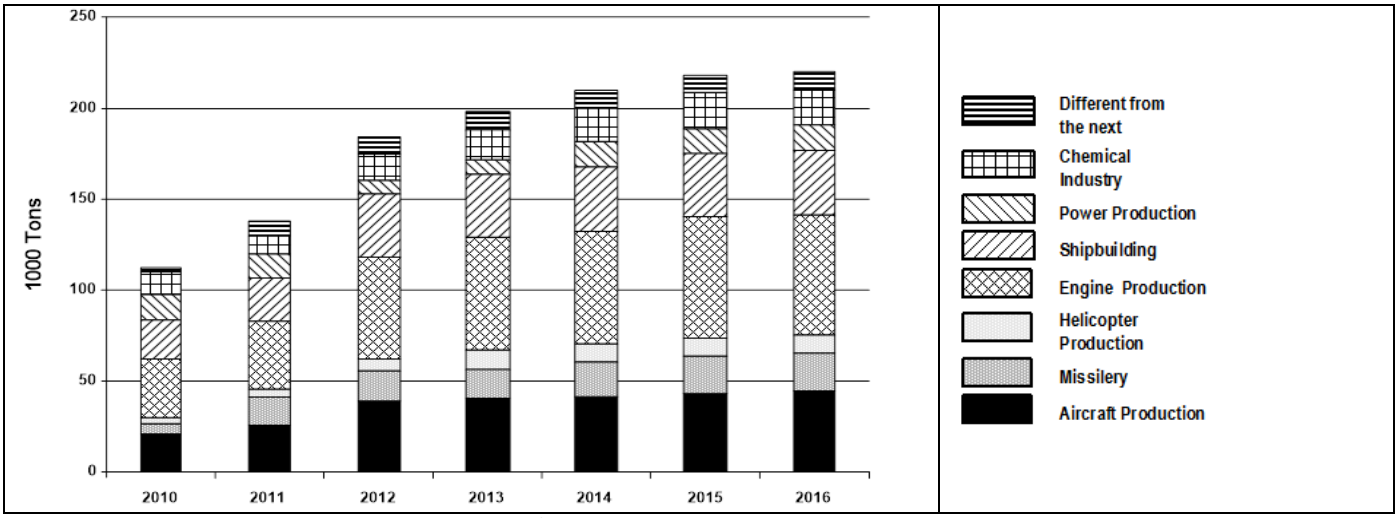



***Fig 1.*** *World consumption of titanium alloys according to applications and along the years [1]*

## *2. Characteristics of titanium alloys and their superior criteria for classes*

To obtain predetermined mechanical properties of titanium it is alloyed with aluminum, vanadium, manganese, molybdenum, chromium, iron and some other chemical elements. Introducing alloying elements in certain combinations and quantities, as well as targeted thermal effect, allow to change the properties of alloys in a wide range. The ultimate tensile strength of commercial titanium alloys can be varied from 400 MPa for low-alloyed soft alloys and up to 1600 MPa for the high-heat-strengthened alloys.

Relatively To obtain predetermined mechanical properties of titanium it is alloyed with aluminum, vanadium, manganese, molybdenum, chromium, iron and some other low density in combination with relatively high-strength characteristics of titanium alloys provides a higher specific strength (ratio of strength characteristics to density) in a wide range of temperatures, as compared to aluminum alloys, steels and heat-resistant nickel alloys.

This circumstance is the decisive factor in determining the preference of use of titanium in aircraft and aerospace engineering. Titanium alloys retain their inherent strength characteristics up to a relatively high temperature. Best heat-resistant titanium alloys can operate at temperatures 600-650 ° C.

| Class of alloys | | Rm, MPa | ρ g/cm$^3$ | Rm/ρ, MPa cm$^3$/g |
|---|---|---|---|---|
| **Titanium alloys** | Low-strength<br>Middle-strength<br>High-strength | 400-700<br>700-1000<br>>1000 | 4,5-4,55<br>4,4-4,5<br>4,65-4,75 | 88,4-154,6<br>157-225<br>>213 |
| **Alluminium alloys** | Low-strength<br>Middle-strength<br>High-strength | 130-300<br>350-500<br>>500 | 2,7<br>2,85<br>2,85 | 48,1-1 14<br>123-175<br>>175 |
| **Steels** | Conventional<br>Low-alloyed<br>Middle-alloyed<br>High-strength | 300-700<br>400-850<br>850-1500<br>>1500 | 7,8<br>7,8<br>7,8<br>7,8 | 38,5-89,7<br>89,7-109<br>109-192<br>>192 |

***Table 1**. Comparison of the level of strength for steels, titanium and aluminum alloys [1]*

Table 1 presents a comparison between the strength and the density of steels, titanium and aluminium alloys.

Specific features and unusual functional characteristics of special titanium alloys significantly expand the scope of their use. Criteria for competitiveness for various titanium alloys are presented in Table 2.

| Titanium alloys | Application criteria |
|---|---|
| Technical titanium | Mass, corrosion resistance, stiffness, deformability, appearance |
| α + β – alloys, titanium aluminides | Mass, high-temperature strength/resistance, oxidation resistance, durability, strength |
| β –alloys | Mass, high strength, spring characteristics, cold formability |
| Titanium aluminides | Heat resistance |
| Titanium-nickel alloys | Mass, corrosion resistance |
| Titanium-nickel alloys | The shape memory effect |

***Table 2.** Criteria for various titanium alloys, related to their competitiveness*

The numeric design of the composition and the operative technological parameters in metallurgy is a problem of particular complexity due to its multivariate nature. There is a need for continuous improvement of the whole industry in order to improve the properties of alloys with broad application.

This research is part of series of approaches and methodologies that at the stage of generating the decision do not use the knowledge gained in the field of metallurgy. The proposal has the potential to predict the mechanical properties of alloys, like in [t13], using prior information of data linking composition, processing and properties. The cited monograph explores the iron-based alloys, thus confirming the thesis for evaluation of these alloys numerically and experimentally. This methodology is the way to design alloys at a predetermined database.

## *3. Formulation of the problem*

The results from the analysis of the models and the optimization can provide a guideline for further experimental and computational investigation [6, 7].

Instead of performing real experiments, the computational design approach combines physical models of known interactions, compositions, processing, properties to predict the alloy composition and the related to it set of characteristics [8].

The increase in the number of variables is considered usually to lead to a drastic increase in the complexity of physical models, which causes the calculation to be much more time-consuming and demanding for computation capacity [9].

That is why the developed by us procedures and algorithms [5] are realized for a fixed processing mode. Therefore it is of practical importance and also it is necessary to expand the task to understand the relation between the composition, the processing and the properties which would allow a quick evaluation for the alternation of composition and of the processing route.

The purpose of this research was the statistical comparison of strength and plastic properties for titanium alloys of different classes depending on their chemical composition, expressed as equivalents for aluminum and molybdenum.

This paper includes an example illustrating the relationship between the composition and the properties and modeling capabilities in this direction. Thereby it is possible to evaluate the basic properties depending on a popular summary of the alloy composition based on two widely used equivalents [1].

To calculate equivalents for aluminum and molybdenum there was used the average chemical composition of 18 industrial alloys. In references [4] on the basis of summarizing a large amount of literature and experimental data there are cited the most typical values of the mechanical properties, i.e. values close to the average estimates. The used data base is presented in Table3. Related to the specific composition of each alloy there are defined two quantities of aluminum and molybdenum equivalents described as follows [1]. The mechanical properties of titanium alloys strongly depend on the thermal treatment. The data shown in Table 3 are derived from the same heat treatment - Annealing (α + β)

$$Al = \%Al + \%\frac{Sn}{3} + \%\frac{Zr}{6} + 10\left(\%O + \%C + 2(\%N)\right);$$

$$Mo = \%Mo + \%\frac{Ta}{4} + \%\frac{Nb}{3{,}3} + \%\frac{W}{2} + \%\frac{V}{1{,}4} + \%\frac{Cr}{0{,}6} + \%\frac{Ni}{0{,}8} + \%\frac{Mn}{0{,}6} + \%\frac{Fe}{0{,}4}.$$

These two equivalents carry information for alloying, because they are calculated for the various combinations of the alloying elements.

For comparison and optimization of titanium alloys it is possible to use structural and strength equivalents to aluminum and molybdenum, proposed in [1]: molybdenum and aluminium equivalents are integral characteristics describing the effect of alloying elements on the structure, the phase composition and the strength of titanium alloys. The structural equivalent to the total effect of aluminum characterizes the impact of α- stabilizers and neutral reinforcers on the phase composition of alloys (intermetallic formation conditions α). The formation of phase α leads to a sharp decrease in ductility, and in the thermal stability of alloys. The phase is not formed if the equivalent structure on aluminum does not exceed 9%. α- stabilizers are alloying elements that increase the temperature of the polymorphic transformation of titanium. These include aluminum, carbon, nitrogen, oxygen. The structural equivalent of molybdenum characterizes the total effect of β-stabilizing elements on the phase composition of alloys (number of β-phase, its stability, the ability to phase transformations). β- stabilizers are elements that reduce the temperature of the polymorphic transformation of titanium. They can be divided into zoomorphic (vanadium, tungsten, molybdenum, etc.) and eutectoid (chromium, manganese, cobalt, etc.).

This example shows the effect from alloying complexity related to the quantities and also to the alloy elements, over the basic mechanical parameters - Rm - ultimate tensile strength, Rp0.2 - tensile yield strength, E - elongation.

| № | alloy | Mo –ekv $X_1$ | Al-ekv $X_2$ | Rm [MPa] | Rp0.2 [MPa] | E [%] |
|---|---|---|---|---|---|---|
| **1** | Ti-6Al-2Sn-1.5Zr-1Mo-0.35Bi-0.1Si | **1,375** | **8,12** | **937** | **848** | **16,0** |
| **2** | Ti-3Al-2.5V | **2,161** | **4,2** | **690** | **627** | **20,0** |
| **3** | Ti-6AI-2Sn-4Zr-2Mo | **2,375** | **8,53** | **1000** | **930** | **15,0** |
| **4** | Ti-8Al-1Mo-1V | **2,089** | **9,2** | **1000** | **930** | **12,0** |
| **5** | Ti-10V-2Fe-3Al | **12,14** | **4,2** | **970** | **900** | **9,0** |
| **6** | Ti-13V – 11Cr-3Al | **27.99** | **4.2** | **950** | **860** | **18** |
| **7** | Ti-6AI-2Sn-4Zr-6Mo | **6,375** | **8,53** | **1030** | **970** | **11,0** |
| **8** | Ti-6Al-4V (Grade 5) | **3,232** | **7,2** | **950** | **880** | **14,0** |
| **9** | Ti-6Al-6V-2Sn | **4,661** | **7,87** | **931** | **807** | **18,0** |
| **10** | Ti-7Al-4Mo | **4,375** | **8,2** | **1030** | **970** | **12** |
| **11** | Ti-5Al-5Sn-2Zr-2Mo-0.25Si | **2,375** | **8,2** | **730** | **552** | **20,0** |
| **12** | Ti-5Al-6Sn-2Zr-1Mo-0.25Si | **1,375** | **8,53** | **720** | **550** | **17,0** |
| **13** | Ti-4Al-3Mo-1V | **4,089** | **5,2** | **860** | **860** | **10,0** |
| **14** | Ti-5Al-1.5Fe-1.4Cr-1.2Mo- | **7,283** | **6,2** | **1061** | **1020** | **14,0** |
| **15** | Ti-5Al-2.5Fe | **6,25** | **6,2** | **860** | **780** | **9,0** |
| **16** | VT14 | **4,475** | **6,1** | **883** | **873** | **10,0** |
| **17** | VT16 | **8,589** | **3,5** | **814** | **716** | **8,0** |
| **18** | Ti (99.5) | **0,375** | **1,2** | **331** | **241** | **30** |

***Table 3****. Relationship between variables and equivalents percentage*

## *4. Results*

Based on this information from Table 3, nonlinear regression models are derived establishing the relation between the complex composition and the properties.

The software package DSTAT [10] was used for statistical analysis.

Table 4 presents the coefficients of the regression models derived for coded values of the variables. Passive-experiment data affect the accuracy of the models, but nevertheless the models are adequate and they can be used for prediction. Fig. 2 introduces graphical interpretations of the displayed models

| **Characteristics** / **Coefficient** | **Rm [MPa]** | **$Rp_{02}$ [MPa]** | **E [%]** |
|---|---|---|---|
| Free coefficient | 990.168 | 1008.96 | 10.7753 |
| $b_1 * X_1$ (Mo ekv) | 179.100 | 185.366 | -2.29775 |
| $b_2 * X_2$ (Al ekv) | 342.250 | 380.970 | -5.27148 |
| $b_{11} * X_1^2$ | -102.675 | -185.659 | 8.37208 |
| $b_{12} * X_1 X_2$ | 85.8673 | 202.658 | - |
| $B_{22} * X_2^2$ | -106.736 | -123.784 | - |
| R | 0.8834 | 0.8016 | 0.6753 |
| F computing | 8.5277 | 4.3135 | 3.9131 |
| F tabl. meaning | 3.1059 (α = 0.05, 5, 12) | 3.1059 (α = 0.05, 5, 12) | 3.3439 (α = 0.05, 3, 14) |

***Table 4****. Coefficients and parameters of regression models describing properties depending on molybdenum and aluminum equivalents*

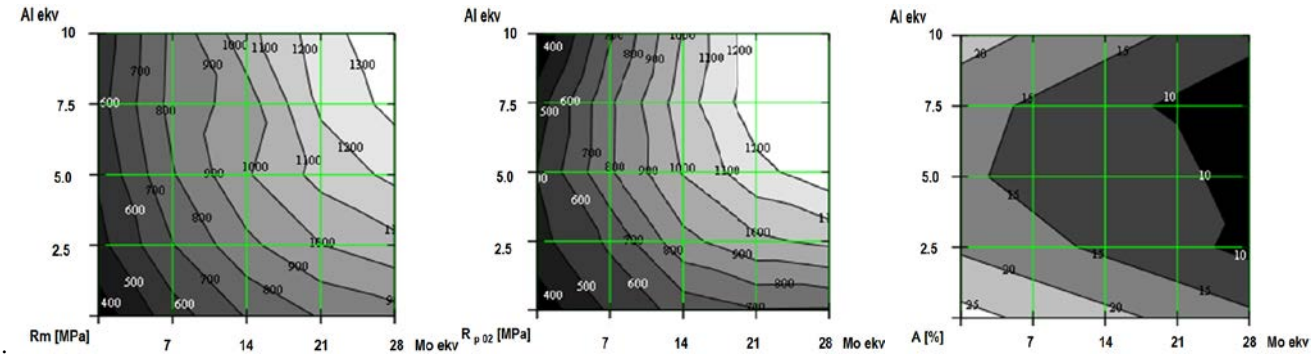



***Fig. 2****.Changes of mechanical properties - Rm - ultimate tensile strength, Rp0.2 - tensile yield strength, E-elongation depending on the aluminum and molybdenum equivalents.*

The contradiction between plastic and strength characteristics stands out from all attached graphics, including vector graphics depicted in Fig. 3. High strength is observed for high values of aluminium and molybdenum equivalents. Plasticity is relatively low for these values of the equivalents.

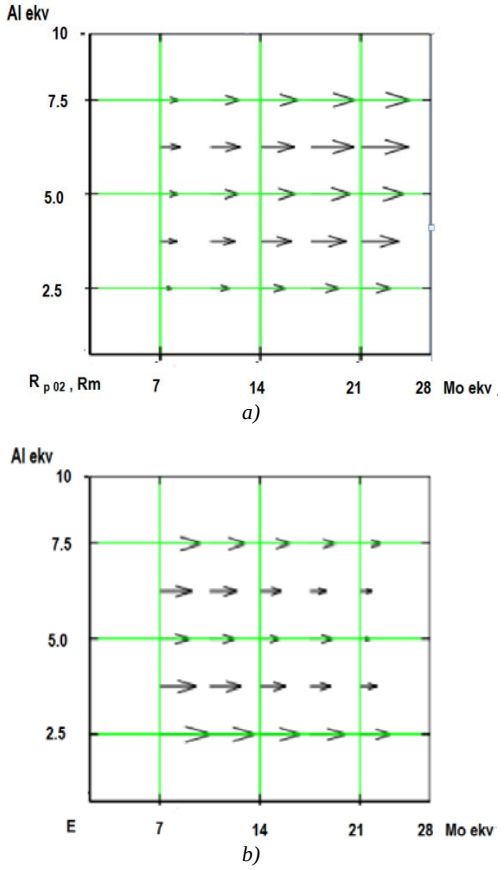



***Fig. 3**. Vector representations of: Rp0.2 – tensile yield strength, Rm – ultimate tensile strength – a) and for E – elongation b), depending on molybdenum and titanium equivalents.*

The resulting regression models listed in Table 3 make it possible to define the multicriteria problem, by means of which to determine optimal values of aluminum and molybdenum equivalents for which strength and plastic properties are relatively maximal. This procedure is described in detail [11]. As a result of applying the procedure in Table 5 are shown the following optimal values.

| Input parameters of optimal characteristics | | Optimal values of the investigated characteristics | |
|---|---|---|---|
| | | for elongation E | For yield strength $R_{p\,02}$ |
| Mo ekv /$X_1$/ | Al ekv /$X_2$/ | 16.8 [ %] | 1008 [MPa] |
| 28 % /1/ | 5.2 % /0/ | Percentage of the determined decision related to the maximum value | |
| | | 53.6 [%] | 60.60 [%] |

***Table 5**. Optimal values of the investigated characteristics*

## *Conclusion.*

In the presented research are introduced the possibilities of regression analysis to model the properties and the related to it multicriteria optimization of the composition of titanium alloys. This is done after performing characteristics of established applications of various titanium alloys. For clarity of results the option is a bidimensional case, expressed by aluminum and molybdenum equivalents. The applied methodology is solved for ten variables

## *References.*


**1.** **Ilyin A.A.** Titanium alloys. The composition, structure and properties. Handbook / **A.A.Ilin, B.A.Kolachev, I.S.Polkin** - M.: VILS-MATI, 2009, 520 pp. (in Russian)

**2.** **Schulte R**. Innovation, including use of titanium, drives airbus success / Rick Schulte // Aerospace Digital Edition of Titanium Today - 2013 . - Issue number 1 2 - P.70- 71

**3.** Annual Report 2012 OAO "Corporation VSMPO-AVISMA". http://www.vsmpo.ru/files/user_groupes/Administrator/Section/235/Godovoi_12.pdf – Michail Metz Russian Titanium market. Demand forecast. History and forecast 2010 – 2017/ Materials report on international conference "Titanium 2013" – March 5-7, 2013, Hamburg, Germany, Titanium Europe 2013 – Executive Summary // Aerospace Digital Edition of Titanium Today – 2013. – Issue 2 №1 – pp.60-69.

**4.** **Malinov, S, Sha, McKeown, J.J**.: Modelling and Correlation between Processing Parameters and Properties of Titanium Alloys using Artificial Neural Network. Computational Material Science 21, 375--394 (2001)

**5.** **Tontchev N**. Materials Science, Effective solutions and Technological variants, 2014/3/3, LAMBERT Academic Publishing

**6.** **Maier M.F., K. Stowe and S. Sieg**, "Combinatorial and high-throughput materials science", Angewandte Chemie-International Edition 2007, 46:6016-6067

**7.** **Fischer C.C, K.J. Tibbetts, D. Morgan and G. Cedar**, "Predicting crystal structure by merging data mining with quantum mechanics", Nature Materials 2006, 5:641-646

**8.** **Vitos L., P.A. Korzhavyi and B. Johansson**, "Stainless steel optimization from quantum mechanical calculations", Nature Materials 2003, 2:25-28

**9.** **Borst R.** de, "Challenges in computational materials science: Multiple scales, multi-physics and evolving discontinuities", Computational Materials Science 2008, 43:1-15

**10.** **Vuchkov, I., & Stoyanov, S.** (1980). Mathematical modeling and optimization of process units. Sofia: Engineering, (In Bulgarian).

**11.** **Tontchev N.., L. Kirilov** , Two Approaches for Solving Multiple Criteria Decision Making (MCDM) Problems with an Illustrative Example, PROBLEMS OF ENGINEERING, CYBERNETICS AND ROBOTICS, 58, 2007, 53-63 2007

# INTELLIGENT DECISION-MAKING FOR ENERGY AND ECONOMIC EFFICIENCY OF INNOVATIVE MANUFACTURING PROCESSES BASED ON MULTI-ATTRIBUTE KEY PERFORMANCE INDICATORS

M.Sc. Grzelak D.[1], Dipl.-Wirt.-Inf. Freund R.[1], Dr. Wiemer H. [1], Prof. Großmann K. [1]
Institute of Machine Tool and Control Engineering, Technical University of Dresden, Dresden, Germany [1]

Dominik.Grzelak@tu-dresden.de

***Abstract:*** *Production planning for the replacement of conventional manufacturing systems by new automated process chains is a complex activity particularly when it comes to choosing the right processes, materials and technologies. Nowadays those new process chains have to fulfil constraints such as low energy consumption and have to be resource-efficient and cost-efficient at the same time. The decision-making process can be a difficult task for authorities especially when the uncertainty of the input parameter has to be taken into account, such as prices for electricity, raw materials and lot sizes. This paper proposes a new decision-making model based on multidimensional key performance indicators (KPIs) that represent an economic and environmental objective as well as a performance objective.*

**Keywords**: MANUFACTURING, LEIGHTWEIGHT STRUCTURES, DECISION-MAKING, ENERGY-EFFICIENCY, COST-EFFICIENCY

## *1. Introduction*

The Designing of hybrid lightweight structures are becoming increasingly more interesting in research and industry. New hybrid materials are developed, consisting of multiple materials like e.g. thermoplastic textile composite components made of plastic and glass fibre, for the realization of lightweight construction concepts and allow a significant weight reduction whilst still providing a high mechanical strength and functional density [1] and can lead to reduced operational costs. For example in the automobile sector the use of lightweight structures can lead to energy savings through weight reduction [2] and in return leads to less fuel consumption. Currently developments of those hybrid structures are limited to niche applications and require the need for innovative process chains, technologies, tools, and the use of hybrid materials.

For accomplishing the goal for the construction of hybrid structures, new machines and tools are used, whereby basic technologies are "merged" together to realize new innovative merged process chains. By using those merged process chains in existing manufacturing facilities, the complexity of the whole manufacturing process can be reduced as well as it allows a resource and economic efficient production and development. But the complexity in the planning phase of those new composite constructions leads to long development times, high financially expenditure and detailed expert knowledge.

In manufacturing chains with a wide variety of materials, machines, tools and production levels, evaluation and comparison of various alternative process chains only consider cost aspects [3] or allow only insight to the energy consumption of processes [4]. Rarely an overall evaluation of the ecological *and* economic factors is conducted.

Choosing from multiple alternatives e.g. the best technology, tool and material is a difficult task for decision-makers, manufacturing supervisors or production managers. Furthermore constraints like low energy consumption and resource efficiency are a basis for discussion in the present time and have to be observed taking account of a robust product. A multi-criteria decision-making (MCDM) support for economic and energy efficiency is essential and can help to drastically cut long development times and costs especially in the early phases of planning, especially when only a small amount of series of tests are carried out and therefore minimum data is available.

MCDM can be used to find the "best" alternative under all available options at the same time considering many, often conflicting criteria and making assumption to different constraints. This paper illustrates a simple but effective approach to multi-attribute decision-making of automated process chains for planning and development in the early phases of production.

## *2. Methodology of MCDM Design*

The decision-making process can be divided into the following 5 steps as depicted in Fig. 1:

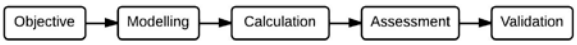



***Fig. 1*** *General procedure of the multi-criteria decision analysis.*

The first step includes discussion of the current state, formulating the problem to solve and listing comparable process chains or single processes, examining available information (this raises issues about the extent of parameters, which can be measured, approximated or are available) and describing the objective that raising the question: What are the constraints and which goals have to be reached for choosing the best process chain?

The next steps of this procedure model will be illustrated in the following sections.

### *2.1 Model*

The decision matrix $M$ describes the performance of the alternatives (as rows) with respect to selected criteria (as columns) and is defined as set $M = \{\mathbf{A}, \mathbf{C}, \mathbf{W}\}$, where $A_i, i = 1, \dots, n$, denotes the $i^{\text{th}}$ process chain, $\mathbf{C} = (c_{ij}),\ j = 1, \dots, m$, the attribute matrix, where every column formally represents a criterion, and $w_j\ (j = 1, \dots, m)$ the corresponding weights:

$$\mathbf{C} = \begin{bmatrix} c_{11} & \cdots & c_{1j} & \cdots & c_{1m} \\ \vdots & \ddots & \vdots & \ddots & \vdots \\ c_{i1} & \cdots & c_{ij} & \cdots & c_{im} \\ \vdots & \ddots & \vdots & \ddots & \vdots \\ c_{n1} & \cdots & c_{nj} & \cdots & c_{nm} \end{bmatrix}, \quad \text{with} \quad c_{\cdot j} \mapsto w_j \tag{1}$$

The attributes represent the model values against which the alternatives will be evaluated (cf. [5, p. 52]) and are partitioned in two levels with $M = 3$ upper level criteria, representing the three indicators $I\ (I = 1, .., M)$, which we will describe shortly, and overall $m = 12$ lower level criteria (see section 2.2). Let $L_I$ be the set of the lower level criteria for the first indicator $(I = 1)$, namely the economic objective then $L_1 = \{1,2,3,4\}$; the environmental objective with $I = 2$ is formulated as $L_2 = \{5,6,7,8,9\}$, and the performance objective with $I = 3$ is represented by $L_3 = \{10,11,12\}$. The model values for the alternative $A_i$ can then be formulated as vector $A_i = \{c_{i1}, c_{i2}, c_{i3}, c_{i4}, c_{i5}, c_{i6}, c_{i7}, c_{i8,} c_{i9}, c_{i10}, c_{i11}, c_{i12}\}$ with the corresponding weights $w_j = \{w_1, \dots, w_{12}\}$.

### *2.2 Model Values*

The model values are based on three different multidimensional key performance indicators (KPIs) as already mentioned above, which represent an (i) **economic**, (ii) **environmental** and

(iii) **performance** objective. The term indicator and upper level criterion will be used as synonyms for KPI throughout the paper. The KPIs are calculated from real data of first series of tests or can be approximated. At the same moment they have the same function like constraints (see section 2.3). The criteria are arranged in two hierarchical levels with three upper level criteria (the KPIs) and overall 12 lower level criteria. An attribute is a property of an alternative to be evaluated. That means $I = 1$ has four lower level criteria, $I = 2$ has five sub-criteria, and three other lower level criteria belonging to upper level criterion $I = 3$. As mentioned before the attributes are evaluated against the alternatives, so that they are also called criteria, because of the one-to-one correspondence, concerning the evaluation of an alternative. Table 1 shows the KPIs with their related sub-attributes, the unit of measurement, and the direction in which they should be optimized.

***Table 1:*** *The criteria represented by the three KPIs are displayed and subdivided into their related attributes which form the corresponding KPI. The unit of measurement is listed as well. The direction of the optimization for the decision-making is displayed in the last column for every attribute. Component is abbreviated with comp.*

| KPI | Sub-attribute | Unit | Direction |
|---|---|---|---|
| Economic | | | |
| | Production Overhead | [€/Comp.] | Min |
| | Material Costs | [€/Comp.] | Min |
| | Personnel Costs | [€/Comp.] | Min |
| | Total Costs of Process Chain | [€/Comp.] | Min |
| Environmental | | | |
| | Energy Costs | [€/day] | Min |
| | Energy Costs | [€/month] | Min |
| | Energy Costs | [€/year] | Min |
| | CO2 Emissions | [CO2 of kg /year] | Min |
| | % of Renewable E. | [%] | Max |
| Performance | | | |
| | Production Volume | [Comp./day] | Max |
| | | [Comp./month] | Max |
| | | [Comp./year] | Max |

Even though the KPIs are formed by different attributes with different unit of measurements the strength of MCDM is shown here, because it can handle the hybrid nature of the unit of measurements of various attributes. For example *material costs* is measured by euro per component, and *production volume* has the unit components per day. Also qualitative and quantitative attributes can be mixed.

Suppose we have two process chains, $Q$ and $C$, of length $n$ and $m$, respectively, where

$$Q = q_1, q_2, \dots, q_n, \tag{2}$$

$$P = p_1, p_2, \dots, p_m, \tag{3}$$

and $q_i$ and $p_i$ represent one process with their related machine, tool or material. The decision model is designed with its KPIs to compare different kind of process chains, no matter of what length they are or of which machines and tools they consist of. Each KPI is firstly calculated independently for every process in the chain before they get merged to one value as illustrated in (Fig. 2). That approach has the advantage that also numerous new features can be introduced into the model. Statistical values can be calculated (e.g. averages, standard deviations etc). For example this was done to introduce the attribute "total costs of the process chain" from the values *personnel*, *material*, and *production overhead costs* **(**Table 1**)**. As next their calculation will be briefly discussed in this section.

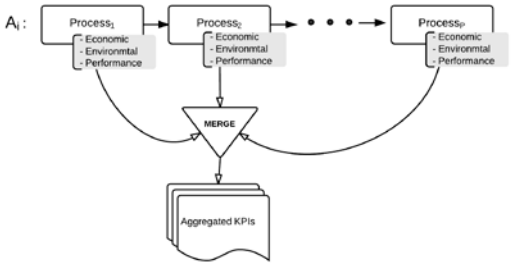



***Fig. 2*** *Illustration of the calculation for the three KPIs. Every sub-attribute is computed separately for every process before they get merged (accumulated) together to represent the sub-attributes which build up the hierarchical structure to represent the specific KPI for the whole process chain.*

At first, boundary conditions have to be made, because they are necessary for the calculation. They include the following factors: (i) number of work shifts, (ii) working hours per shift [h], (iii) working days per year [d], (iv) pay rate for personnel [€/h], (v) material costs [€/unit], and (vi) energy costs [€/kWh]

The **first indicator** and its sub-attributes are calculated through cost accounting like implemented in [3]. Important sub-attributes are *production overhead*, *personnel costs* and *material costs*, and the sum of all as value *process chain costs* **(**Table 1**).** All these values have the unit [€/component]. This has the advantage that the costs can be taken into causal consideration [3], this means that every cost attribute is calculated separately for every process in one process chain and are accumulated to form this KPI with its sub-attributes (Fig. 2). The values can be approximated or can come from accounting reports or other data sheets.

The **second indicator** represents information such as energy costs and environmental issues like the percentage of use of renewable energy sources. The values can be actually measured or can come from data sheets from machines or tools. In early stages of production planning only the energy consumption may be available so that for every process the energy costs could be calculated and then accumulated in the end for the whole process chain:

$$E = E_1 + E_2 + E_3 + \cdots + E_p. \tag{4}$$

Here $E_1$ formally represents the sub-attribute *energy costs* of the environmental objective (Table 1) for process$_1$ of the process chain $A_i$ (Fig. 2). In the end every sub-attribute is accumulated for one process chain to get an overall value for the alternative. This is done for *energy costs* in all three unit of measurements (days/month/year).

The performance is measured through the **third indicator**. It is subdivided into *production volume* and is covered in three units of measurements (Table 1). The production volume per day can come from first test series or can be approximated if the cycle time for every process is available. The production volume per day, month and year can also be calculated roughly with the global assumptions. For every process the sub-attributes are calculated separately and accumulated in the end to get a value for the whole alternative.

### *2.3 Prioritizing the KPIs by Weighting*

Weighting is an important and essential issue in this process because it reflects the preferences of a decision-maker and depends on different factors [6, 7]. For example production managers tend to rate technical and economic criterion and profitability higher than environmental issues like energy, fuel or gas consumption or the use of renewable energy sources, whereas operators of industrial robots might rate security at the working place and personnel loan higher than production volume. Through the different subjective perception of those authorities and operators the importance of those factors is different.

The preference (importance) of one attribute in comparison to another is modeled through weights. For each attribute $c_{.j}$ a weight $w_j$ is assigned independently from one alternative as described earlier in section 2.1. The weights are standardized to 0 at the most un-

important and to 1 at the most preferred. Assigning weights to attributes is a way to prioritize the criteria that are considered the most important for decision makers or stakeholders. Let $W_I$ the weight for the indicator $I$ than for every low level criterion a weight $w_j$ is assigned, so that they sum up to $W_I$:

$$\sum_{j \in L_I} w_j = W_I, \text{ with } 0 \leq W_I \leq 1, \sum_{I=1}^{M} W_I \leq \mathrm{M}. \quad (5)$$

The weights of all indicators can add up to 3 (see constraint in Eq. (5)) and each KPI must have a value in the interval [0,1]. The low level criteria $c_{\cdot j}, j \in L_I$ are dependent of the weight from their parent indicator $I$. The weights of each group of indicator $I$ add up to $W_I$. The assignment of the weights is independent from the alternatives, however; they relate to the attributes in general and not to a specific value.

### *2.4 Assessment*

To ensure that the calculated criteria are comparable the attribute matrix $\mathbf{C}$ is normalized between the interval [0,1] with the min-max-normalization rule [8]. Even if MCDM methods are suited dealing with large scales and the hybrid nature of attributes, works like [9] showed that normalization of all attributes may change the outcome and lead to a different assessment. If extreme values are present in the data set one attribute may get prioritized, but with scaling the assessment is not shifted towards possible outliers.

We use the value measurement approach to produce a preference order among all alternative (cf. [5, p. 85]). For that the utility (value) function $U(\cdot)$ is formulated and associated with an alternative in such a way that an alternative is represented as a value. If $A_i$ is preferred over $A_{i+1}$ then $U(A_i) > \mathrm{U}(A_{i+1})$, if both alternatives are indifferent then $U(A_i) = \mathrm{U}(A_{i+1})$. To calculate the utility (or use value) of an alternative $A_i$, **weighted additive aggregation** is used that takes the level hierarchy into account (cf. [5, 6, 9]):

$$U(A_i) = \sum_{I=1}^{M} W_I * \sum_{j \in L_I} w_j * c_{ij}. \quad (6)$$

Where:
$U -$ is the overall "score" (utility) for the alternative $A_i$,
$W_I -$ is the weight for the upper level criterion $I$ (the $I^{\text{th}}$ KPI),
$c_{ij} -$ is the normalized attribute $j$ for the alternative $A_i$,
$w_j -$ is the weight corresponding to the attribute $j$ in the attribute matrix $C$, and
$L_I -$ is the set of indices that represent all attributes for the indicator $I$.

We propose the new function $\hat{U}(\cdot)$ by using the basic utility function in Eq. (6) to turn the results in the positive direction, and extending the function with the parameter $\theta$:

$$\hat{U}(A_i, \theta) = 2 * \mathrm{s}\left(1 - \frac{U(A_i)}{\theta}\right)^{-1}, \text{ with } s(x) = (1 + \exp(-a\,(x-b)))^{-1}. \quad (7)$$

The function allows an optimal representation of the results. The use values will not be negative when evaluating the performance of the alternatives: The higher the value the better the alternative performs compared to the others. The factor $\theta$ represents the "strength of effect" or "uncertainty" of the result and is a positive value ($\theta > 0$). The new utility function in Eq. (7) has the following property

$$\lim_{\theta \to \infty} \hat{U}(A_i, \theta) = 1, \text{ if } a = b = 1. \quad (8)$$

The parameter can be varied to well-mark the difference of the evaluated alternatives. The higher the value $\theta$ the smaller the gaps between the results and the more difficult the decision will be. If $\theta$ becomes extremely large then all alternatives will not be discriminable, because the output will be one. The decision-maker can use this knowledge if there is a high uncertainty in the future. The value can be set smaller if more series of test are conducted and set higher if only rough approximations are available or the values are expectations. An optimization of the parameter is a research base in another paper based on the current available information and the progress of the production planning.

With Eq. (7) the final assessment is then conducted with the maximum rule

$$\max_{i=1,\ldots,n} \hat{U}(A_i, \theta), \quad (9)$$

which states that the alternative process chain $A_i$ with the highest utility value is chosen. It is important here to note that the alternative with the largest value will be selected as the "best" choice for the decision. That means that e.g. high production volumes will be favored as well as high production costs. If criteria like costs or energy consumption should be minimized it is necessary to mark those values in the attribute matrix $\mathbf{C}$ (see Eq. (1)) as negative ones (Table 1).[1]

## *3 Discussion*

To get insight of the effects of the model the following analyses were conducted and afterwards discussed. This helps the decision-maker to understand how the model behaves in a changed environment. For the example three random artificial alternatives are generated with the following relationships:

a) $(C_1 \geq C_2) \wedge (C_2 > C_3)$

b) $(E_1 \leq E_2) \wedge (E_2 \ll E_3)$

c) $(P_1 < P_2) \wedge (P_3 \leftrightarrow 2\,P_2)$

The expressions of the cost (C), energy (E) and performance (P) among the alternatives can be interpreted as follows: a) The costs of $A_1$ are greater or equal than $A_2$, but nearly the same, where $A_3$ has the lowest costs for the production; b) Both $A_1$ and $A_2$ have much lower energy consumption than $A_3$, but $A_1$ consumes less energy than $A_2$; c) $A_1$ has the lowest production volume and $A_3$ produces twice as much than $A_2$. The relationships are intentionally simplified for a easier understanding of the results of the model.

### *3.1 Uni-Criterion Analysis*

To begin the analysis of the model we ran a "uni-criterion" analysis to have an overview of the technical performance of each alternative for each criterion independently to measure the influence of the weights. This was done using Eq. (7), by steadily increasing the weight of the selected criterion $W_I (I = 1, .., M)$ by 0.1 beginning from 0 to 1 and settings the weights of all other KPIs to zero with $W_K$ $(K \neq I)$. That is done for all three KPIs separately to prioritize each indicator once. The results are presented in Fig. 3.

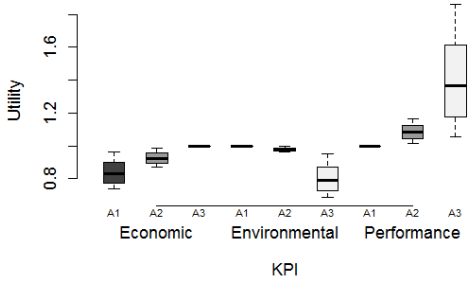



***Fig. 3*** *Representation of the variation of the outcomes if the importance of the KPIs is changing.*

If only the *economic objective* is considered then $A_3$ is always the best option. But an outlier from $A_1$ can be seen that performed nearly as well as the results around the median from $A_3$. That happened if low weights like 0.1 were used (that means no importance for that indicator). For the *environmental objective* one can say that $A_1$ and $A_2$ are the best options. Changing the weighting has no significant influence at the outcome for both (the variation in the data is small). Only for $A_3$ a high variation in the data can be seen. The

[1] Alternatively it is possible to use the *minimize* function in Eq. (9) instead so that only the attributes of the performance indicator has to be negative.

outliers from $A_3$ were created due to using a low weight like 0.1 which means that the KPI should be considered unimportant—through that fact a suboptimal alternative can perform as well as another in terms of a KPI if it is not considered important. If only the *performance indicator* is regarded then $A_3$ clearly is the best option between the other alternatives. Because $A_1$ and $A_2$ have the worst production volumes (see expression c) above) the weighting has not much influence on both. As explained before the same applies here: A low weight like 0.1 creates an outlier for $A_3$, which means that even the other two alternatives perform similar although $A_3$ has the highest production volume.

The results from the "uni-criterion" analysis were averaged for every alternative and depicted in Fig. 4.

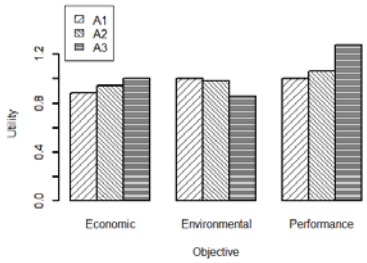



***Fig. 4*** *Average results in each group for every alternative if different weights are used in the "uni-criterion" analysis. Only one objective is considered at a time by setting the weights of the other objectives to zero.*

It can be seen that the model correctly interprets the relation between the three alternatives. Disadvantages from alternatives can be compensated through low weights and may also lead to false conclusions.

### *3.2 Considering the Strength of Effect*

In next analysis a variation of the factor $\theta$ was introduced and analyzed, where a neutral weight distribution of one was used for every KPI. Fig. 5 shows therefore a visual comparison of various values. In this case $\theta$ is set to $\theta = \{0.1, 0.5, 1, 4\}$. It can be seen that the higher the value the greater the differences between the three alternatives are. In early stages of production it is useful to set this factor greater or equal one. This can be used as a risk factor to avoid false decisions. In the case for $\theta = 0.1$ the results of the three alternatives are very wide apart (Fig. 5, left plot). The more precise data is available and the more progress in the manufacturing planning is made the lower this factor can be set to be more certain with the decision. For $\theta = 4$ the outcomes are nearly the same (Fig. 5, right plot). It is up to the authority to determine the best value and will be discussed in further research.

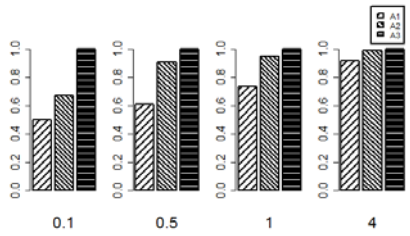



***Fig. 5*** *Variation of the factor* $\boldsymbol{\theta}$ *("strength of effect") to illustrate the influence on the decision.*

The evaluation of usefulness of an assessment depends on context and requires critical judgment of production manager and decision-makers. The assessment can only evaluate the current state of the environmental factors. Normally there is a high uncertainty in the future for factors like energy prices, new technologies, material or infrastructure, laws etc. that may heavily change the outcome.

## *4 Conclusions*

In this paper a prototype of a new decision-making model is proposed that can be used in the early stages of planning and production for new manufacturing chains. For the assessment three base KPIs with a hierarchical attribute structure were determined to represent an economic, environmental and a performance objective. A modified additive weighting aggregation approach from the classical value measurement theory was used in combination with additional factors that can be parameterized to change to outcome which is not common yet in literature.

It can be updated if new information are available and can then be compared to the previous assessments to evaluate the improvement. Furthermore the global boundaries can be changed to create "scenarios" like increasing production volume or energy prices. Maybe an alternative is favorable if the global boundaries are different.

Further work is dedicated to the integration of more environmental factors (e.g. carbon-footprint) and extending the performance objective by adding methods from data envelopment analysis (DEA). Additionally the goal is to provide simulation capabilities in the model and adding support for conducting multiple decisions at the same time and aggregating the results in an appropriate form. Decision-making under uncertainty will be further considered in the model as well. It is proposed to add an error term $\epsilon$ to the model, where $\epsilon$ reflects the uncertainty of the future assumed independently and normally distributed with $\epsilon \sim N(0, \sigma_\epsilon^2)$.

## *5 Acknowledgements*

This work was performed within the Federal Cluster of Excellence EXC 1075 "MERGE Technologies for Multifunctional Lightweight Structures" and supported by the German Research Foundation (DFG). Financial support is gratefully acknowledged.

## *6 References*

1. T. M. Pollock, "Weight Loss with Magnesium Alloys," *Science,* vol. 328, no. 5981, pp. 986-987, 2010.
2. Y. Zhang, P. Zhu and G. Chen, "Lightweight Design of Automotive Front Side Rail Based on Robust Optimisation," *Thin-Walled Structures,* vol. 45, no. 7–8, pp. 670-676, 2007.
3. "Energy-related and economic balancing and evaluation of technical systems – insights of the Cluster of Excellence eniPROD," 2013.
4. N. Weinert, S. Chiotellis and G. Seliger, "Methodology for planning and operating energy-efficient production systems," *CIRP Annals-Manufacturing Technology,* vol. 60, no. 1, pp. 41-44, 2011.
5. V. Belton and T. Stewart, Multiple Criteria Decision Analysis: An Integrated Approach, Springer US, 2002.
6. M. Weber and K. Borcherding, "Behavioral influences on weight judgments in multiattribute decision making," *European Journal of Operational Research* , vol. 67, no. 1, pp. 1-12, 1993.
7. J. Palma, A. Graves, P. Burgess, W. van der Werf and F. Herzog, "Integrating environmental and economic performance to assess modern silvoarable agroforestry in Europe," *Ecological Economics,* vol. 63, no. 4, pp. 759-767, 2007.
8. K. Priddy and P. Keller, Artificial Neural Networks: An Introduction, Society of Photo Optical, 2005.
9. K. Steele, Y. Carmel, J. Cross and C. Wilcox, "Uses and misuses of multicriteria decision analysis (MCDA) in environmental decision making," *Risk analysis,* vol. 29, no. 1, pp. 26-33, 2009.

# INVESTIGATION OF MECHANICAL PROPERTIES OF TITANIUM ALLOYS BASED ON GENETIC OPTIMIZATION AND PARETO FRONT

## ИЗСЛЕДВАНЕ НА МЕХАНИЧНИТЕ ХААКТЕРИСТИКИ НА ТИТАНОВИ СПЛАВИ НА БАЗАТА НА ГЕНЕТИЧНА ОПТИМИЗАЦИЯ И ФРОНТ НА ПАРЕТО

Martin Ivanov[1], Nikolay Tontchev[2]
New Bulgarian University, Sofia, Montivideo 21[1], University of Transport, Sofia, Geo Milev 158[2]

E-mail: mivanov@nbu.bg[1] tontchev@vtu.bg[2]

***Abstract:*** *An approach to the study of the relationship between the extreme values of the mechanical properties of titanium alloys . The approach is based on the approximated dependence of the mechanical properties of the chemical composition of the alloy of the ANN model . Approximating dependencies are included in the genetic optimization model based on optimization algorithm NSGA II, which was built by Pareto - fronts , modeling the relationship between the studied mechanical parameters.*

**Keywords**: METTALLURGICAL DESIGN, TENSILE PROPERTIES, COMPOSITION-PROCESSING-PROPERTY CORRELATION, APPROXIMATION WITH NEURAL NETWORKS, PARETO FRONT, NSGA II ALGORITHM

## *1. Introduction*

The process of material selection gives meaning to a whole trend in the material science at the design stage. It is directly related to information integration of engineering activities and to their effectiveness, being related to methods for automated information processing.

The choice of material and the technology for its processing are necessarily concerned to formalize the product presentation and also in order to improve engineering automation. The purpose of this work is subjected to to this idea. It is based on a priori data used in the creation of approaches and software tools for the determination of control parameters of the examined system simultaneously assessing several of its contradictory parameters.

This research is part of series of approaches and methodologies that at the stage of generating the decision do not use the knowledge gained in the field of metallurgy. The proposal has the potential to predict the mechanical properties of alloys, like in [1] [2], using prior information of data linking composition, processing and properties. The cited monograph explores the iron-based alloys, thus confirming the thesis for evaluation of these alloys numerically and experimentally. This methodology is the way to design alloys at a predetermined database.

Introducing the dependencies between the extreme values of the physico-mechanical properties of titanium alloys can hardly be achieved based entirely on empirical research and also on the relevant statistical treatment of the results. In most cases, the experimental research can be difficult, too lengthy and much too expensive.

This work proposes a solution based on the use of a software model and techniques from the field of multicriteria analysis and optimization, and establising regression relationships between the mechanical properties of the alloy and its chemical composition based on neural regression models.

At the base of the problematic links we find the set of non-dominated points with values of the investigated mechanical parameters - the so-called “Pareto front” and modeling relationships between the chemical composition and the mechanical properties with software tools. The task is presented as a typical multicriteria optimization problem. The main concepts in this task are described by the following relations:

General optimization problem - to be presented in the following form:

$$\max(f_1(x), f_2(x),..., f_m(x)), \quad (1)$$

where:

$f_1(x), f_2(x),\ldots,f_m(x)$ are the private optimization criteria (physical and mechanical characteristics);

$$x \in D \subset R^n, m \le 2, x = (x_1, x_2,..., x), \quad (2)$$

are the conditions defining the domain $D$ vector solution $x = (x_1, x_2, ..., x_n)$. In the specific task, the domain is given in the form:

$$D : x_k \in [l_k, h_k] \subset R, k = 1,..., n,, \quad (3)$$

where $l_k$ and $h_k$ are the lower and upper limits of the range of variation of each of the arguments (the percentage of the chemical element).

Relation of dominance between a pair of solutions $x^{(1)}$ and $x^{(2)}$ ( $x^{(1)} \prec x^{(2)}$ ) - expressed in the following form:

$$\forall i = 1,..., m \quad f_i(x^{(1)}) \ge f_i(x^{(2)}), \quad (4)$$

$$\exists j = 1,..., m \quad f_j(x^{(1)}) > f_j(x^{(2)}), \quad (5)$$

i.e. dominance of $x^{(1)}$ to $x^{(2)}$ is when at least one of the criteria is a strict inequality (indicating orientation) for both alternatives, the remaining criteria in force non-canonical inequality (or at less equality).

Pareto-optimal set – the set of solutions $P^* \subset D$, non-dominated by any element of the set $D$. The Pareto-front is a graphic representation of the Pareto-optimal solution in the target space.

## *2. Methodology for solving the problem.*

The definition of the purpose of the study leads to the formation of the general scheme of the model. The input parameters of the neural network are those of the alloy with composition and heat treatment according to Fig.1.

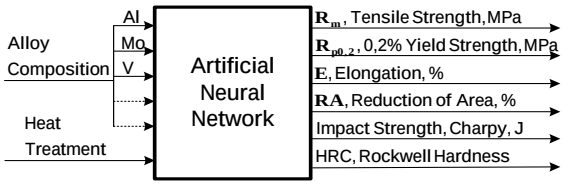



***Fig.1****. Input-output multicriteria research parameters.*

Neural network (NN) input parameters are the chemical composition and the types of heat treatment.

The composition includes the most often used alloying elements, namely Al, Mo, V, Sn, Zr, Cr, Fe and O.

The methodology for solving the problem is based on some verified and validated research capacity [1]. It includes two main components:

- Modeling the links between mechanical parameters via neural models [1], [2];
- Applying a genetic model for multi-criteria optimization and constructing the Pareto front [4].

The approach of combining these two concepts has proven to be effective . It allows to overcome some limitations related to the inability easy to obtain good approximations of the relations between the problem variables, and also with respect to the search for appropriate (or optimal) solution in the definition domain of the problem. Both applied paradigms combine modern means of finding the solution.

Modeling relationships between the problem variables is performed by approximation with neural networks of the "multilayer perceptron" type with a single hidden layer. For this purpose we used an established software tool - package Statistica v.10 of corporation StatSoft. The inputs to the network are the values of percentage of the following elements: Al, Mo, Sn, Zr, Cr, Fe, V, Si and O. Another nine inputs to the neural model are determined for the nine nominal levels (with values 0 and 1) of parameter *HT*. The output of the model is a single value for the approximated mechanical parameter $f_i(x)$. The number of neuron models corresponds to the number of the modeled relationships between the chemical composition and the mechanical properties. The complete description of the methodology for modeling and analysis of the results is subject to another presentation in a separate publication.

The formation of the Pareto front, even in cases with just two competing criteria, is not at all a simple problem. The aspects of this problem are:

- "Non-convex" front - in this case the construction of the front via the direct use of a series of points calculated on the basis of the decisions taken in the domain space of the problem is impossible. Such is the case with Pareto-fronts approximating the links in the investigated problem.
- Concentration of ("clustering") the calculated points from the front in several clusters with significant empty spaces between them. This is a common problem of genetic algorithms used to determine the Pareto-fronts.

To overcome these problems there was used the popular algorithm to construct Pareto-front based on genetic optimization NSGA II (a non-dominated sorted genetic algorithm), described in [4] and [5]. Characteristic of this algorithm is the inclusion of a specific advanced procedure for building a set of non-dominated solutions and taking under consideration the distance (the compression ratio) between the calculated points [4] up this front. The algorithm is well-researched and successfully applied to the solution of problems of this type. In order to use it in our case, we made in it some improvements:

- Reduce the minimum distance between the points forming the front (in order to achieve their even distribution along the line forming the front);
- Filtration of the solutions frequently occurring with the same value - also in order to cover the whole range of possible values in the front and to improve the performance of the genetic algorithm.

The introduced algorithm is implemented as software code in programming language Java.

## *3. Survey results.*

Data for constructing the studied relationships in the software model are taken from [3]. There have been approximated the values of parameters $Rp_{0.2}$, E and IS. Some of the research parameters manifest a significant scatter and low correlation between observed and modeled values, probably due to insufficient accuracy of the experimental results.

Despite the incompleteness of the data and their possible lack of precision there was achieved satisfactory approximation (the coefficient of correlation between observed and modeled values of $R$ is in the range from 0.79 up to 0.87).

Approximating dependencies (neural regression models) are included as source code in the basic software model that implements the algorithm NSGA II [4]. The results of modeling the Pareto fronts of the parameters Rp02, E and IS are shown in Fig. Fig. 1, 2, 3, 4 and 5. Fig. 6 shows a three-dimensional graph of the relationship between the parameters Rp02, E and IS. Unfortunately, due to the peculiarities of the algorithm at this stage, it was impossible to obtain a three-dimensional graph of the general Pareto-front for these three parameters.

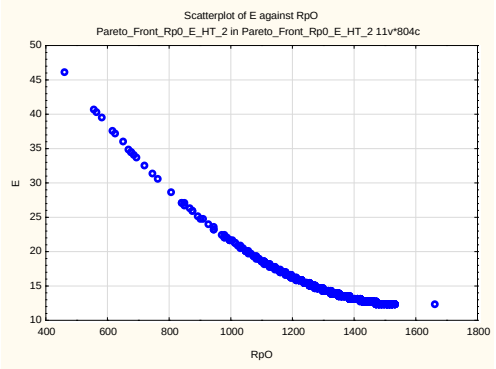



***Fig.2**. Pareto-front for parameters Rp02 and E for HT=2.*

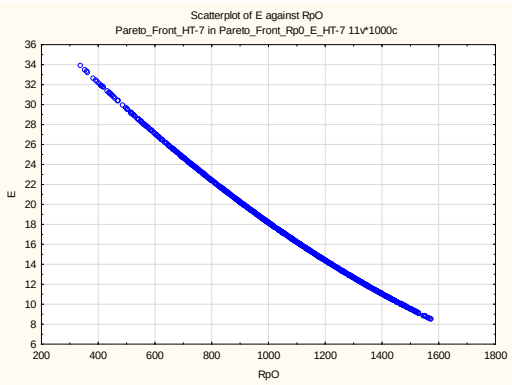



***Fig.3**. Pareto-front for parameters Rp02 and E for HT=7.*

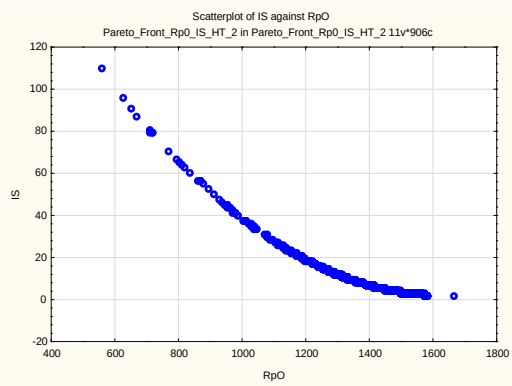



***Fig.4**. Pareto-front for parameters Rp02 and IS for HT=2.*

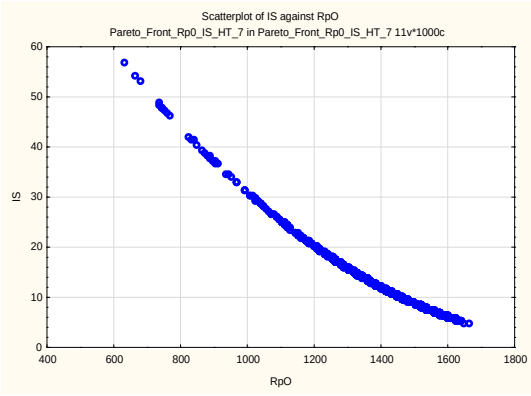



***Fig.5**. Pareto-front for parameters Rp02 and IS for HT=7.*

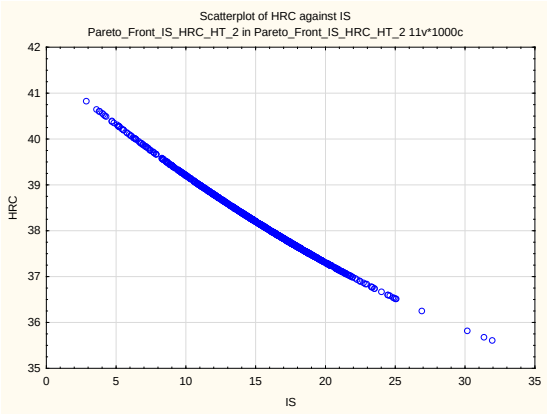



***Fig.6**. Pareto-front for parameters $Rp_{0.2}$, E and IS for HT=2.*

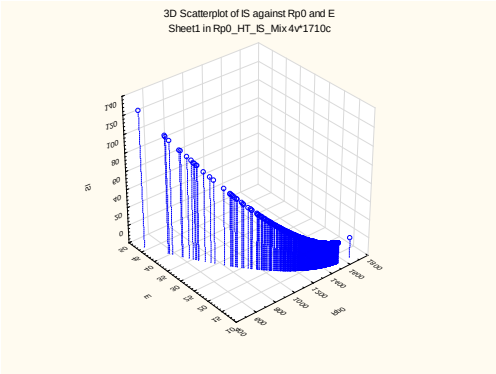



*Fig.7. Pareto-front for parameters Rp02, E and IS for HT=2.*

The achieved results show that the proposed method can quite successfully be used to determine the substantial relations between the extreme values of the mechanical parameters.

Complementation of the database from the experimental measurements from [3] will allow improvement of the software model and the future refinement of the results. The proposed approach and the established relations may be used in the engineering practice.

## *4. Conclusion.*

The new method offers a realistic possibility to significantly reduce the cost and time to predict chemical concentrations and multiple properties of a class of Ti alloys so that the new alloys will have improved properties.

For these specific properties there are indicated the possible combinations of alloying elements for different types of heat treatment. Regression and neural models are designed for the properties and optimization is performed for the composition and the processing parameters for a large database with more than 300 cases of different titanium alloys. Pareto front is constructed and analyzed related to the system 'composition-processing- properties .

## *References:.*


1. **Tontchev N., M. Ivanov**, Modeling and Optimization of the Composition of Iron – Based Alloys By Approximation with Neural Models and Genetic Optimization Algorithm, FBIM Transactions, 15 01, 2(1), pp. 1-12.
2. Tontchev N. Materials Science, Effective solutions and Technological variants, 2014/3/3, LAMBERT Academic Publishing
3. **Malinov, S, Sha, McKeown**, J.J.: Modelling and Correlation between Processing Parameters and Properties of Titanium Alloys using Artificial Neural Network. Computational Material Science 21, 375--394 (2001).
4. **Kalyanmoy Deb**, *Associate Member, IEEE*, Amrit Pratap, Sameer Agarwal, and T. Meyarivan , A Fast and Elitist Multiobjective Genetic Algorithm: NSGA-II, IEEE TRANSACTIONS ON EVOLUTIONARY COMPUTATION, VOL. 6, NO. 2, APRIL 2002.
5. **Sun Yijie, Shen Gongzhang** , Improved NSGA-II Multi-objective Genetic Algorithm Based on Hybridization-encouraged Mechanism, Chinese Journal of Aeronautics, Volume 21, Issue 6, December 2008, Pages 540–549.

# SOFWARE MODEL FOR SELECTION OF THE APPROPRIATE CHEMICAL COMPOSITION OF TITANIUM ALLOYS UNDER DEFINES REQUIREMENTS FOR MECHANICAL CHARACTERISTICS

## СОФТУЕРЕН МОДЕЛ ЗА ИЗБОР НА ЦЕЛЕСЪОБРАЗЕН ХИМИЧЕСКИ СЪСТАВ НА ТИТАНОВИ СПЛАВИ ПРИ ЗАДАДЕНИ ИЗИСКВАНИЯ КЪМ МЕХАНИЧНИТЕ ХАРАКТЕИСТИКИ

Martin Ivanov[1], Nikolay Tontchev[2]
New Bulgarian University, Sofia, Montivideo 21[1], University of Transport, Sofia, Geo Milev 158[2]
mivanov@nbu.bg[1] tontchev@vtu.bg[2]

***Abstract:*** *The paper presents the application of modern computational approaches in determining the appropriate chemical composition of titanium alloys . Discusses three types of problems for the selection of the chemical composition of alloy at set requirements for mechanical properties . Tasks are solved in a different formulation of the target criteria . The proposed solutions are based on software model using approximation with artificial neural networks and genetic optimization algorithm.*

**Keywords**: ….

## *1. Introduction*

The numeric design of the composition and the operative mode in metallurgy is a problem of particular complexity due to its multivariate nature. There is a need for continuous improvement of the whole industry in order to improve the properties of alloys with broad application.

Very small amounts of the concentration of alloying elements and their combinations may result in significant changes in the physical and mechanical properties of the alloys. This fact determines the need to seek the most appropriate for the specific concentrations of alloying elements. Probably the most famous center for research in the field of modeling and regression analysis of super-alloys is the one in the University of Cambridge UK [1].

Relying on extensive knowledge from companies, on various databases in the research of the relationships between them, it is possible to make valuable suggestions improving the parameters of the created products and technologies. That is why in science, probably the biggest asset comprises the rational ideas that jointly with the appropriate scientific infrastructure is implemented to specific technologies. The criteria evaluating various parameters of technology and products, as well as the methods for targeted search, refine initial ideas, and therein lies the essence of design with optimization.

This research is part of series of approaches and methodologies that at the stage of generating the decision do not use the knowledge gained in the field of metallurgy. The proposal has the potential to predict the mechanical properties of alloys, like in [2] [3], using prior information of data linking composition, processing and properties. The cited monograph explores the iron-based alloys, thus confirming the thesis for evaluation of these alloys numerically and experimentally. This methodology is the way to design alloys at a predetermined database.

The traditional alloy-development strategy consists of producing numerous samples with varying composition and set of the elements, the processing mode included, to { determine | define } an alloy with optimal properties [Campbell and Olson, 2001].

The approach resulted in high costs of experimentation [4].

This is the reason that the methods of directed search and the 'trial and error' method reside on, the highest level in the hierarchy of methods.

An alternative effective approach is to use data from past experience worked to a statistical model – based on a large amount of data associated by composition, processing and properties.

Compared to physical models, the advantage of statistical models lies in their ability to survey complex, multi-scale information in a timely and effective manner, even when well-established physic theories and models do not exist.

The results from the analysis of the models and the optimization can provide a guideline for further experimental and computational investigation [8].

The present paper aims at exploring and illustrating the possibility of using modern computational tools to solve specific engineering problems in the processing of titanium alloys.

The presented problem is formulated in the following way - determine an appropriate chemical composition of a titanium alloy from the elements Al, Mo, Sn, Zr, Cr, Fe, V, Si and O.

The percentage of elements in the alloy is represented by the arguments of the target function $X=(x_1, x_2,.., x_n)$. Three specific subproblems are formulated and examined with respect to the appropriateness of the decision of the most common problem:

- Define the requirements for the mechanical properties of titanium alloys as specific ("precise", "point") target values $g_i$ ($i$ = 1, ..., $m$);
- Define the requirements by the boundary (minimal or maximal) values (as unilateral restrictions);
- Define the requirements for the mechanical parameters in the closed interval (as bilateral restrictions on the parameters).

In the **first** case is solved an optimization problem of the form:

$$\min Z_1(X) = \sum_{i=1}^{m} (g_i - f_i(X))^2 , \quad (1)$$

where:

$q_i$ – is the target value of the i-th mechanical parameter: $i$ = 1, .., $m$;

$X = (x_1, x_2, ..., x_n)$ – is a vector of the decision (with the values of the arguments for the percentage of the elements in the alloy);

$f_i(X)$ – are links between the values of the arguments ($X = (x_1, x_2, ..., x_n)$) and the mechanical parameters of the alloy (obtained by approximation of the experimental data).

The problem domain is formulated by a set of bilateral restrictions:

$$D: x_i \in [l_i, h_i], i = 1,...,n , \quad (2)$$

where $l_i$ and $h_i$ ($i$ = 1, ..., $n$) are the lower and upper limits of the range, wherein is defined the $i$-th argument (the percentage of relevant chemical element).

The **second** problem is solved with the following formulation:

(3) $\min Z_2(X) = \sum_{i=1}^{m} w_i.\varphi_i(X)$,

where:

(4) $\varphi_i(X) = \begin{cases} 0, & f_i(X) \text{ comply with the requirements} \\ |g_i - f_i(X)| & \text{otherwise} \end{cases}$

$w_i$ – are assessments for violation of the requirements ("penalties"), which are determined separately for each of the mechanical parameters (criteria).

$f_i(X)$ - are approximations of the mechanical properties (as in problem (1)).

The problem domain is as above (2).

The third task is essentially a variant of the second, which limits the mechanical parameters are bilateral.

## 2. Methodology for solving the problem.

The considered tasks are based on research and results published in [1]. The methodology for solving problems is similar. It includes two basic approaches:

- Approximation of the relationships between the chemical composition of the alloy, and the mechanical characteristics based on neural models of the type of multi-layer perceptron (a method presented in [3]).
- Applying a genetic optimization algorithm ([6][7]) for determining an appropriate composition of the alloy - for each of the above-mentioned problems. The genetic algorithm is composed by the procedure described in [3].

The proposed methodology overcomes the difficulties with the usage of relations between the problematic parameters in an explicit analytical form and the classic optimization methods. The methodology is implemented in software code written in the language C, as an experimental software model (the scheme in Fig. 1).

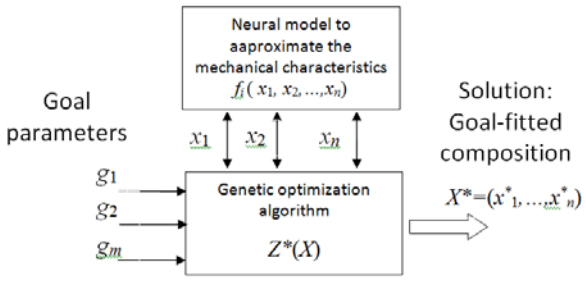



***Figure 1***. *Scheme of the software model.*

## 3. Experimental results.

Here are given some of the results obtained after series of experimental applications of the software model. The problems are applied to select the mechanical parameters $Rp_{0.2}$, E, IS and HRC, where the approximation relations give the most reliable results. Data for constructing the studied relationships in the software model are taken from [3].

Table 1 and Table 2 consistently present the mechanical parameters and the alloy composition according to Problem (1); Table 3 and Table 4 – the mechanical parameters and the alloy composition under requirements in the form of unilateral constraints; Table 5 and Table 6 – the mechanical parameters and the alloy obtained by imposing minimal and maximal constraints on the mechanical parameters.

The table shows the values of the target conditions (requirements) generated by the model values, the value of the goal function and the chemical composition of the alloy.

***Table 1.*** *Target values of physical and mechanical parameters Rp02, E, IS and HRC and results from the optimization of Problem (1).*

| Solution No | Initial requirements | Results | Deviation ( Goal function) |
|---|---|---|---|
| 1. | Rp0.2 = 950<br>E = 35<br>HT =2 | Rp02 = 9.49 85315417<br>E = 35.000895290 | 1.076700256161e-008 |
| 2. | Rp02 = 800<br>IS = 35<br>HT = 2 | Rp02 = 8.04.08046962<br>IS = 32.330481643 | 7.1137050227e-004 |
| 3. | HPC = 25<br>IS = 35<br>HT = 2 | HPC = 25.001246681<br>IS = 35.000952059 | 8.5996124444e-010 |

***Table 2.*** *Chemical composition of the alloy related to the decisions in Table 1.*

| Sol. No | Chemical composition [%] | | | | | | | | |
|---|---|---|---|---|---|---|---|---|---|
| | Al | Mn | Sn | Cr | Zr | Fe | V | Si | O |
| 1. | 0.12280648 | 1.40079958 | 5.51292458 | 3.1035798 | 4.093234 | 1.872463 | 7.493835 | 4.513992 | 2.0005951 |
| 2. | 0.02685628 | 8.51100192 | 0.06378368 | 0.0067140 | 1.099127 | 4.991254 | 1.406257 | 0.016751 | 0.24967650 |
| 3. | 0.68263801 | 9.66414380 | 8.45167394 | 3.3211157 | 2.652058 | 4.965371 | 0.145275 | 0.082504 | 0.2307855 |

***Table 3.*** *Target values of physical and mechanical parameters Rp02, E, IS and HRC, and results from the choice of Problem (2).*

| Solution No | Initial requirements | Results | Deviation ( Goal function) |
|---|---|---|---|
| 1. | Rp02 > 950<br>E > 35<br>HT = 2 | Rp02 = 1.2803199668e+003<br>E= 4.8938539044e+001<br>Ht=2 | 0.0 |
| 2. | Rp02 > 1050<br>IS > 35<br>HT = 2 | Rp02 = 1341.6185481e+003<br>IS = 33.139429441e+001<br>HT = 2 | 1.8605705586 |
| 3. | HRC > 40<br>IS > 35<br>HT = 2 | HRC = 43.428584903<br>IS = 35.831069211<br>HT = 2 | 0.0 |

***Table 4.*** *Chemical composition of the alloy related to the results in Table 3.*

| Sol. No | Chemical composition [%] | | | | | | | | |
|---|---|---|---|---|---|---|---|---|---|
| | Al | Mn | Sn | Cr | Zr | Fe | V | Si | O |
| 1. | 1.8936124 | 0.01556443 | 0.504898220 | 9.76595355 | 7.33109530 | 3.902914 | 0.105746 | 0.40852 | 0.112495 |
| 2. | 0.0236823 | 14.948728 | 0.018799401 | 0.0701623 | 10.979522 | 3.99333 | 3.81054 | 4.99223 | 0.248327 |
| 3. | 1.4412060 | 12.174138 | 5.046632282 | 3.5812860 | 9.5890377 | 4.81956 | 7.10196 | 0.44746 | 0.246832 |

***Table 5.*** *Target values of the physical and mechanical parameters Rp02, E, IS and HRC and results from the choice of setting bilateral requirements.*

| Solution No | Initial requirements | Results | Deviation ( Goal function) |
|---|---|---|---|
| 1. | Rp02 = [950,1200]<br>E = [35,40]<br>HT = 2 | Rp02 = 1.171.3229999<br>E = 36.359591800e+001<br>HT = 2 | 0.0 |
| 2. | Rp02 = [950,1200]<br>IS =[30,35]<br>HT = 2 | Rp02 = 1199.6942091<br>IS = 32.738526176 | 0.0 |
| 3. | HPC= [35,40]<br>IS = [25,30]<br>HT = 2 | HPC = 39.353021119<br>IS = 29.626693242 | 0.0 |

***Table 6.*** *Chemical composition of the alloy related to the decisions of Table 5.*

| Sol. No | Chemical composition [%] | | | | | | | | |
|---|---|---|---|---|---|---|---|---|---|
| | Al | Mn | Sn | Cr | Zr | Fe | V | Si | O |
| 1. | 6.30463576 | 10.0985747 | 0.21820734 | 7.7806024 | 1.1971194 | 1.563393 | 7.493820 | 0.345164 | 0.084156315 |
| 2. | 0.02002014 | 11.3794366 | 0.02014221 | 0.0647907 | 10.955353 | 4.957223 | 0.699942 | 0.321832 | 0.249633777 |
| 3. | 0.42066713 | 10.6305124 | 0.76204718 | 6.7080294 | 3.4221621 | 2.516608 | 11.68614 | 0.043824 | 0.208696241 |

## *4. Conclusion.*

This research is also an attempt to predict the concentrations of the majority of alloying elements, so as to create alloys with desired set of properties. This design concept was tested using experimental data. Thus it was shown that the approach has the potential to identify new compositions with significantly improved defined properties.

The new alloy-design concept uses a combination of a multicriteria algorithm and a stochastic optimization to predict mechanical properties of the explored alloys.

## *References:*


1. **Fujii, MacKay, D. J. C. and Bhadeshia, H. K. D. H**., "Bayesian neural Network Analysis of Fatigue Crack Growth Rate in Nickel-Base Superalloys", ISIJ International, Vol. 36, 1996, pp. 1373-1382.
2. **Tontchev N., M. Ivanov**, Modeling and Optimization of the Composition of Iron – Based Alloys By Approximation with Neural Models and Genetic Optimization Algorithm, FBIM Transactions, 15 01, 2(1), pp. 1-12.
3. **Tontchev N.** Materials Science, Effective solutions and Technological variants, 2014/3/3, LAMBERT Academic Publishing
4. **Vitos L., P.A. Korzhavyi and B. Johansson**, "Stainless steel optimization from quantum mechanical calculations", Nature Materials 2003, 2:25-28
"System design of high performance stainless steels I, Conceptual and computational design", Journal of Computer-Aided Materials Design 2001, 7:145-17
5. **Malinov, S, Sha, McKeown, J.J.:** Modelling and Correlation between Processing Parameters and Properties of Titanium Alloys using Artificial Neural Network. Computational Material Science 21, 375--394 (2001).
6. **Mitchell Melanie, An Introduction to Genetic Algorithms**, A Bradford Book The MIT Press, Fifth printing, 1999.
7. **David E. Goldberg**, Genetic Algorithms, Pearson Education, 2006.

# THERMAL STRESSES IN THE BLADES WITH AND WITHOUT TBC BASED ON THE TEMPERATURE DISTRIBUTIONS MEASURED USING THERMAL IMAGING CAMERA

M.Sc., Eng. Maś K.[1], M.Sc. Woźny M. [1], PhD. Eng. Dudek S. [2], PhD. Marchewka M. [1], PhD. Płoch D. [1], PhD. Bochnowski W. and Prof. Sheregii E. M. [1]

Center for Microelectronics & Nanotechnology – University of Rzeszow, Poland[1], WSK-PZL Rzeszow [2], Poland

kinga04@interia.pl, mwozny@ur.edu.pl,

***Abstract.*** *Turbine blades used in the jet engines are subjected to frequent and rapid temperature changes. As a result of the hot gases influence the temperatures excess 1000°C. Certain conditions for the blades generate local thermal stresses. In this paper the thermal stresses are calculated on base on experimental measurements of the temperature distributions using the high resolution thermal imaging camera FLIR SC7000 registered the distribution of temperature field for the blades with TBC and without TBC. The distribution of stresses in the blades based on the collected measurement data has been calculated. The calculations were made using FEM method implemented in COMSOL.*

**Keywords:** THERMOGRAPHIC MEASUREMENT, THERMAL STRESSES, FINITE ELEMENT METHOD, MECHANICAL STRESSES, BLADE MATERIALS, DESIDN.

## *1. Introduction*

The conditions within gas turbines are extreme: the pressure can be as high as 40 bar, the temperature more than 1000 K. Any component must therefore be carefully designed to be able to withstand thermal stresses, vibrations and loads asserted by the fluid rushing through the turbine. Therefore, it is very important to recognize the thermostresses arisen in blades due to the temperature gradients. Particularly, the distribution of real temperatures in-situ at work of engine is crucible. Usually, calculation of "internal stresses" or thermostresses in the turbine blades is based on modeling of the temperature distribution [1,2]. There are many works (see, for example, Refs. 3-10) where an analyses of thermostresses in the turbine blades was performed using the finite element method (FEM) assuming some theoretical distribution of temperature. From other hand, real distribution of temperature are playing an crucible role for estimation of the real thermostresses distribution in situ at work of engine.

In this paper is proposed the method of the real temperature distribution measurements. The measurements for the turbine blades with and without thermal barrier coatings (TBC) have been performed. Simultaneously, the calculations of the thermostresses distribution are provided for these blades using the COMSOL computer Program. The significant differences in this distribution for blades with and without TBC are demonstrated.

## *2. Description of the measurement method*

**2.1. Object of research.** The blades were made from the JETHETE M-152 high strength stainless steel which is a 12 % Cr, about 3 % Nickel, molibden, mangan, Silicon, carbon.



***Fig. 1*** *The turbine blades: left – without TBC, right – with TBC.*

The TBC were performed from ceramic material consisted $ZrO_2$ (zirconium oxide) mostly. The fig.1 show the blade without TBC on left and the blade with TBC on the right site.

**2.2. The temperature distribution measurements.** Measurement of the temperature distribution was made using the high resolution thermal imaging camera FLIR C7000. Temperature range of camera was set from 200°C to 1500°C. The frequency of measurement was 25Hz. In order to perform correct measurements of the temperature distribution on the surface researched there was made series settings to verify several parameters of the camera: emissivity of the object, apparent temperature– this parameters is important, when the measuring element is characterized by low emissivity; atmosphere permeability, distance between the objective of camera and the sample researched – this parameter is important because big part of radiation of the object is absorb in the air so the optimal distance was 1,35m.

The thermographic measurements were made for the blades heated in the chamber imitated the combustion chamber of the jet engine. In the chamber (dimensions: 240mm x 300mm x 140mm) were installed 2 gas burners powered by propane butane gas. This installation allows to record thermal excitation of blades as well as to observe differences in the cooling of the blades with TBC coating and without one. In order to provide the cooling conditions closer to real engine the air-flow with velocity of 20 m/s has been used for cooling of the blades. Controllable table (fig.1) with a rotor mechanism enable us to observe all surfaces of researched elements in reality time: the angle of rotation is changed from 0 ° to 360 °.

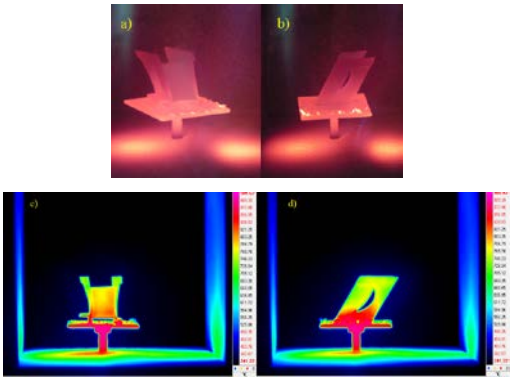



***Fig. 2*** *The Blades measured located in a specially designed heating position in the combustion chamber: a) and b) images was carry out in visible light, c) and d) in IR region using the thermography camera.*

In fig. 2 are shown the pictures of the blade located on rotating table. The pictures in fig. 2a and fig. 2b were obtained in visible light, whereas the pictures 2c and 2d – in the IR region using the FLIR SC7000 camera.

## *3. Experimental Results*

The results of thermographic measurements for two types of blades (with TBC and without TBC) are presented in figs. 3-6 as actual temperature distribution on their surface. In fig.3 is shown the actual temperature distribution on the blade surface for the case with maximal heating. This time point is chosed as initial: t=0.

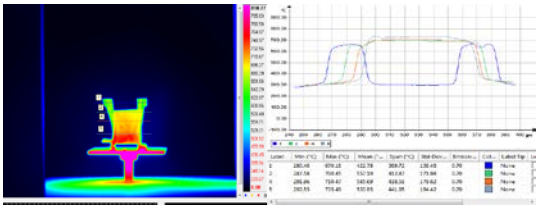


***Fig.3*** *The temperature distribution for blade without TBC obtained by thermographic measurements at maximal heating: initial point of time, t=0s.*

In next fig.4 is shown the temperature distribution on the same blade surface (shown in fig.3) after the 60 second cooling.

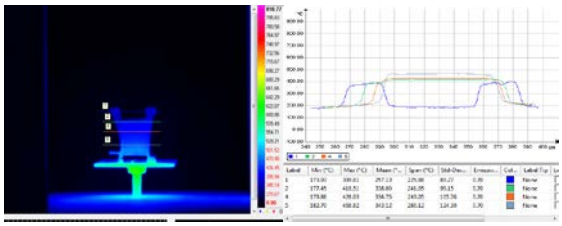


***Fig.4*** *The temperature distribution for blade without TBC obtained by thermographic measurements after the 60s time cooling: time point is t=60s.*

Such measurements of the surface temperature distribution were performed for each second during the180 s time cooling of blade. Analogical measurements were carried out for the blade with TBC barrier. The results are presented in fig. 5 and fig. 6.

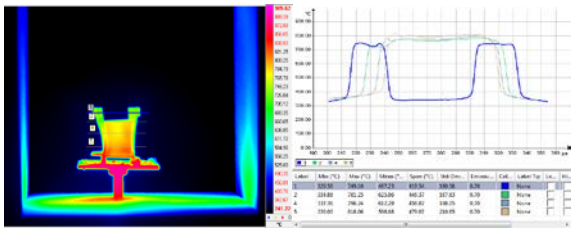


***Fig.5*** *The temperature distribution for blade with TBC obtained by thermographic measurements at maximal heating, initial time point, t=0 s.*

It is possible to notice that for last case of blade the maximal temperature $T_{max}$= 818°C, at t=0 was achieved whereas at the same process of heating only $T_{max}$= 735°C, at t=0 takes place for the case of blade without TBC

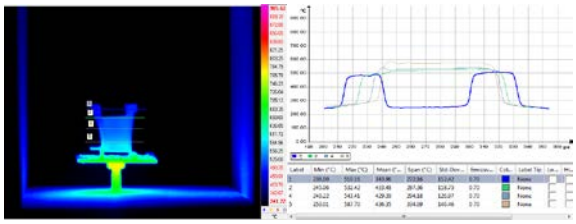


***Fig.6*** *The temperature distribution for blade with TBC obtained by thermographic measurements after the 60s time cooling: time point is t=60s.*

Despite of the same parameters and the same time of thermal excitation the temperature distribution for both case of blades is different: more high temperatures were achieved and process of cooling is more slow for the vane with the TBC coating.

## *4. Calculations*

The thermal stresses in the blades researched are calculated on base on experimental measurements of the temperature distributions presented above. COMSOL is a Computer Program Environment available for the thermostresses calculations [11]. For this aim were used two main library of COMSOL: the Structural Mechanics Module dedicated to the analyses in the 2D or 3D coordinate system and the Heat Transfer Module to investigate the effect of heating or cooling in the devices, components, or processes. That is module to study the mechanisms of the heat transfer – conduction, convection, and radiation – often in collaboration with other physics, such as structural mechanics. Program dispose of the Material Library with data for 2500 solid materials, such as Young's Modulus or heat and electrical conductivity, the temperature dependences of these parameters take place also. The M-152 alloy is available in the COMSOL Material Library. Among the data covered by the Material Library, there are the linear elastic model (requires a reference temperature that is set to 300 K) and the Poisson's Ratio that is set to 0.33, a number comparable to that for other stainless steels. The coating has been taken into account.

The calculations of termostresses are based on the motion equation as well as on the heat transfer equation using the FEM method [12]. The first step of the thermosteresses calculations was obtaining the voluminal temperature distribution on base of the experimentally measured surface temperature distributions. The example of such results is presented in fig. 7 where the inner temperature distributions are presented according three planes for the blade without TBC.

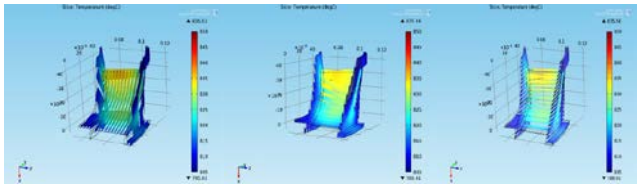


***Fig. 7*** *The inner temperature distributions obtained according three planes XY, YZ and XZ for blade without TBC.*

The temperature gradient distributions for blades researched is next step of calculations. In fig. 8a,b are presented such as distributions in the form of arrows the lengths of which is proportional to values of gradients. In fig. 8 are shown the points of maximal gradients which have achieved the values of above than 38000 K/m.

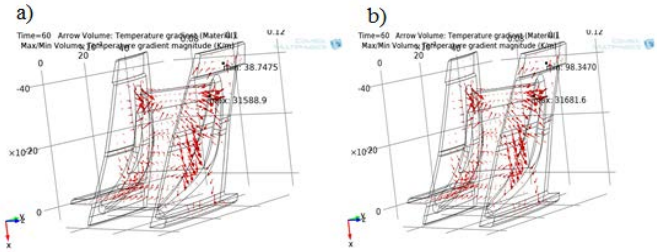



***Fig. 8*** *The temperature gradient distributions obtained for blades: a) without TBC; b) with TBC*

Third step is calculation of thermostresses and the results of these calculations are presented in Fig. 9a,b.

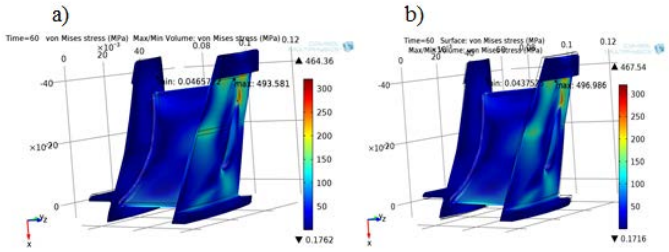



***Fig. 9*** *The thermostresses distributions obtained for blades: a) without TBC; b) with TBC*

In the fig. 9a as well as 9b are shown points with maximal value of stress. These values are 493.6 MPa for blade without TBC and 496.9 MPa for blade with TBC and these values are regarding to points where the maximal temperature gradients takes place. Whereas, the most volume of both blades is sized by low level of thermostresses, namely: below 100 MPa. At the same time this level is lower for blade with TBC.

## 5. *Discussion and Conclusions*

It is interesting to consider the temperature dependences of the thermostresses $\sigma_T(T)$ in different points of the blades. The curves of the $\sigma_T(T,x,y,z)$ are presented in fig.10 a, b. In inset of fig.10 are shown points on blade for which the $\sigma_T(T,x,y,z)$ curves were calculated.

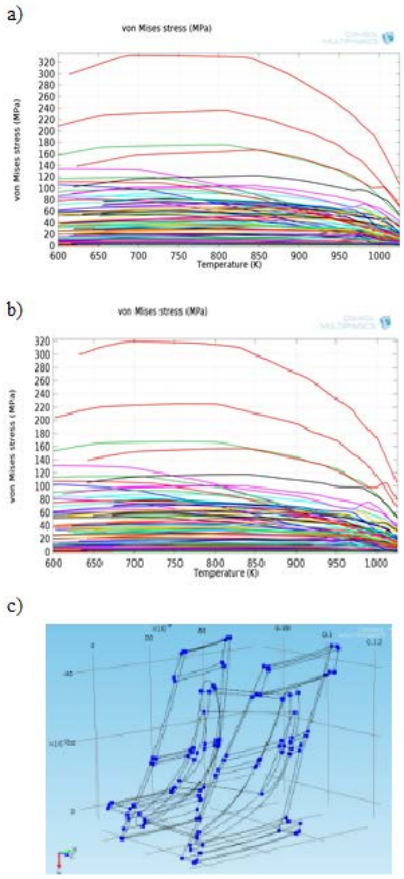



***Fig.10*** *The curves of thermostresses $\sigma_T(T,x,y,z)$ for different points of the blades: a) blade without TBC; b) blade with TBC; c) are shown the points for which are calculated the $\sigma_T(T,x,y,z)$ curves.*

The $\sigma_T(T,x,y,z)$ – curves are calculated for case of cooling of blades from temperature of maximal heating: to $T_{max}$= 818°C or 1091K. It is possible to see that maximal values of stresses are achieved at temperatures between 700K and 800 K. The $\sigma_T(T,x,y,z)$ – curves for blade with and without TBC covering are similar, particularly, in case of points with maximal stresses. Some differences take place for points where thermostresses are lower: the character of dependences is similar but level of stresses is lower for blade with TBC covering. The largest differences take place for the curves of total displacements.

The curves of displacements $\delta l(T,x,y,z)$ for different points on the vane surface are of great interest because that are values of real deformations in blades while the total displacement don't means the linear extension (thermal dilatation) but length of trace for individual points at deformation. In fig.11 are presented the $\delta l(T,x,y,z)$ - curves for blade with and without TBC-covering. The total displacements for the blades with and without TBC are different: in the case of blade with TBC the total displacements are smaller. The character of the $\delta l(T,x,y,z)$ dependences it seems to be similar but really in case of the blade without TBC-covering the region where the displacements are changing is twice as big what show a non-homogeneous tendency for displacements of significantly more large values for different points.

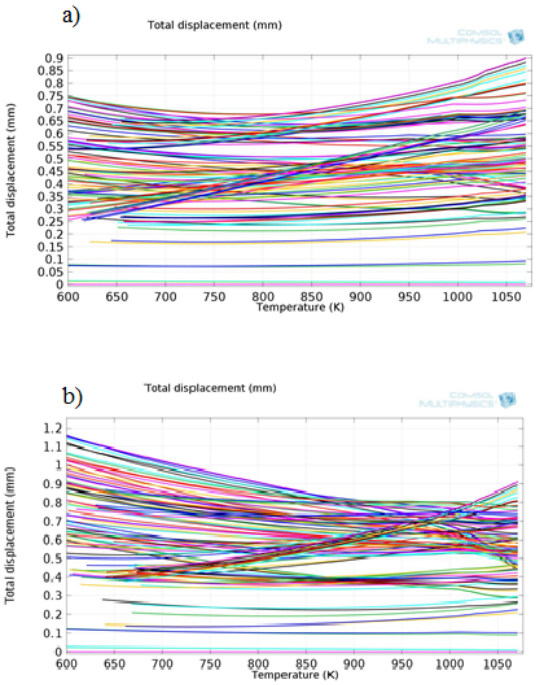



***Fig.11*** *Total displacements of chosen points in blades after cooling during 60s: a) for blade without TBC; b) for blade with TBC*

Therefore, the thermal stresses aroused in the turbine blades are calculated on base on experimental measurements of the temperature distributions using the thermographic high resolution camera FLIR SC7000. The measurements were performed at heating of the blade in special chamber imitated the combustion chamber of the jet engine. That one and careful calibration of thermographic camera enable us to obtain the real distribution of temperature for different surfaces of blades. The measurements were performed for blade with thermal barriers coatings (TBC) and for blade without TBC. Numerical calculations were carried out on the base on these experimental data using Program COMSOL what enable us to state differences in the deformations in the blade with TBC in comparison with the blade without TBC. Whereas, the blade without TBC show a non-homogeneous tendency for displacements of significantly more large values for different points of the blade, on the other hand, the absolute values of thermostresses are similar.

## *References*


[1] M.P. Boyce, *Gas Turbine Engineering Handbook*, Gulf Professional Publishing, Second edition, 2001.

[2] J. Bredberg, *Turbulence Modelling for Internal Cooling of Gas-Turbine Blades*, Thesis for the degree of doctor of philosophy, Chalmers University of Technology, 2002.

[3]Poursaeidi E., Mochammadi M., Khamesi S.S., Advanced Materials Research 452-453 (2012)pp.502-507.

[4]Khor K.A. , Gu Y.W., Materials Science and Engineering A277 (2000) p. 64–76.

[5]Lugscheider E., Nickel R., Surface and Coatings Technology 174 –175 (2003) p. 475–481.

[6]Ng H.W., Gan Z., Finite Elements in Analysis and Design 41 (2005) p. 1235–1254.

[7]Pandaa P.K., Kannana T.S., Duboisb J., Olagnonb C., Fantozzib G., Journal of the European Ceramic Society 22 (2002) p. 2187–2196.

[8]Park J.-W., Mendez P.F., Eagar T.W., ActaMaterialia50 (2002) p. 883–899.

[9] Sfar K., Aktaa J., Munz D., Materials Science and Engineering A333 (2002) p. 351–360.

[10]Teixeira V., Andritschky M., Fischer W., Buchkremer H.P., Stöver D., Journal of Materials Processing Technology 92-93 (1999) 209-216.

[11] *ComsolMultiphysics 3.4 User's Guide, Modeling Guide and Model Library,Documentation Set*, Comsol AB, 2007.

[12*]Thermal Stress Analysis of a Turbine Stator Blade*, Solved with COMSOL Multiphysics 4.3, Comsol , 2012

# APPLICATION OF EA SIGNAL TO EVALUATE THE DEGRADATION OF X6CrNiTi18-10 STEEL DURING TENSILE TEST

Dr Bochnowski W.[1], Dr Dziedzic A.[1], Dr Adamiak S.[1], Prof. Szeregij E.[2]
Faculty of Mathematics and Natural Sciences – University of Rzeszow, Poland [1]
Center for Microelectronics & Nanotechnology – University of Rzeszow, Poland[2]

wobochno@ur.edu.pl, dziedzic@ur.edu.pl, sadamiak@ur.edu.pl,

***Abstract: The EA Signal tests*** *registered during the static stretching of the X6CrNiTi18-10 steel (according to EN 10088)* ***have been*** *included in the work. The tests were done in the room temperature and in the high temperature of - 400°C on the universal strength (tensile) machine ZDM-5 with the range of 0-50 kN equipped with the digital registration of the strength and stretching. The analysis of the EA signal intensity has been conducted, depending on the deformation of the sample and test temperature. On the basis of the EA signal there have been the own characteristic oscillation frequencies of the samples designated, being the effect of the degradation of the structure as a result of the increased load.*

**Keywords**: ACOUSTIC EMISSION, STRENGTH TO STRETCHING, STAINLESS STEEL

## *1. Introduction*

The EA method allows to register the signal in real time, generated as a result of the rising stresses caused by the outer mechanical load or/and thermal [1,2]. The behaviour of cracks– their initiation and development under operation of mechanical (tensile stresses, compressional stresses, oscillating, constant and variable) and thermal outer loads can be quantitatively described through the EA signal parameters (duration time,count numbers, energy and signal amplitude).

Presenting the relationships between the internal stress caused by the outer load, crack mechanisms and qualitative and quantitative indicators describing signal of acoustic emission, is the subject of many publications [3-7]. The widely used FFT analysis for the description of the EA signal. Due to the character of the EA signal (huge changes of the amplitudes within short time and lack of periodicity) the wavelet analysis has been used more often.

There are tests undertaken in order to define the characteristic signal frequencies generated during the spring strain and plastic strain for materials used in TBC coatings [2,3].

The key problem of the qualitative evaluation of the EA signal is the selection of the measurement signal processing method. The commonly used Fourier transformation practice and also wavelet transform which is applied more often, allow for receiving the qualitative description of the frequency spectrum of the EA signal, directly dependent on the types of the cracks, their size and arrangement. In specific conditions that is high and low thermal loads, the qualitative evaluation of the process of creation, connecting and penetration of cracks will allow for defining the life span of the layer in a specific conditions of the thermal load on the basis of the chosen EA signal parameters [2].

The authors of that work [3] performing the test in the room temperature, determined the characteristic EA signal frequencies generated as a result of the cracks of the marked layer. The specific types of cracks have been correlated ( crosswise, longitudinal and layer delamination) with the corresponding signal frequences for the used TBC layers.

## *2. Material and test methodology*

The samples of austenitic steel X6CrNiTi18-10 (according to EN 10088) were used to the static test of stretching in the temperature of 20°C and 400°C, in the annealing state, made of metal sheet of the thickness - 4 mm and other sizes as in the fig. 1. The requirements of the binding standard PN EN ISO 6892-1 have been considered while matching the sizes. Tensile test part 1.

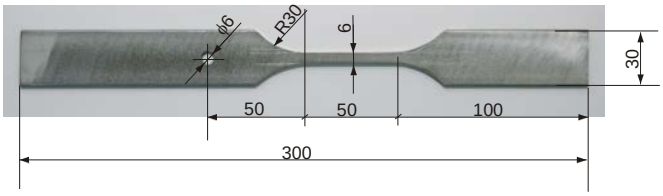



***Fig. 1*** *Shape and size of the flat samples used in the static tensile test*

The measurement path of the EA signal was tested during the static tensile test in the room temperature.The static tensile test was done at the universal strength machine ZDM-5 of the 0-50 kN range equipped with the digital registration and strength record and extension (fig. 2).

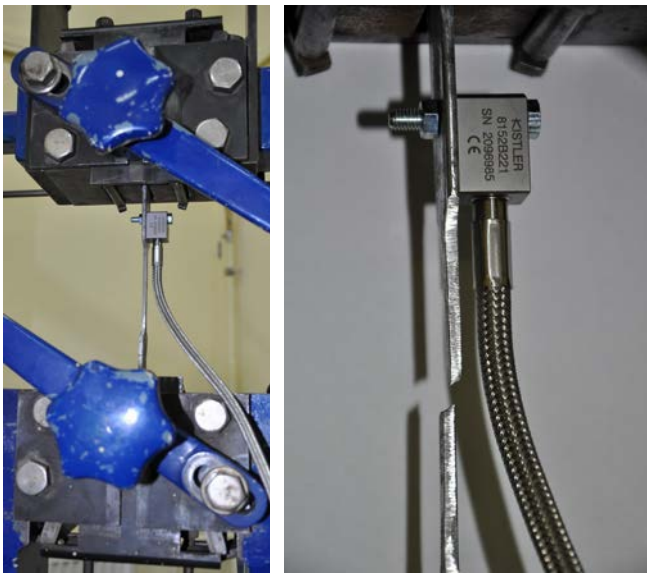



***Fig. 2*** *A test with the EA sensor in the strength machine handles before and after breaking*

The EA signal has been registered with the use of the EA Kistler 8152B sensor. It ensured receiving the needed sensitivity and resonance characteristics. The signal from the EA sensor was connected to the standard signal conditioner- Piezotron Coupler-that included the preamplifier, amplifier and lower and upper bushing filters. The reinforced and filtered initial signals that were sent to the 12-bit measuring card RT-DAC4/PCI of the test frequency up to 0,5 MS/s/ch.

In order to register the signal sent from the card to the computer, the application had been made in the Microsoft Visual C++ 2010 language. The application had the possibility of the assumption of: test frequency, reinforcement coefficients and formats of the output data record of the measured EA signal. The

data was developed in a numerical form to the file *.txt in two columns: time (s) and level of tension. The Fourier FFT transformation was done with the use of the applications in the Matlab/SIMULINK environments.

In case of using the National Instruments card, the application has been prepared in the LabVIEW system, which allows for the stream measurement data record of the EA signal for the test frequencies 140 kS/s within 240s time. The application diagram has been presented in the fig. 3. The Advanced Signal Procesing Toolkit package tools and FFT transform have been used to the analysis of the EA signal.

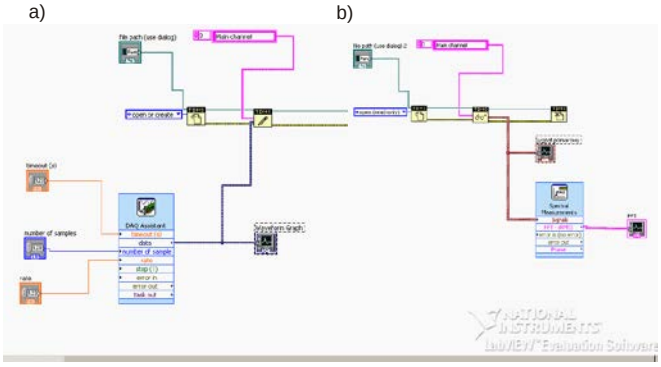



***Fig. 3*** *Application diagram - LabVIEW: a) used in measurements , b) used in the EA signal analysis.*

Before measurements, the EA sensor has been checked with the Nielsen and Hsu method, meeting the ASTM standards- ASTM E976-84. The sensor has been screwed to the steel plate of the size - 250x250x30 covering the contact element of the sensor with the silicone grease. At a distance of 50 mm from the sensor, the graphite lead refill -2H hard, 0,5mm diameter, slipped off of 3 mm, The support case has been put on the lead refill, that ensured the proper inclination angle. The collected signal was the effect of spring strain of the steel plate due to the graphite lead refill breaking – the tension value in the time function was given to the FFT transform, and the frequency spectrum of the measured signal was received.The test was done 5 times. The example of the result received in the first, second and third test was presented in the fig. 4.

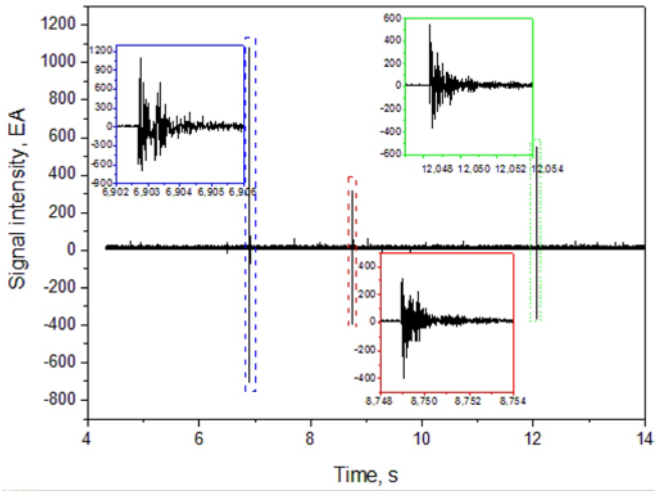



***Fig. 4*** *The example of the EA signal course together with the enlargement of the chosen fragments.*

## *3. Test results*

During the test, time, extension, strength, AE signal was registered. On the basis of the collected data, the graph of nominal tensile in the extension function and the corresponding course of the EA signal level change have been presented for each of the five tested samples.

The source of the acoustic emission signal in a matter are among others, the processes of defects relocations such as the dislocation movement, microcrack propagation that can lead to the permanent shape change and size of the object. The amplitude and the impulse energy change within the huge range because they can come from relocation of single dislocations, and also from the propagation of the cracks in a material. The example of the change course of the level of the EA signal registered together with the enlargement of the chosen fragments have been presented in the fig. 5.

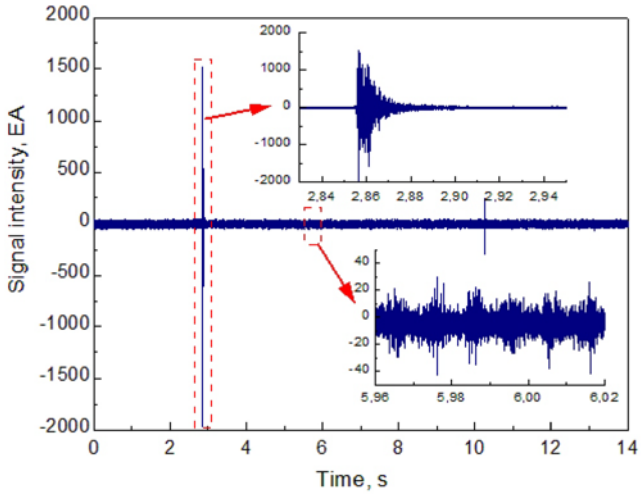



***Fig. 5*** *The example of the EA signal together with the enlargement of the chosen fragments*

As a result of the plastic strain of the tested steel, the characteristic EA signal spectrum has been received during the static tension test that can be the result of rising of the crystal network defects such as dislocations,Cottrell's atmosphere,Lüders' line. There has been the considerable increase of the event counts generating EA signal on the tested samples during stretching in the temperature of 20$^{o}$C after crossing the symbolic border of plasticity (fig. 6, B area). During the further plastic strain, at the time of stretching, the number of events generating EA signal has been decreasing (fig. 6, C area). After crossing the maximum strength during the narrowing, another increase of the EA signal level change has been registered in the sample. The differences in the EA signal quality has been also noted down during the tests of stretching conducted in the high temperatures. During the sample stretching in the temperatures of 400$^{o}$C and 650$^{o}$C the lower number of events generating the change of the EA signal amplitude have been registered (fig. 7).

On the basis of the EA signal, the characteristic frequencies of the sample own oscillations have been designated, being the effect of the structure degradation as a result of the increased load that was presented in the table 1.

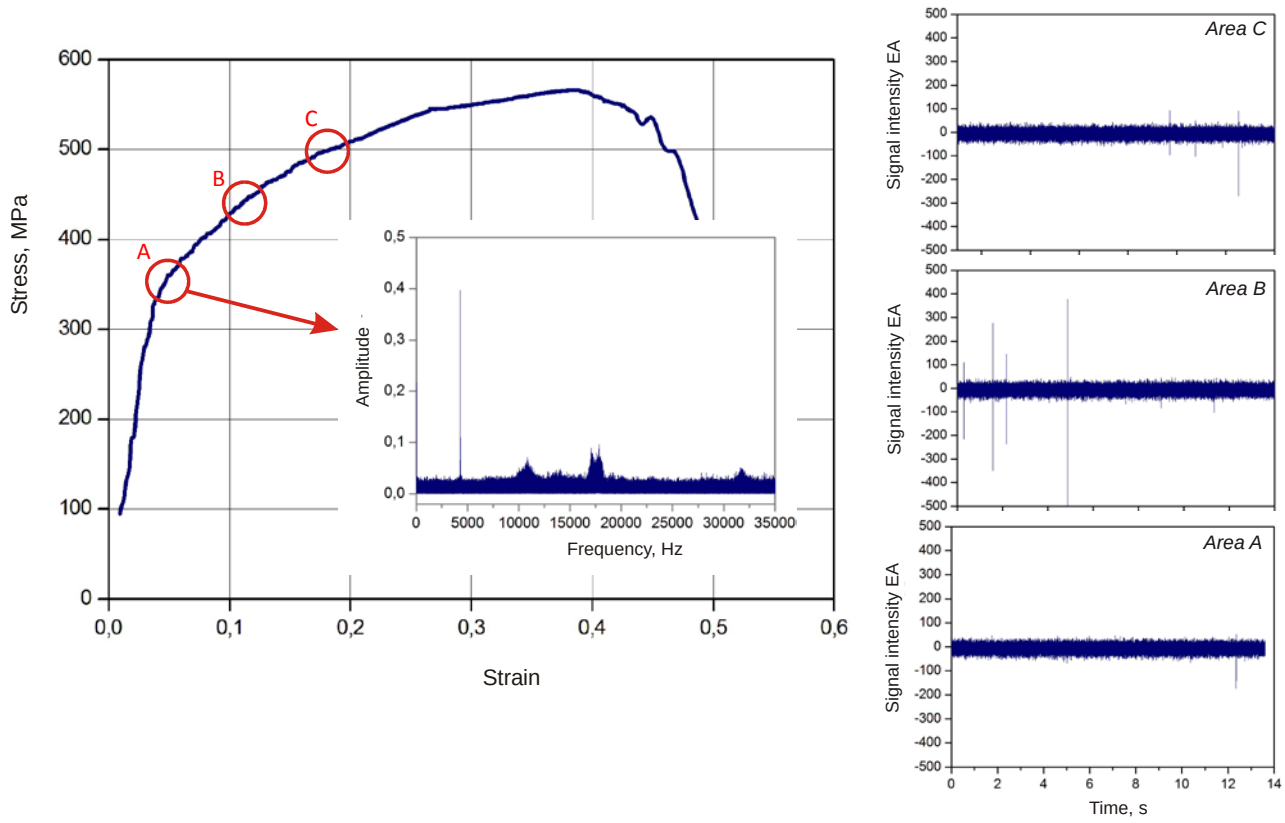



***Fig. 6*** *Curve-tensile steel strain X6CrNiTi18-10 received.in the temperature of 20°C and graphs of EA signal registered in the A,B,C areas together with the example FFT graph.*

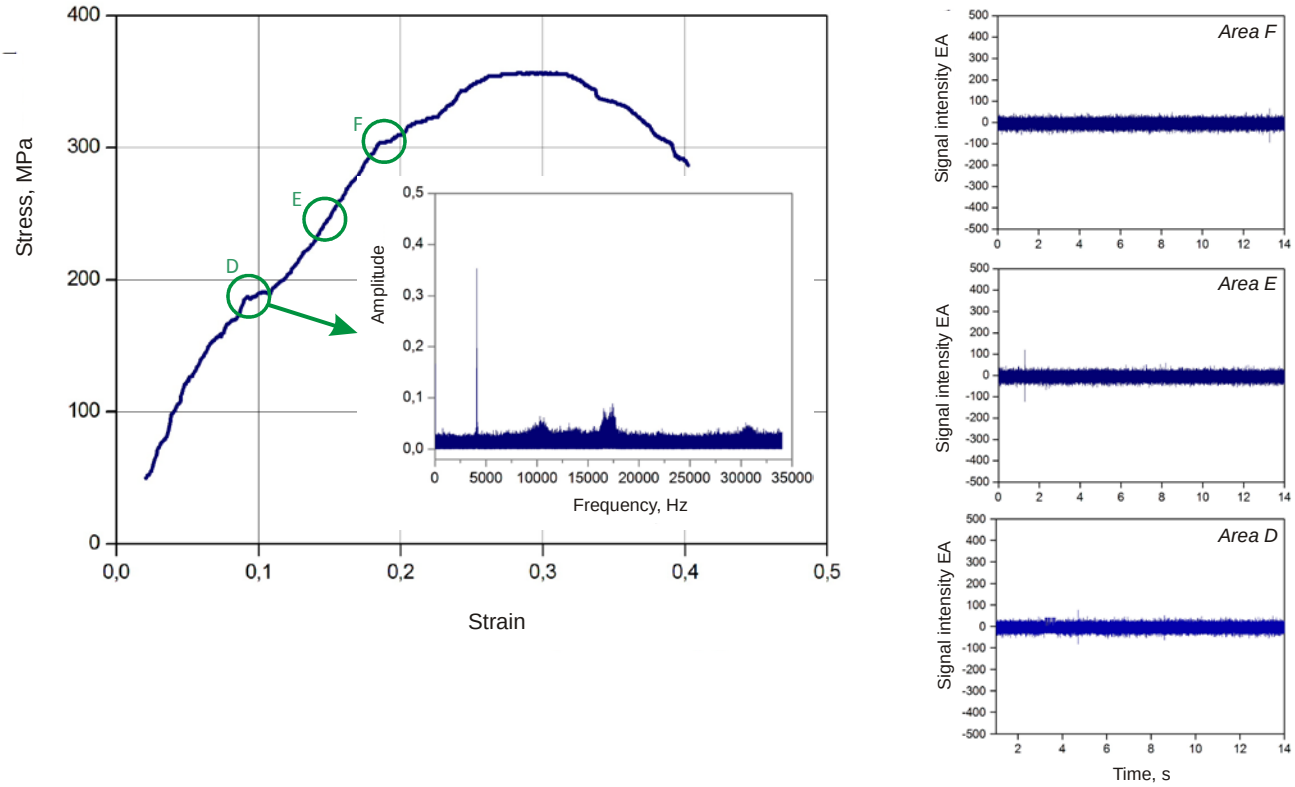



***Fig. 7*** *Curve tensile steel strain X6CrNiTi18-10 received in the temperature of 400°C and EA signal graphs registered in the D, E, F areas together with the example FFT graph .*

***Table 1: Typical frequencies of the signal generated during the static tensile test*** *of the steel X6CrNiTi18-10 conducted in the temperature of 20°C and 400°C.*

| Test temperature $^0$C | Typical frequencies designated from the tested areas | | | | | |
|---|---|---|---|---|---|---|
| | area | Hz | area | Hz | area | Hz |
| 20 | A | 4286;<br>10823;<br>17076;<br>17882;<br>31772 | B | 4280;<br>10607;<br>17165;<br>17910;<br>31685 | C | 4275;<br>10689;<br>17221;<br>17800;<br>31660 |
| 400 | D | 4087;<br>10442;<br>16561;<br>17455;<br>30674 | E | 4087;<br>10403;<br>16605;<br>17367;<br>30652 | F | 4209;<br>10655;<br>17157;<br>17842;<br>31512 |

## *4. Conlcusions*

The Fourier's FFT analysis of the EA signal in case of the measured signals, especially short-time aplitude change turns the result loaded with the certain imperfections.

New possibilities within the field of frequency-time analysis are given by the wavelet analysis. The designated coefficients of constant wavelet transform can be presented in the form of time-scale signal graph. It is a different image of the signal data than the time-frequency Fourier's image.

An important thing in the wavelet transform is the proper selection of the filter bank. It guarantees the getting out information essential for the identification. It depends on the type of the information processed and is the individual matter for each case. The wavelet choice is done experimentally.

It is planned to conduct FFT analysis and the wavelet analysis of the EA signal received within the range of the plastic strain in the static tensile test in another research.

**Gratitudes to:**

Financial support of Structural Funds in the Operational Programme - Innovative Economy (IE OP) financed from the European Regional Development Fund - Project "Modern material technologies in aerospace industry", Nr POIG.01.01.02-00-015/08-00 is gratefully acknowledged.

## *5. References*

1. L. Yang, Y.C. Zhou, C. Luc: Damage evolution and rupture time prediction in thermal barrier coatings subjected to cyclic heating and cooling: An acoustic emission method, Acta Materialia 59 (2011) 6519–6529.
2. X.Q. Ma, S. Cho, M. Takemoto: Acoustic emission source analysis of plasma sprayed thermal, barrier coatings during four-point bend tests Surface and Coatings Technology 139 2001.
3. W.B. Yao, C.Y. Dai, W.G. Mao, C. Lu, L. Yang, Y.C. Zhou, Acoustic emission analysis on tensile failure of air plasma-sprayed thermal barrier coatings, Surface & Coatings Technology 206 (2012) 3803–3807.
4. C.K. Mukhopadhyay, K.K. Ray, T. Jayakumar, Baldev Raj, Acoustic emission from tensile deformation of unnotched and notched specimens of AISI type 304 stainless steels, Materials Science and Engineering A255 (1998) 98–106.
5. V. Satheeshkumar, P.R. Lakshminarayanan, Developing mathematical models on tensile strength and acoustic emission count of ZE41A cast magnesium alloy, Journal of Alloys and Compounds, S0925-8388(12)00699-8, 2012.
6. F. Dahmene, A. Laksimi, S. Hariri, C. Hervé, L. Jaubert, M. Cherfaoui, A. Mouftiez, Acoustic wave propagation in austenitic stainless steel AISI 304L: Application examples,International Journal of Pressure Vessels and Piping 92 (2012) 77-83.
7. Zhiyuan Han, Hongyun Luo, Hongwei Wang; Effects of strain rate and notch on acoustic emission during the tensile deformation of a discontinuous yielding material, Materials Science and Engineering A 528 (2011) 4372–4380.

# PVD DEPOSITION OF HAFNIUM IN ALUMINIDE COATINGS

Jolanta Romanowska
Rzeszów University of Technology, Department of Materials Science W. Pola 2 str., 35-959 Rzeszów, Poland

E-mail: *jroman@prz.edu.pl

***Abstract:*** *The paper presents comparison of microstructures of hafnium modified aluminide coatings deposited in two different ways on pure nickel. In the first way a hafnium layer was deposited by the EB-PVD method, subjected to the diffusion treatment for 6 hours and than aluminum was deposited by the CVD method. In the second method, double layers of hafnium (3 μm thick) and aluminum (3 μm thick) were deposited by the EB-PVD method on the nickel substrate. The double layers were subjected to diffusion treatment at 1050 $^0$C for 6 h. The obtained coatings were examined by the use of an optical microscope (microstructure and coating thickness) and a scanning electron microscope (chemical composition on the cross-section of the modified aluminide coating). In aluminide coatings deposited by the CVD process, an outward nickel diffusion via the hafnium layer and inward aluminum diffusion to the surface of nickel lead to the formation of a diffusion zone. Hafnium forms a layer of intermatallic phases with nickel in the diffusion zone. Diffusion treatment for 6 h of nickel with hafnium and aluminum layer leads to formation of the $Ni_5Hf$ phase.*

**Keywords**: PVD METHOD, CVD METHOD, ALUMINIDE COATINGS, HAFNIUM

## *1. Introduction*

Protective aluminide coatings deposited on superalloys are degraded by the loss of Al due to oxidation of the coating surface to form aluminum oxide and by interdiffusion with the underlying substrate [1]. It accelerates the rate of the oxide growth and results in the loss of the coating strength and deformation of the coating. Therefore, as to improve the oxidation resistance of the coating it is necessary to slow oxide scale growth and improve its adherence [2-5]. Aluminum concentration gradient between the superalloy and the coating is the driving force of the Al loss. Candidate diffusion barrier materials should retard Al diffusion at high temperatures, possess good thermo-mechanical compatibility with the substrate and the coating and remain relatively stable for extended periods of time at high temperature. The addition of small amount of reactive elements such as: hafnium, zirconium, yttrium and cerium has a beneficial effect on oxidation behavior since [6-7]. This beneficial effect includes an improvement of adhesion of alumina scales and reduction of oxide scale growth rate. Pint et al. [8,7] allege that hafnium doped cast alloys proved that hafnium doping of β-NiAl and Ni-Pt aluminides reduces the parabolic rate constant by a factor of ten and even possibly to be more efficient than platinum addition. Hafnium addition to the nickel superalloy decreases the propensity for rumpling oxides when it diffuses into coating and to the growing aluminum oxide [9, 7].

Hafnium is a reactive metal with melting temperature of 2225 °C. Hafnium has extremely high chemical reactivity with various materials: oxygen, nitrogen, hydrogen and carbon [7, 10]. Cochardt et al [11, 7] showed, that small content of hafnium (0.1 -1.0 % wt) improves high temperature mechanical properties.

Due to the significant beneficial effects of hafnium addition on the oxidation resistance of nickel based superalloys, processes of diffusion coating were intensively investigated. Howment research corporation [12-13] incorporates hafnium into platinum aluminide coatings by CVD method. Addition of small amount of hafnium (<1 wt %) to the coating and controling its level and distribution in aluminide coatings remains an open issue [14].

Nesbitt et al. and Warnes et al. suggest that NiAl – based alloys containing small amount of reactive elements (hafnium or zirconium) added with or in place of platinum exhibit further improvements of the lifetime [15-16]. The reactive elements addition to these alloys causes an improvement of the alumina scale adhesion and a reduction of the growth rate of the scale by the segregation of reactive elements' ions on the scale grain boundaries and alloy-scale interface [17]. Research at the General Electric Company resulted in the development of several new overlay coating and alloys containing 2 % at. hafnium and/or zirconium and up to 5 % at. chromium [18, 7]. Oxidation resistance of these coatings was comparable to modern (Ni,Pt) diffusion coatings.

Chemical vapour deposition process consists of the following sub-processes [10]:

- transport of the gas reagent to the substrate surface,
- adsorption of the gas reagent on the substrate surface,
- chemical reaction between the gas reagent and the substrate elements,
- nucleation and growth of the coating,
- desorption of the unnecessary reaction product.

Electron beam physical vapour deposition (EB-PVD) is an advanced coating fabrication technique reported by [11]. Guo, Sun, Gong [12] alleged the lack of evidence about the use of EB-PVD coating technique for aluminide coating deposition. In this study hafnium was incorporated to the aluminide coating by the EB-PVD method. Coatings deposited in two different ways. In the first way a hafnium layer was deposited by the EB-PVD method, subjected to the diffusion treatment for 6 hours and than aluminum was deposited by the CVD method. In the second method, double layers of hafnium (3 μm thick) and aluminum (3 μm thick) were deposited by the EB-PVD method on the nickel substrate. The double layers were subjected to diffusion treatment at 1050 $^0$C for 6 h. The microstructure of hafnium doped aluminide coatings deposited in two different ways was investigated.

## *2. Experiment*

The commercial nickel of 99.95 % wt purity was used in this study. The cylindrical samples of the 20 mm diameter and 5 mm high were cut and grounded up to SiC No 1000, degreased in ethanol and ultrasonically cleaned. Zirconium thin layers (1μm and 3 μm thick) were deposited by the EB-PVD method. In this method, material to evaporate (placed in a water-cooled Cu crucible) is melted by focused high energy electron beam. Power density in electron beam spot (on the surface of the material) can reach over 40 kW/cm$^2$ and any material around the spot can be easily evaporated. Well-cooled walls of crucible, protect the material against contamination by Cu. After the evaporation process, material can be easily evacuated (it does not stick to the crucible). Additional advantage of this method is that material can have any form (wire, sheet pieces, pellets, etc) and can be easily supplemented in the crucible. For this work Balzers ESQ 110 (four hearts crucible) electron beam evaporator was used. Electrons emitted from a hot tungsten cathode (Fig. 1), are initially focused by the Wehnelt electrode than, are accelerated by the electric field to the anode and achieve energies up to 10 keV. Under the influence of the magnetic field, electron beam is focused and deflected (by an angle of 270º), forming on the surface of the material in the crucible a high energy electron spot. Due to four hearts crucible of ESQ 110, it is possible to obtain up to 4 different material layers on the substrate in one vacuum process.

All layers were deposited on motionless Ni substrates. The distance between the evaporating source (crucible) and substrates was 150 mm.

In this conditions, the rate of the material deposition (v) depends on the electron beam power:

$$P_E = U_E \times I_E \quad (1)$$

where $U_E$ – anode voltage and $I_E$ – electron beam current (cathode emission current).

Deposition rates for Hf were established as follows:

$v_{Zr}$ = 1,0 μm/min for $I_E$ = 310 mA, $U_E$ = 9,5 kV

Technological stages for Hf layers deposition were as follows:

- substrates cleaning in a detergent and placing in a substrates holder
- pumping the chamber to p = $2\times 10^{-6}$ hPa
- substrate heating to 300 ºC ($t_H$ = 20 min)
- evaporation of the Hf layer with the deposition rate (v) mentioned in order to obtain the proper coating thickness (evaporation time $t_E$ = 50 s )
- crucible rotation (changing the position to another material)
- cooling substrates to 50 ºC (about 1 hour)
- venting the chamber.

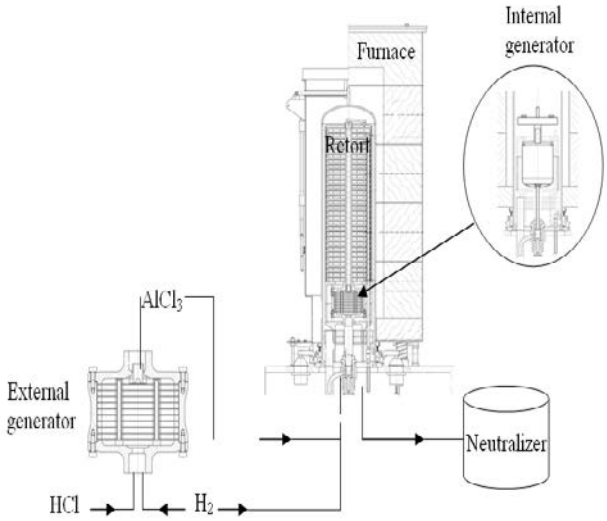



***Fig.1.*** *Scheme of the apparatus of the EB-PVD method.*

The aluminide coatings were made using the CVD equipment BPXPR0325S manufactured by IonBond company (Fig. 2). aluminizing process was conducted for 8h at the temperature 1000 °C. Aluminium chloride vapour ($AlCl_3$) was produced in an external generator I (Fig. 1), at 330 °C according to the reaction: $2Al+6HCl\rightarrow 2AlCl_3+3H_2$. Then the saturating atmosphere was transported in a stream of hydrogen gas into the CVD reactor, where nickel samples were placed. The $AlCl_3$ vapour reacted with the nickel at the temperature 1000 °C and grains of intermetallic phase NiAl were formed according to the reaction:

$2AlCl_3+2Ni+3H_2 \rightarrow 2AlNi+6HCl$

The microstructure of the surface and cross-sections of the coatings were investigated by an optical microscope Nikon Epiphot 300, a scanning electron microscope (SEM) Hitachi S-3400N and an energy dispersive spectroscope (EDS). The coatings thicknesses were determined by means of the NIS-Elements software.

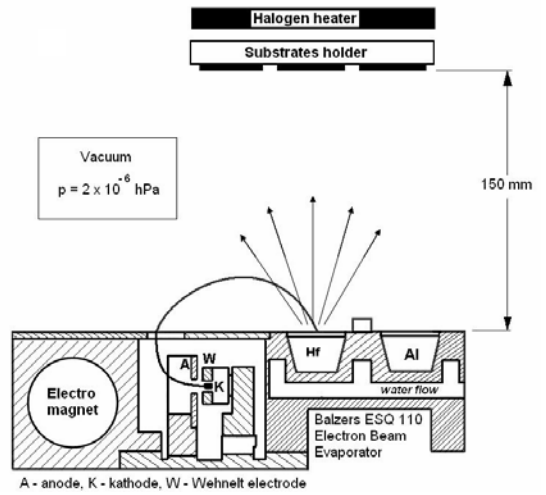



***Fig. 2.*** *A scheme of equipment for deposition of aluminide coatings by the CVD method.*

## *3. Results and discussion*

The microstructure of coatings in which both hafnium and aluminum were deposited by the EB-PVD method and than subjected to diffusion treatment for 6 hours is presented in Figure 3. The diffusion treatment leads to formation of the γ – Ni(Al) phase in which inclusions of the phase enriched with hafnium are observed. According to the Ni-Hf phase diagram [19], chemical composition of these phases corresponds to the $Ni_5Hf$ phase. The EDS linear analysis on the cross-section indicates that intermetallic phases are distributed up to about 20 μm below the samples surfaces (Fig. 4).

After the diffusion treatment process, hafnium formed the $Ni_5Hf$ intermetallic phase, whereas aluminum did not form any phases with nickel nor hafnium. Its concentration is almost the same along the investigated cross-section. Therefore, it may be assumed that aluminum dissolves in nickel and γ-Ni(Al) solid solution is being formed.

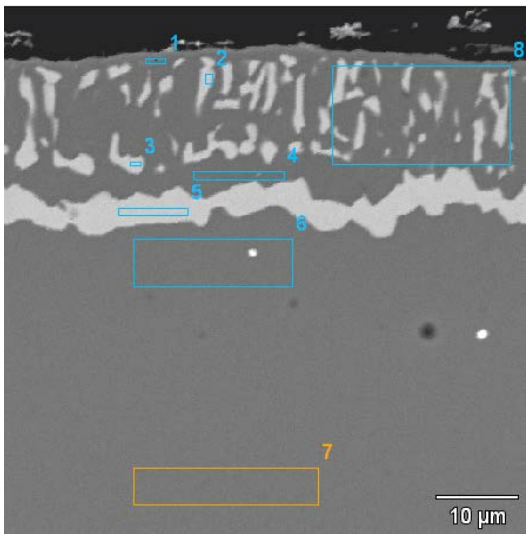



***Fig.3.*** *Microstructure on the cross-section of the Hf 3 μm thick and Al 3 μm thick coatings deposited by the EB-PVD method after the 6h diffusion treatment*

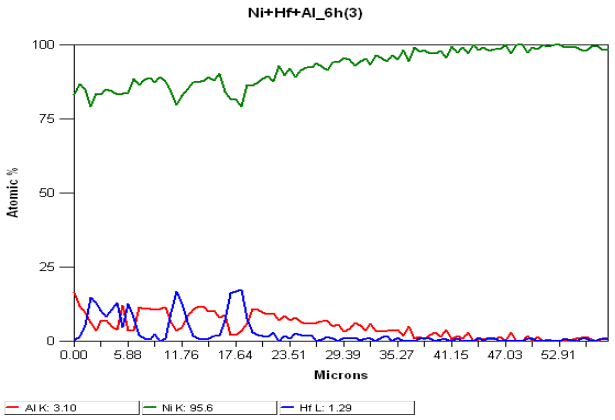



***Fig. 4.*** *EDS linear analysis on the cross-section of the Hf 3 μm thick and Al 3 μm thick coatings deposited by the EB-PVD method after the 6h diffusion treatment*

***Table 1.*** *Chemical composition on the cross-section of the Hf 3 μm thick and Al 3 μm thick coatings deposited by the EB-PVD method after the 6h diffusion treatment*

| Point | Phase | Chemical composition, % at | | |
|---|---|---|---|---|
| | | Al | Ni | Hf |
| 1 | γ-Ni(Al) | 9.86 | 88.38 | 1.76 |
| 2 | $Ni_5Hf$ | - | 88.5 | 14.28 |
| 3 | $Ni_5Hf$ | - | 85.76 | 14.24 |
| 4 | γ-Ni(Al) | 7.44 | 85.69 | 6.87 |
| 5 | $Ni_5Hf$ | - | 86.54 | 13.46 |
| 6 | γ-Ni(Al) | 5.25 | 94.02 | 0.73 |
| 7 | Ni | - | 100.00 | - |
| 8 | γ-Ni(Al)+$Ni_5Hf$ | 8.89 | 87.36 | 3.75 |

The microstructure of the coating deposited by both EB-PVD and CVD methods is presented in Figure 6. The phase enriched with hafnium is formed 25 μm below the sample's surface. Its chemical composition corresponds to the $Ni_2AlHf$ phase. The chemical composition of the above area corresponds to the β-NiAl, whereas the chemical composition of the area below, corresponds to the γ'-$Ni_3Al$.

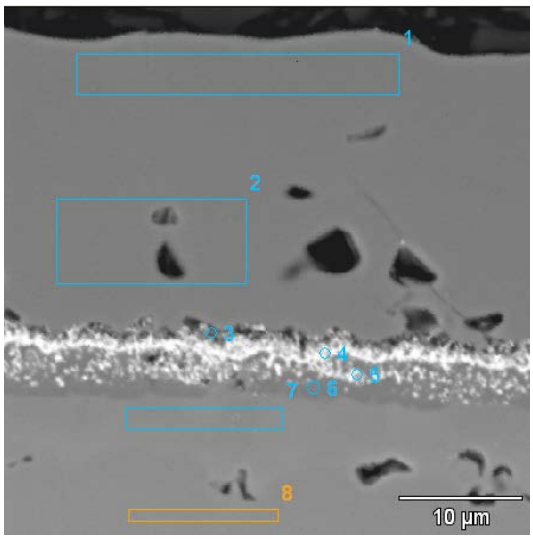



***Fig. 5.*** *Microstructure on the cross-section of the Hf 3 μm thick coatings deposited by EB-PVD method after the 6h diffusion treatment and Al deposition by the CVD method*

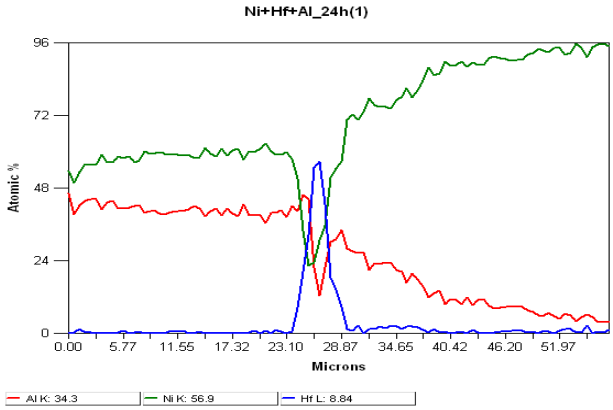



***Fig. 6.*** *EDS linear analysis on the cross-section of the Hf 3 μm thick coatings deposited by EB-PVD method after the 6 h diffusion treatment and Al deposited by the CVD method*

***Table 2.*** *Chemical composition on the cross-section of the Hf 3 μm thick coatings deposited by EB-PVD method after the 6 h diffusion treatment and Al deposited by the CVD method*

| Point | Phase | Chemical composition, % at | | |
|---|---|---|---|---|
| | | Al | Ni | Hf |
| 1 | β-NiAl | 42.92 | 56.95 | 0.13 |
| 2 | β-NiAl | 39.22 | 60.61 | 0.16 |
| 3 | $Ni_2AlHf$ | 40.46 | 48.00 | 11.54 |
| 4 | $Ni_2AlHf$ | 31.95 | 31.38 | 36.67 |
| 5 | $Ni_2AlHf$ | 30.48 | 53.01 | 16.51 |
| 6 | γ'-$Ni_3Al$ | 36.65 | 61.81 | 1.54 |
| 7 | γ'-$Ni_3Al$ | 24.84 | 73.74 | 1.41 |
| 8 | γ'-$Ni_3Al$ | 12.13 | 87.69 | 0.17 |

## *4. Conclusion*

The method of aluminum deposition on the nickel substrate with hafnium layers (3 μm thick) has a tremendous effect on the microstructure of the coatings. In coatings deposited by the EB-PVD method aluminum dissolves in nickel, the γ-Ni(Al) phase is being formed and inclusions enriched with hafnium are distributed in the whole coating. The chemical composition of thease inclusions correspond to the $Ni_5Hf$ phase. On the other hand, aluminum deposited by the CVD method forms intermetallic compounds with nickel (β-NiAl and γ'-$Ni_3Al$ phases) and hafnium forms the $Ni_2AlHf$ phase. This phase lies 25 μm below the coatings surface, between the β-NiAl and γ'-$Ni_3Al$ zones. The coating was formed through aluminum invard diffusion and nickel outward diffusion. Both aluminum and nickel diffused through the hafnium layer.

## *Acknowledgment*

The presented research was supported by the Ntional Science Centre, Poland, project number 2011/01/B/ST8/05036.

## *4. Literature*

[1] J.A. Haynes, Y. Zhang, K.M. Cooley, L. Walker, K.S. Reeves, B.A. Pint, Surf .Coat. Technol. 189 (2004) 153-157.
[2] M. Zagula-Yavorska, J. Sieniawski, T. Gancarczyk, Archives of Metallurgy and Materials. 57 (2012) 503-509.
[3] M. Zagula-Yavorska J. Sieniawski, JMEPEG 23 (2014) 918–926.

[4] J.A. Haynes, K.L. More, B.A. Pint, I.G. Wright, K. Cooley, Y. Zhang, High Temperature Corrosion and Protection of Materials. 5 (2000) 35.
[5] Y. Niu, W. Wu, D. Boone, J. Smith, J. Zhang, C. Zhen, Journal de physique IV. 3(1993) 511-519.
[6] W.T. Griffiths, L.B. Pfeil, U.K. Patent 459848 (1937).
[7] Y. Wang, M. Suneson, Sayre G, Surface&Coating Technology. 15 (2011) 1218-1228.
[8] B.A. Pint, I.G Wright, W. Lee, Y. Zhang, Mater. Sci. Eng A. 245 (1998) 201
[9] V. K. Tolpygo, K.S. Murphy, D. R. Clarke, Acta Mater. 56 (2008) 489.
[10] R. Tricot, Mem. Etud, Sci. Rev. Metall. 88(1991) 747.
[11] A.W. Cocchardt, W. Township, US patent 3005705 (1961).
[12] B. M. Warnes, D.C. Punola, J.S. Smith, D.L. Near, U.S. Patent 6689422 (2004).
[13] B. M.Warnes, Surface Coating Technology. 146-147 (2001) 7.
[14] G.Y. Kim, L.M. He, J.D. Meyer, A. Quintero, J.A. Haynes, W.Y. Lee, Metall. Mater. Trans. A, 35 (2004) 3581.
[15] J.A. Nesbitt, B. Nagaraj, Warrendale, PA. (2001) 78– 92.
[16] B.M. Warnes, Surf. Coat. Technol. 146–147 (2001) 7.
[17] B. Ning, M. Shamsuzzoha, M.L. Weaver, Surface & Coatings Technology. 200 (2005) 1270 – 1275.
[18] B.A. Nagaraj, J. L. Williams, U.S. Patent 6602356 (2003).
[19] K.P. Gupta, Journal of Phase Equilibria, 22 (2001) 69-75.

# CVD AND EB-PVD AS A METHODS OF THE ZIRCONIUM INTRODUCING TO THE ALUMINIDE COATINGS

PhD M. Zagula-Yavorska*, Prof. J. Sieniawski

Rzeszów University of Technology, Department of Materials Science W. Pola 2 str., 35-959 Rzeszów, Poland

E-mail: *yavorska@prz.edu.pl

***Abstract:*** *Zirconium was introduced to the aluminide coating by means of two methods: the EB-PVD method and the CVD method. Zirconium layers (1 and 3 μm thick) were deposited by the EB-PVD method on the pure nickel substrate. Than samples were aluminized by the CVD method. Aluminizing process leads to obtain triple zone coatings. The top ß-NiAl zone, the middle γ'-$Ni_3Al$ zone and the inner γ - Ni(Al) zone were observed. Intermetallic phases NiZr($NiZr_2$) and $Ni_5Zr$ on the border between the top and the middle zone and middle zone and thesubstrate were found. When zirconium was introduced to the aluminide coating during the CVD process a triple zone coating was obtained. It was found that zirconium is dissolved in the NiAl phase.*

**Keywords**: ALUMINIDE COATINGS, CVD AND EB-PVD METHODS, ZIRCONIUM, MICROSTRUCTURE

## *1. Introduction*

Materials used to the turbine elements production have to be resistant to high temperatures.

The usage of directionally crystallized superalloys and single superalloys leads to the increase of the temperature of turbine elements work up to 1100 °C. Further increase of the temperature and times of turbine exploitation is possible by the use of the protection coatings. Literature data indicates that now about 75 % of the elements of aircraft engines have protective layers or coatings [1]. Coatings used in the aircraft industry are still being developed and elaborated. The widest investigations are performed for four kinds of coatings: erosion resistance coatings, thermal barrier coatings, seal coatings and oxidation resistant coatings [2-6].

Oxidation resistant coatings protect substrate materials from corrosion and oxidation.

Coatings increase stability of turbine blades and vanes. Nonmodified and modified aluminide coatings are widely used. Addition of small amount of reactive elements such as zirconium, yttrium or hafnium to aluminide coatings has beneficial effects on the oxidation behavior. This beneficial effects include improvement of adhesion of alumina scales and reduction of oxide scale growth rate [6-7]. Zirconium co-deposition with aluminum on the nickel superalloy by the CVD process was investigated by ONERA and SNECMA. Zirconium provided by the $ZrOCl_2 \cdot 8H_2O$ activator [8] locates far below the coating's surface, at the interface between the β-NiAl coating and the interdiffusion zone. This interface corresponds to the initial surface of the superalloy and zirconium deposition occurs at the beginning of the process. The interdiffusion zone consists of the β-NiAl matrix and phases containing additional elements from the superalloy (Cr, Co, W, Al, Ti, Mo) [8]. During oxidation zirconium migrates towards the surface and the Zr distribution in the whole oxide layer becomes homogeneous. Zirconium may migrate via NiAl grain boundaries, where it is known to segregate [9]. Thus, Zr present in the oxide, can be expected to modify the stress relief by reducing the oxide creep rate. Aluminide coatings are produced by pack cementation, above-the-pack or chemical vapour deposition methods.

The chemical vapour deposition method has several advantages in comparison to other processes. It allows deposition of the aluminide coatings on the internal cooling canals of the turbine blades, control of the batch cooling rate and provides heat treatment of the alloys that reduces cost of the process. The chemical vapour deposition process consists of the following sub-processes [10]:

- transport of the gas reagent to the substrate surface,
- adsorption of the gas reagent on the substrate surface,
- chemical reaction between the gas reagent and the substrate elements,
- nucleation and growth of the coating,
- desorption of the unnecessary reaction products.

Electron beam physical vapour deposition (EB-PVD) is an advanced coating fabrication technique [11]. Guo, Sun and Gong [12] alleged the lack of evidence about the use of EB-PVD technique for aluminide coating deposition. In this study zirconium was incorporated to the aluminide coating by the CVD method. Zirconium layers (1 and 3 μm thick) were also deposited by the EB-PVD method on pure nickel substrate. Than samples were aluminized by the CVD method. The microstructure and hardness of zirconium doped aluminide coatings were examined.

## *2. Experiment*

The commercial nickel of 99.95 % wt purity was used in this study. The cylindrical samples of 20 mm diameter and 5 mm high were cut and grounded up to SiC No 1000, degreased in ethanol and ultrasonically cleaned. Zirconium thin layers (1μm and 3 μm thick) were deposited by the EB-PVD method. In this method, material to evaporate (placed in a water-cooled Cu crucible) is melted by focused high energy electron beam. Power density in electron beam spot (on the surface of the material) can reach over 40 kW/cm$^2$ and any material around the spot can be easily evaporated. Well-cooled walls of crucible protect the material against contamination by Cu. After the evaporation process, material can be easily evacuated (it does not stick to the crucible). Additional advantage of this method is that material can be of any form (wire, sheet pieces, pellets, etc) and can be easily introduced to the crucible. For this work Balzers ESQ 110 (four hearts crucible) electron beam evaporator was used. Electrons emitted from a hot tungsten cathode (Fig. 1), are initially focused by the Wehnelt electrode than, are accelerated by the electric field to the anode and achieve energies up to 10 keV. Under the influence of the magnetic field, electron beam is focused and deflected (by an angle of 270º), forming on the surface of the material in the crucible a high energy electron spot. Due to four hearts crucible of ESQ 110, it is possible to obtain up to 4 different material layers on the substrate in one vacuum process.

All layers were deposited on motionless Ni substrates. The distance between the evaporating source (crucible) and substrates was 150 mm.

In this conditions, the rate of the material deposition (v) depends on the electron beam power:

$$P_E = U_E \times I_E \qquad (1)$$

where $U_E$ – anode voltage and $I_E$ – electron beam current (cathode emission current).

Deposition rates for Zr were established as follows:

$v_{Zr}$ = 1.0 µm/min  for $I_E$ = 310 mA,  $U_E$ = 9.5 kV

Technological stages for Zr layers deposition were as follows:

- substrates cleaning in a detergent and placing in a substrates holder
- pumping the chamber to p = 2× $10^{-6}$ hPa
- substrate heating to 300 ºC ($t_H$ = 20 min)
- evaporation of the Zr layer with the deposition rate (v) mentioned in order to obtain the proper coating thickness (evaporation time $t_E$ = 50 s )
- crucible rotation (changing the position to another material)
- cooling substrates to 50 ºC (about 1 hour)
- venting the chamber.

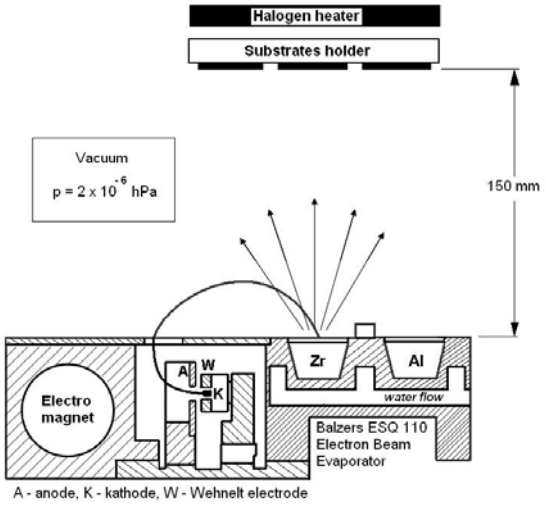



***Fig.1.*** *Scheme of the apparatus of the EB-PVD method.*

The aluminide coatings were made using the CVD equipment BPXPR0325S manufactured by IonBond company (Fig. 2). aluminizing process was conducted for 8h at the temperature 1000 °C. Aluminium chloride vapour ($AlCl_3$) was produced in an external generator I (Fig. 1), at 330 °C according to the reaction: $2Al+6HCl \rightarrow 2AlCl_3+3H_2$. Then the saturating atmosphere was transported in a stream of hydrogen gas into the CVD reactor, where nickel samples were placed. The $AlCl_3$ vapour reacted with the nickel at the temperature 1000 °C and grains of intermetallic phase NiAl were formed according to the reaction:

$2AlCl_3+2Ni+3H_2 \rightarrow 2AlNi+6HCl$

Zirconium was also incorporated during the CVD process. Zirconium chloride vapour was produce in an external generator at 440 °C according to the reaction: $2Zr+6HCl \rightarrow 2ZrCl_3+3H_2$. The saturated atmosphere was transported in a stream of hydrogen gas into the CVD reactor, where nickel samples were placed. The $AlCl_3$ and $ZrCl_3$ vapour reacted with nickel and intermerallic phase NiAl(Zr) was formed.

The microstructure of the surface and cross-sections of the synthesized coatings were investigated by an optical microscope Nikon Epiphot 300, a scanning electron microscope (SEM) Hitachi S-3400N and an energy dispersive spectroscope (EDS). The coatings thicknesses were determined by means of the NIS-Elements software.

Phase composition of investigated coatings was executed using ARL X'TRA X- ray diffractometer, equipped with a filtered copper lamp with the voltage of 45kV and heater current of 40mA.

Adhesion evaluation of the layers was made using the scratch test on the CSM REVETEST device, by moving the diamond indenter along the examined specimen's surface with the gradually increasing load.

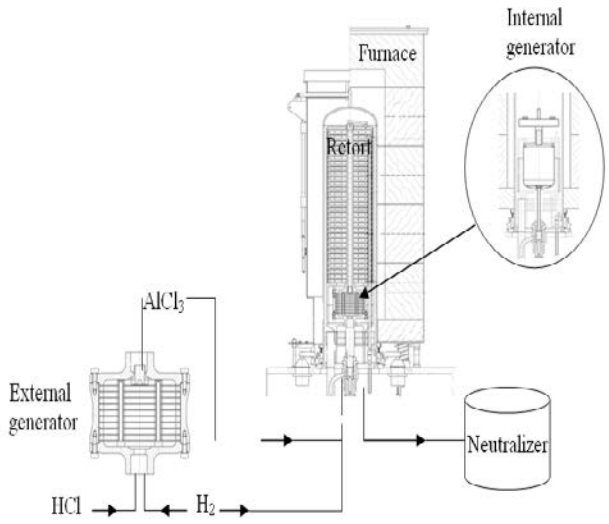



***Fig. 2.*** *A scheme of equipment for deposition of aluminide coatings by the CVD method.*

## *2. Results and discussion*

The zirconizing - aluminizing CVD process of the nickel substrate at 1050 °C during 8 h leads to the triple zone aluminide coating formation (50 µm thick). In the first zone, on the top of the coating, the proportion of Ni to Al corresponds to the β-NiAl phase (Fig. 3, table 1). The chemical composition of the second zone, which is adjacent to the β-NiAl phase, corresponds to the γ' – $Ni_3Al$ phase (Fig. 4). The chemical composition of the third, inner zone, corresponds to the γ – Ni(Al) phase. Chemical composition of the zone below γ – Ni(Al) phase is same as the matrix composition, that is pure nickel. Zirconium does not form any inclusions, but dissolves in the coatings phases.

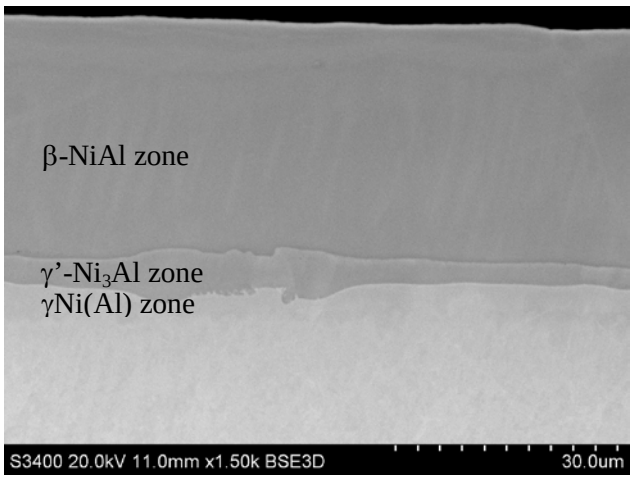



***Fig. 3.*** *Microstructure of the zirconium aluminide coating deposited by CVD method on the nickel substrate. Deposition temperature 1050 ℃, time 8h.*

Wang et al. [13] proved that enthalpy of the NiAl phase formation is about -67 kJ/mol at 1000 °C. Enthalpy of the $Ni_3Al$ phase formation is about -42 kJ/mol at 1000 °C. Small values of the enthalpy of formation indicate on the favorable conditions of the intermetallic phase formation.

XRD phase analysis confirmed the existence of the NiAl phase in the coating (Fig. 5).

**Table 1:** *Phase and chemical composition of the zirconium aluminide coating deposited by CVD method on the nickel substrate. Deposition temperature 1050 ℃, time 8h (Fig. 3).*

| Phase | Chemical composition, % at | | |
|---|---|---|---|
| | Al | Zr | Ni |
| β-NiAl | 41.14 | 0.28 | 58.58 |
| γ'-$Ni_3Al$ | 26.17 | 0.23 | 73.6 |
| γ-Ni(Al) | 6.58 | 0.20 | 93.22 |
| Ni | - | | 100 |

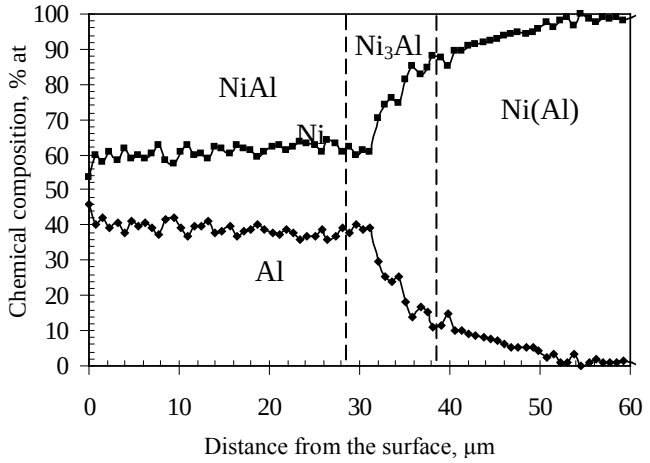



***Fig. 4.*** *Chemical composition on the cross-section of the zirconium aluminide coating deposited by CVD method on the nickel substrate.*

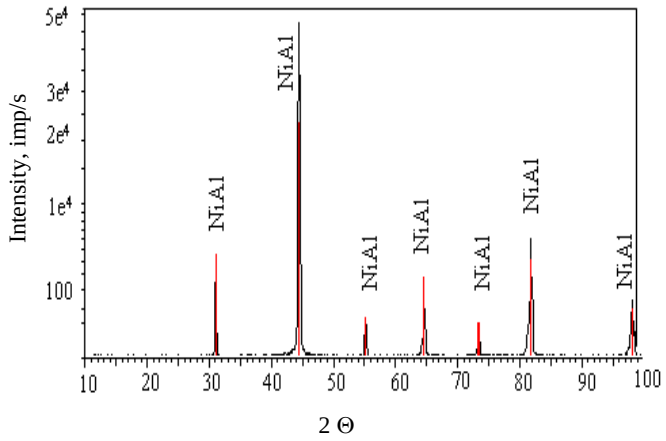



***Fig. 5.*** *XRD results of aluminide coating deposited by CVD method on the nickel substrate.*

The results of the scratch test revealed that layers obtained by the EB-PVD method have good adhesion to the nickel substrate. The load from 0 to 10 N does not lead to destruction of layers. Aluminizing process of the zirconium layer (1 μm thick) deposited on the nickel substrate leads to the $Ni_5Zr$ intermetallic phase formation at the boundary of the $Ni_3Al$ and Ni(Al) phases (Fig. 6). Large zirconium content (about 56 % at) was found at the boundary of the top zone (ß-NiAl phase) and the second zone (γ'-$Ni_3Al$ phase) (Table 2, Fig. 7).

Chemical composition at the phase boundary between the NiAl and $Ni_3Al$ corresponds to the NiZr and $NiZr_2$ phases according to the Ni-Zr phase diagram.

The increase of the zirconium layer thickness from 1 to 3 μm before aluminizing process does not change both phase and chemical composition of the aluminide coating. Aluminide coating consists of three zones (Fig. 8). The $Ni_5Zr$ phase was found at the $Ni_3Al$/Ni(Al) zone boundary (Table 3).

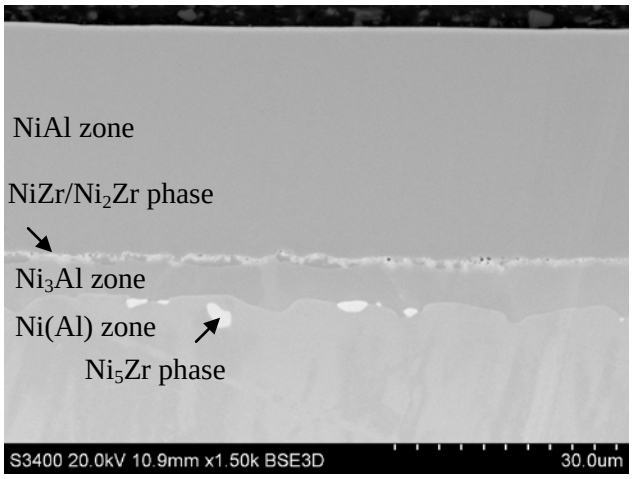



***Fig. 6.*** *Microstructure of the zirconium modified (1 μm zirconium thick deposited by EB-PVD method) aluminide coating deposited by CVD method on the nickel substrate. Deposition temperature 1050 ℃, time 8h.*

**Table 2:** *Phase and chemical composition of the zirconium modified (1 μm zirconium thick deposited by EB-PVD method) aluminide coating deposited by CVD method on the nickel substrate. Deposition temperature 1050 ℃, time 8h (Fig.6).*

| Phase | Chemical composition, % at | | |
|---|---|---|---|
| | Al | Ni | Zr |
| β-NiAl | 41.0 | 59.0 | - |
| NiZr/$Ni_2Zr$ | 7.25 | 36.31 | 56.45 |
| γ'-$Ni_3Al$ | 23.75 | 74.71 | 1.54 |
| $Ni_5Zr$ | - | 84.17 | 15.83 |
| γ-Ni(Al) | 6.58 | 93.42 | - |

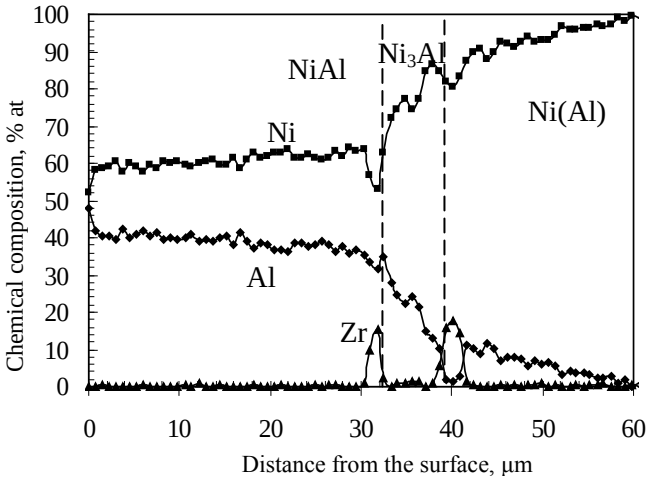



***Fig. 7.*** *Chemical composition on the cross-section of the zirconium modified (1 μm zirconium thick deposited by EB-PVD method) aluminide coating deposited by CVD method on the nickel substrate.*

The volume fraction of the $Ni_5Zr$ phase was greater compared to the zirconium modified aluminide coating – 1 μm zirconium layer deposited before aluminizing.

Enthalpy of the $Ni_5Zr$ phase formation is about -30 kJ/mol at the 1000 °C temperature [13]. Hardness of the $Ni_5Zr$ intermetallic phase is about 800 HV.

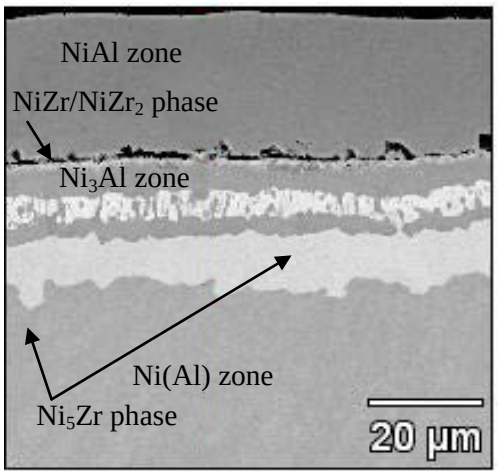



***Fig. 8.*** *Microstructure of the zirconium modified (3 µm zirconium thick deposited by EB-PVD method) aluminide coating deposited by CVD method on the nickel substrate. Deposition temperature 1050 °C, time 8h.*

**Table 3:** *Phase and chemical composition of the zirconium modified (3 µm zirconium thick deposited by EB-PVD method) aluminide coating deposited by CVD method on the nickel substrate. Deposition temperature 1050 °C, time 8h (Fig. 8).*

| Phase | Chemical composition, % at | | |
|---|---|---|---|
| | Al | Ni | Zr |
| β-NiAl | 40.98 | 58.95 | - |
| NiZr/$Ni_2Zr$ | - | 43.07 | 56.94 |
| γ'-$Ni_3Al$ | 22.82 | 73.97 | 3.21 |
| $Ni_5Zr$ | - | 83.86 | 16.14 |
| γ-Ni(Al) | 6.6 | 93.40 | - |

## *3. Conclusion*

The zirconizing - aluminizing CVD process of the nickel substrate at 1050 °C during 8 h leads to the triple zone aluminide coating formation. Zirconium does not form any inclusions, but dissolves in the coatings phases. Hardness of aluminide coating is about 500 HV. Zirconium layers 1 and 3 µm thick were also deposited onto the Ni substrate by the EB-PVD method. The layers have a good adhesion to the Ni substrate.

The structure of zirconium modified (1 and 3 µm thick deposited by EV-PVD method) aluminide coating is the same as aluminide coating deposited by the CVD method. The zirconium serves as marker and forms inermetallic phases $Ni_5Zr$ and NiZr or $NiZr_2$. The intermetallic phases are located at the boundary between the top and inner zones and the inner zone and the substrate. The increase of zirconium layer thickness from 1 to 3 µm does not change phase and chemical composition of the aluminide coating. The volume fraction of the $Ni_5Zr$ phase was greater than in the zirconium modified aluminide coating - 1 µm zirconium layer thick. Hardness of the $Ni_5Zr$ intermetallic phase is about 800 HV.

## *Acknowledgment*

The presented research was supported by the National Science Centre, Poland, project number 2011/01/B/ST8/05036.

## *4. Literature*

[1] Sudhangshu B., High temperature coatings, Butterworth-Heinemann, Oxford 2007
[2] Angenete J., Aluminide diffusion coatings for Ni base superalloys, Chalmers University of Technology, Goteborg, Sweden, 2002
[3]. Wright I., Gibbons T., Recent developments in gas turbine materials and technology and their implications for syngas firing, International Journal of Hydrogen Energy, 32 (2007), 3610-3621
[4] Voudouris N., Christoglou Ch., Angelopoulos G., Formation of aluminide coatings on nickel by a fluidised bed CVD process, Surface & Coatings Technology, 141(2001), 275-282
[5] Hodge A.M. , Durand D.C., Synthesis of nickel–aluminide foams by pack-aluminization of nickel foams, Intermetallics, 9 (2001), 581–589
[6] Pint B., Haynes T., Besmann T., Effect of Hf and Y additions on aluminide coating performance, Surface & Coatings Technology, 205 (2010) 3287-3293
[7] Wang Y., Suneson M., Sayre G., Synthesis of Hf – modified aluminide coatings on Ni-base superalloys, Surface & Coatings Technology 206 (2011) 1218-1228
[8] Hamadi S., Bacos M., Poulain M., Seyeux A., Maurice V., Marcus P., Oxidation resistance of a Zr–dopped NiAl coating thermochemically deposited on a nickel-based superalloy, Surface & Coatings Technology 204 (2009) 756-760
[9] Larson D., Miller M., Atom probe field-ion microscopy characterization of nickel and titanium aluminides, Mater. Charact. 44 (2000) 159
[10] Zagula-Yavorska M., Sieniawski J.: Microstructural study on oxidation resistance of nonmodified and platinum modified aluminide coating, Journal of Materials Engineering and Performance, 23 (2014) 918–926
[11] Movchan B.: Functionally graded EB PVD coatings, Surface and Coatings Technology, 149 (2) (2002) 252-262
[12] Guo H., Sun L., Li H., Gong S.: High temperature oxidation behavior of hafnium modified NiAl bond coat in EB-PVD thermal barrier coating system. Thin Solid Films 516 (2008) 5732-5735
[13] Wang N., Changrong L., Zhenmin D., Fenge W., Experimental study and thermodynamic re-assessment of the Ni-Zr system, CALPHAD 31 (2007) 413-421

# THE TERMOGRAPHIC ANALYSIS OF THE WELDING BY TIG

M.Sc., Eng. Maś K., M.Sc. Woźny M., PhD. Marchewka M. , PhD. Płoch D. and Prof. Dr.Sheregii E.M.

Centre for Microelectronics and Nanotechnology, University of Rzeszow, Poland

kinga04@interia.pl

**Abstract**: *Thermography measurements allow to detect the defects that may appear on a joint at welding of components. Energy pulse generated by a xenon lamp with adequate power in a short period of time is sufficient for thermal excitation and enables to register the temperature distribution using the thermography high resolution camera FLIR SC7000. The impulse with 6kJ energy and 6ms time generate sufficient power to measure the temperature distribution on the surface of the weld tested. During cooling the temperature of the area with defect changes more slowly than in the areas without defects, because of to the less intense heat dissipation. This allows the registration of defects in welds "on-line" at the production process. Material used for analysis detection of defects in the welded joints is Inconel 718, stainless steel 410 and stainless steel 321. The peak energy which flow throw the samples with defects in the welded joints its completely or partially blocked. It cause different temperature distribution on the surface in the places where the connection discontinuity take place.*

Keywords: THERMOGRAPHY, DEFECTS, WELDING, NDT

## *1. Introduction*

Welded joints and padding layers are subjected to control processes through the use of non-destructive testing methods to ensure a high quality semi-finished and finished products [1-3]. Depending on liability and class of structure an individual and single method or a complex of few (usually two independent parallel testing methods), are chosen. Radiographic and fluorescent weld inspection are used as two most common nondestructive testing (NDT) methods to detect discontinuities within the internal structure of welds. The obvious advantage of both of these testing methods is their ability to establish the weld's internal integrity without destroying the welded component. These methods have used widely in industry due to provide information about the test object without reducing its functional properties: they are used to detect defects that can cause damage or destruction of the item [4]. Thermography and thermal imaging include research methods involving remote and contactless evaluation of temperature distribution on the surface of a body [5-7]. This method is based on observation and recording the distribution of infrared radiation emitted by each body, whose temperature is above the absolute zero. If an external source of heat (thermal excitation pulse) is applied the thermography is called as active [8].

In this contribution the active pulse thermography is used for control of welds and results of control are comprised with traditional methods as radiographic and fluorescent methods of testing.

## *2. Materials and methods*

The tests were performed on the samples of number 8, 19 and 23 made from the following materials: Inconel 718, stainless steel 410 and stainless steel 321, respectively.

The fluorescent method of testing includes the observation of defects (discontinuities) present on the surface of welds. Surface cracks and pinholes that are not visible to the naked eye can be located by the liquid penetrant inspection. It is widely used to locate leaks in welds and can be applied with austentic steels and nonferrous materials. Assessment and indications of defects on the test surfaces occur in the ultraviolet lamp light after all stages of penetration testing. The presence of discontinuities (such as cracks, craters) indicate a shining by yellow-green color under the influence of the UV rays.

The radiography (X-ray) is one of the most important, versatile and widely accepted nondestructive method of examination. X-ray-method is used to determine internal quality of the welds. Radiography is based on the ability of X-rays and gamma rays to pass through metal and other materials opaque to ordinary light, and produce photographic records of the transmitted radiant energy. All materials will absorb known amounts of this radiant energy and, therefore, X-rays and gamma rays can be used to show discontinuities and inclusions within the opaque material. The permanent film record of the internal conditions will show the basic information by which the weld reliability and credibility could be determined.

The thermography method show thermograms recorded directly by the IR camera during the measurement or after the computer programme (IrNDT) treatment. Due to this it is possible to traced "step by step" the temperature distribution during of the 100ms time after pulse heat excitation of the sample. The IR camera is registering how the different areas of the sample are conducting the heat because the temperature distribution on the tested surfaces is recording during the heating of sample. The places brighter in the thermograms represent a higher temperature, while the darker – lower temperature.

## *3. Results of testing*

### 3.1 Results of penetration method



***Fig. 1*** *Sample No. 8 made by Inconel 718 alloy.*

In Fig. 1 is shown the results obtained for the penetration method of the sample 8, where two shining areas are observed marked as "a" and "b". In the place marked as "a" shining is lighter what means a deeper discontinuity, with the greater amount of penetrant than the place marked as "b", where shining has a point character.

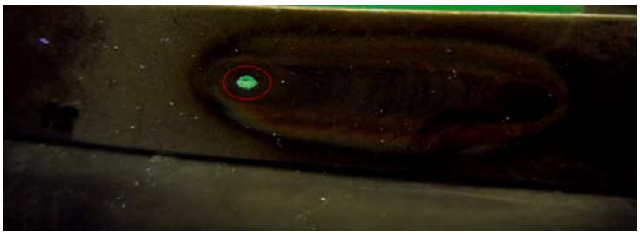


***Fig.2*** *Sample No. 19 made by stainless steel 321*

In Fig.2 is shown the sample with a crater at the end of the pad welding on the left side. The purple color on the surface is coming from a pollution.

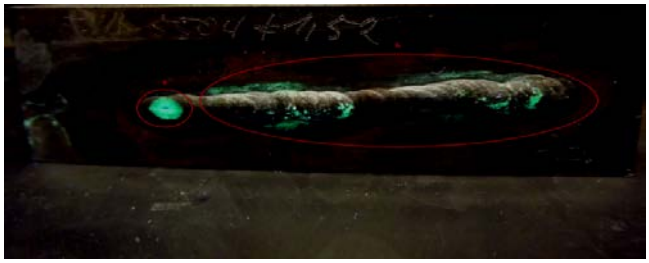


***Fig.3*** *Sample No. 23 made by stainless steel 410*

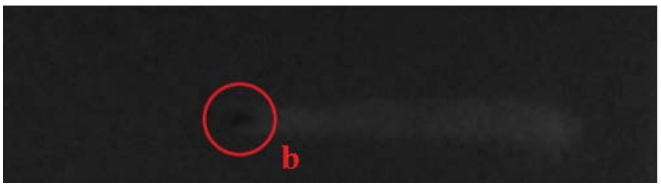
On the surface of the pad welding of the sample 23, shown in Fig.3, the crater is observed also on the left side of sample, which is evidenced by the green-yellow shining of the round shape (area "a"). Others shining places have an irregular shape. They are originated by an inequality and by the roughness of the surface.

### 3.2 The results of radiographic method

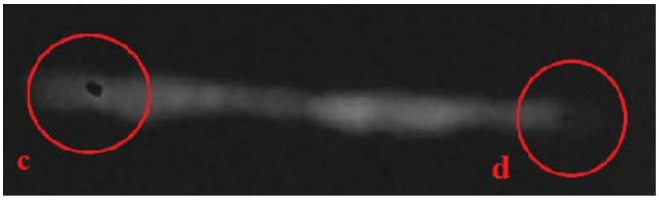
The radiographic testing of the same samples is presented in Figs. 4,5 and 6. It is seen that the dark faults take place on the pictures obtained by the X-ray.




*Fig. 4 Radiogram of weld sample No. 8*




*Figs.5. Radiogram of weld sample No. 19*




*Figs.6 Radiogram of weld sample No.23*

Analysis of the shown in Figs. 4-6 results allows to observe the following particulars:

• in the sample 8 the area "a" indicates that in the place of crater observed by the penetration method (Fig.1) the crack occurs inside the sample;

• the same situation takes place with the sample.

• in the sample 23 are observed not only the cracks inside the sample but a gas bladder exists inside the weld.

So, the faults belong to the internal defects invisible on the surface when the fluorescent method is used, could be observed by X-ray.

### 3.3 The results of thermographic method

In Figs. 7, 8 and 9 are shown the thermograms for the same samples 8, 19 and 23 with welds. Fig.7a show the IR picture obtained for the sample 8 during the heat pulse of the 30 ms time. From the 7a thermographic image, obtained directly by IR camera it couldn't be possible to identify the region of the defects. It is only possible to observe the surface roughness of the weld.

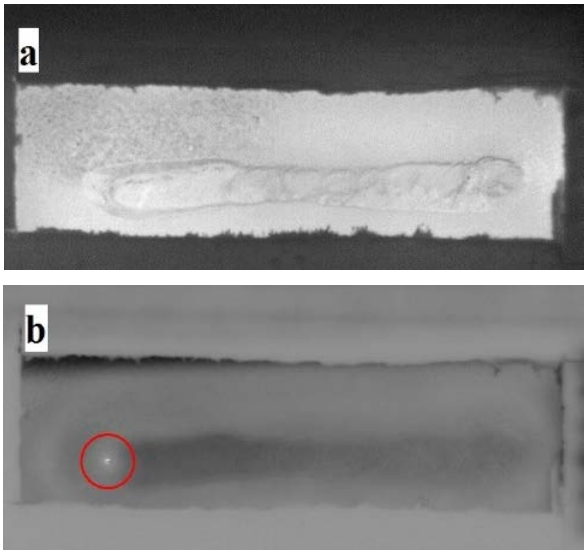



*Fig.7. Thermorams of weld sample no. 8, a-thermogram directly registered by IR camera, b - thermogram obtained after computer treatment in IrNDT program.*

However, the thermogram 7b, obtained after treatment by the IrNDT computer program, enables to find the bright spot (in the area marked with a red circle). Comparing with the radiological and penetration results confirms that this is the crater observed in Figs. 1 and the crack visible in Fig. 4.

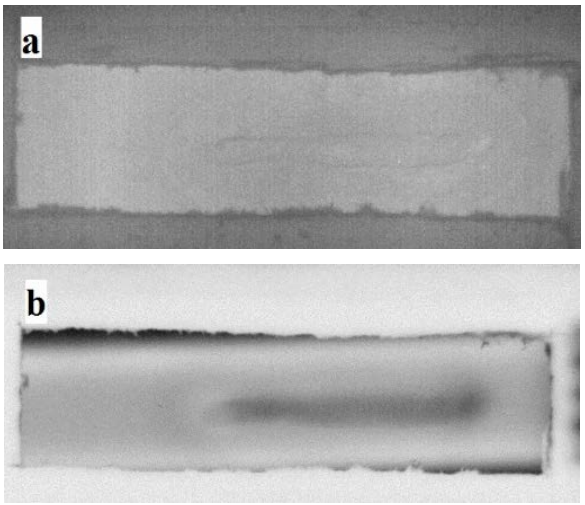



*Fig.8. Thermorams of weld sample no. 19, a-thermogram directly registered by IR camera, b - thermogram obtained after computer treatment in IrNDT program.*

Analogously, in the case of sample 19 shown in Figure 8a, the picture is obtained directly by IR camera, doesn't indicats the defects in the weld. On the thermogram recorded at 50 ms heat pulse and depicted in Fig. 8b the defect observed by penetration (Fig.2) and radiographic (Fig.5) methods, is located at the end of the right side of the weld.

Fig. 9 a,b shows the thermograms of the sample 23 obtained during the 70 millisecond pulse heating. Thermogram in Fig. 9a shows a recess at the end of the weld surface in the right side of sample.

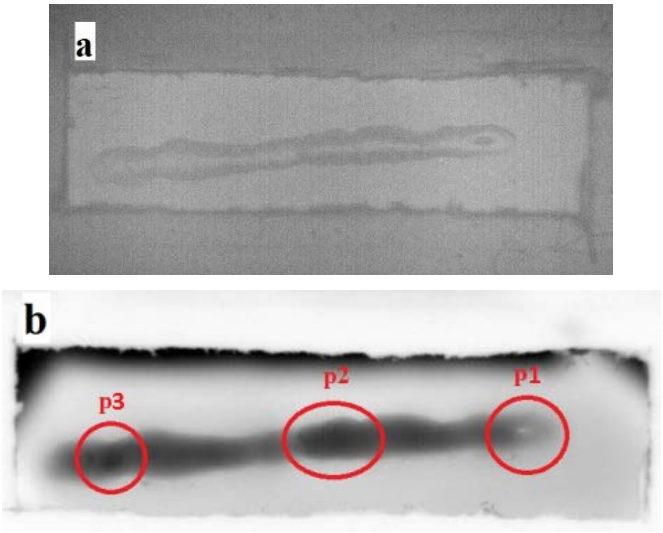



*Fig. 9 Thermorams of weld sample no. 23, a-thermogram directly registered by IR camera, b - thermogram obtained after computer treatment in IrNDT program.*

Fig. 9b shows the thermogram after treatment in IrNDT program. Temperature distribution shows clierly the presence of defects in the weld:

• area "p1" is a place of higher temperature in comparison with surraunding areas. A thickness of the weld material in the area of "p1" have to be smaller because of the presence of a defect. Heat pulse heats the material at this point faster, hence the higher temperature is acheaved (brighter gray level or light spot).

• area of "p2" is a place where the temperature is lower than the temperature at the point "p1". After the visual observation the surface of the sample of the weld, have a larger thickness than that of "p1", because in this point the material was slower heating.

• area "p3" is also a colder place on the weld (darker gray level), in which the temperature was lower than in the area "p1". It has been observed contour defect with circular form.

## *4. Discusson*

The fluorescent method allow to detect the areas where surface discontinuities occurr. Evidence of the defects presence is green-yellow glowing of penetrating substance appearing under the influence of UV rays. The pictures in Figs 1-3 clearly are indicating the presence of surface defects on the welds tested.

Radiographic examination confirms the presence of surface defects detected by the fluorescent method but radiographs revealed the presence of internal defects in the sample 23 (Fig.6) where was observed air bladder. Besides that, the Figs. 5 and 5 registered place of incomplete joint penetration at the ends of joints: the cracks inside the craters, which are not recorded using fluorescent method.

The thermography method enables also to reveal the defects inside the welds. In the region of the defect where crater was observed by fluorescent method (Fig. 1) the bright point is detected in Fig. 7b on a darker background of the rest of the pad welding (lower grades of gray-lower temperature) indicating on the inner defect – crack registered by the radiograph (Fig. 4). Also in the thermogram (Fig.9b) is observed the contours of the bladder registered by radiographic method (Fig.6),where the blackout was greater than in the rest of the pad welding. The reason for this is presence of a gas, which acted as an insulator passing also were heat impulse. On the right side of the sample in Fig 9b internal defect is appeared as a light point. The layer thickness at this point was less due to the presence of the crack in the crater. The area was warmed faster than the rest of the weld.

## *5. Summary*

The comparative analyses is performed using three methods of the weld testing: radiographic method, fluorescent one and thermographic one. Combination of first two method enables to reveal the surface defects on the welded joints and verify possibility of the inner incontinuity presences using radiographs. Thermograms, which are results of the thermographic measurement, allow to visualize location of the defects and determine their type. With the correct preparation the thermography method can replace the above two methods: fluorescent and radiographic. Thermography, based on the detection of infrared radiation with aim to detect defects, is a relatively new field of science, giving new opportunities for development and control of welded joints and other structures and elements to eliminate defective products.

## *References*

[1] J. Nowacki, A. Wypych, Application of thermovision method to welding thermal cycle analysis, Journal of Achievements in Materials and Manufacturing Engineering, 2010.

[2] P. Broberg, A. Runnemalm, Detection of Surface Cracks in Welds using Active Thermography, 18 World Conference on Nondestructive Testing, 16-20 April 2012, Durban, South Africa.

[3] F. C. Sham, C. Nelson, L. Long, Surface crack detection by flash thermography on concrete surface, Insight, vol. 50, pp.240-243, 2008

[4]G. Wang, T. Warren Liao Automatic identification of different types of welding defects in radiographic images, NDT & E International, Volume 35, Issue 8, December 2002, Pages 519–528

[5] V. Valivov, Infrared thermography and thermal control, Moscow, Spectr, 2009

[6] X. Maldague, Theory and Practice of Infrared Technology for Nondestructive Testing, John Wiley – Interscience, New York, 2001

[7] S. Marinetti, Y. A. Plotnikov, W. P. Winfree, A. Braggiotti, Pulse phase thermography for defect detection and visualization, *Proc SPIE* (1999).

[8] Vollmer M., Möllman K.-P.: Infrared Thermal Imaging, Wiley-Vch, N-Y, 2010.

# THE SCANING NOZZLE HOT AIR SYSTEM FOR THERMOGRAPHIC DETECTION OF THE SURFACE INCORPORATED HIDDEN DEFECTS

PhD. Prokhorenko S., M.Sc. Eng. Maś K., M.Sc. Woźny M., and Prof. Sheregii E.M.
Centre for Microelectronics and Nanotechnology, University of Rzeszow, Poland
siergiej.prokhorenko@gmail.com

***Abstract:*** *The scanning nozzle hot air system for thermographic detection of the surface incorporated hidden defects is proposed. Subsurface defects in the sample are detected using the high resolution thermal imaging camera FLIR SC7000. To introduce additional energy in are searched sample, a scanning hot air (about 110°C) nozzle is applied (a patent application P.403346). The hidden defect causes a temperature increase in comparison with the remaining area what is a result of changes in emissivity. The results are compared with the pulse thermography method using the xenon lamp for excitation.*

**Keywords**: THERMOGRAPHY, DEFECTS, SCANNING, NONINVASIVE CONTROL

## *1. Introduction*

The research development based on the IR thermography to detect defects in the surface layer of materials has been observed in the last years. Thermography offers noncontact, wide area detection of subsurface defects, and can be used as an alternative or the complement to the conventional inspection technologies [1-7].

The essence of this research is the thermal response analysis of the material stimulated by the external heat impulse. After supplying specified quantity of energy to the material, for example in the form of a heat pulse, the thermal front begins to move into the material due to the thermal diffusion. The presence of areas containing defects with thermal properties different from areas without defects, causes a change in the diffusion rate what enables to observe the defects location analyzing the temperature distribution on the researched sample surface. [2,5] On the other hand, the size of the detected defects using the pulse thermography method should be not less than few millimeters if a whole surface (usually the macroscopic one) of the researched sample is stimulated [7]. Nevertheless, that is excellent method for express-control of macroscopic specimens.

Other methods of excitation can be used in the thermography detected defects, namely ultrasounds. The ultrasound thermography is used as the interaction between mechanical and thermal waves to detect material defects. If some damage in components absorbs the excitation of high energy ultrasound waves then it is locally heated. The resulting temperature gradient is captured by an infrared camera on the sample surface. This method is suitable for the applications in the cracks detection, adhesion testing and welded joints. It is possible to detect delamination and impact damage in materials using the ultrasound method [8,9].

In this paper a specially designed hot air nozzle as an excitation source with scanning on the sample surface is proposed for the noncontact and noninvasive control of subsurface defects [10]

## *2. Basic theory*

Heat diffusion through a solid is a complex 3D problem that can be described by the Fourier's law of the heat diffusion or the heat equation [11]. The 1D solution of the Fourier equation for the propagation of a Dirac heat pulse, i.e. an ideal waveform defined as an intense unit-area pulse in a semi-infinite isotropic solid, has the form [12,13]:

$$T(t)=T_0 + Q/e(\pi t)^{1/2} \quad (1)$$

where Q is the energy absorbed by the surface and $T_0$ is the initial temperature,

$e$ is the effusivity: $e = (k \rho c)^{1/2}$ (2)

which is a thermal property that measures the material ability to exchange heat with its surroundings and is an important parameter in this method.

If the properties of material ($k$, $\rho$, $c_p$) are changed, the effusivity $e$ is changed too, what causes the local change of temperature $\Delta T$. The time of this change is connected with another parameter – the thermal diffusivity $\alpha$. Any change in the sample temperature is related to the thermal diffusivity α [11],

$$\alpha = k/\rho c \quad (3)$$

where $k$ is the thermal conductivity, $\rho$ is the density and $c$ is the heat capacity at the constant pressure. That is the second very important parameter in the proposed method. The relation between these two parameters ($e$ and $\alpha$) enables to choose the optimal velocity $v$ for scanning of the hot spot as well as the minimal value of the $\Delta T$ necessary to detect a hidden defect.

## *3. Experiment*

A scanning hot air nozzle is mounted on a stationary platform with a high resolution thermal imaging camera FLIR SC7000 (IR camera). The heat flow is directed to the surface of the sample which is placed on the table moving with the selected speed in the direction of $z$ axis (see Fig. 1a,b). The air pressure getting out of the nozzle was 0.2 MPa. The temperature of hot air was 110°C.

Thermography is based on the radiation emission of the objects. Therefore, the emission coefficient $\varepsilon = E/E_s$ as the ratio of emissivity E of a real body to the emissivity $E_s$ of the absolute black body at the same temperature, is important, particularly in the case of the metallic researched surface. It is caused by a small value of the emissivity in comparison with the reflectivity. So, the precise determination of the emission coefficient ε has a principal meaning for the temperature correct measurement.

The IR camera used in this work is operating in the short wave region at 3-5μm. To perform correct measurements of the temperature distribution on the surface. a series of the IR camera settings were made. That is a verification of few parameters for example: emissivity of the object and the distance (this parameter is important because a big part of radiation of the object is absorbed in the air so the distance was 0.5m). On the other hand this distance influences the spatial resolution of the IR camera, which is expected to be maximum.

The sample with dimensions 60mm x 20mm x 5mm was made from C45 steel and contained specially created defects in the form of 5 holes on the back side of a sample with a different size of diameters: 6mm, 5mm, 4mm, 3mm, 2mm.The depth of holes is equal to two thirds of the thickness. Front and back sides of the sample with the scale are shown in Fig. 1b in order to state the positions of holes on the back side.

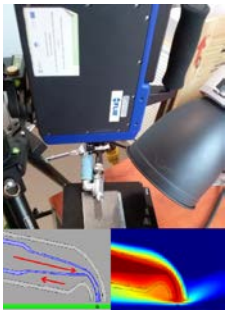
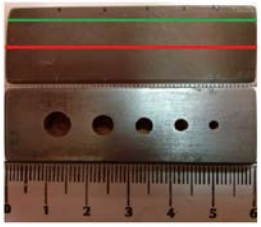
a)  b) 

***Fig. 1.*** *a) Scheme of experiment, a hot air nozzle: hot air is getting from the nozzle of 0.4 mm diameter (blue color in scheme) and sucks up the air reflected from the investigated surface (white color); b) Picture of the sample: front size, back size and scale*

In order to perform precise motion sequences of the sample a motorized positioning system such as an OWIS PKTM 70 table movable in the x, y, z directions, was used. The positioning system (Fig. 1a) enables to choose very precisely the velocity of the sample motion *v*. The velocity value is important from the point of view of the defect detection because the heat diffusion length $L_H = \sqrt{\alpha\tau}$ is determined by the thermal diffusivity α (see the previous chapter) and the next inequality should be fulfilled:

$$d > L_H \qquad (4)$$

where *d* is the size of the defect and $\tau$ is the time of the nozzle going along the defect area: $\tau = d/v$. The equation (4) means that the time $\tau$ is less than the heat diffusion time on the same distance. Therefore, the nozzle velocity is limited by minimum

$$v > \frac{\alpha}{d} \qquad (5)$$

On the other hand, this velocity has a top limit also because it is necessary to register the defect using the change of temperature $\Delta T = Q/e(\pi t)^{1/2}$ as it was shown on the equation (1). The top limit for the nozzle velocity depends on the minimal *Q* value necessary for the efficient temperature change in the defect area, simultaneously the effusivity also influences the $\Delta T$ increase. Thus, the nozzle velocity maximum depends on the material parameters of the examined sample and on the *Q* value delivered by the nozzle. The last one can be derived from the nozzle velocity *v*, the hot air temperature $T_{air}$ and the hot air flux velocity $V_{air} = \Delta V/\Delta t$ ($\Delta V$ is the volume of the hot air getting out from the nozzle during the time interval $\Delta t$), namely:

$$Q = c_{air}\rho_{air}d(T_{air}-T_0)V_{air}/v \qquad (6)$$

where $c_{air}$ and $\rho_{air}$ are the hot air heat capacity and the hot air density, respectively.

The best nozzle velocity *v* selected during the measurement conditions was equal to 4.8mm/s. (at the same time it is the speed of the OWIS PKTM 70 table).

The measurement consisted of the registration of the radiation intensity *I* as a function of the coordinate *z* value at scanning the sample surface along the *z* axis by the hot air nozzle. The FLIR SC7000camera registered the radiation generated by the heat trace during the scanning. The region on the surface ofthe heat trace is possible to be selected by the Altair software and the signal intensity associated with this region of a sample is displayed by this computer program after choosing the area of the heat trace. Thus, the registered magnitude *I(z)* is the radiation intensity generated by the selected area on the heat trace.

## 4. *Results and Discussion*

In Figs. 2 and 3 are presented the experimental curves of *I(z)* obtained at the above described experiment conditions. In Fig. 2a,b are presented the *I(z)*-curves obtained during scanning along the red line where the row of the holes is placed on the back side of the sample (see Fig.1b). The *I(z)*-curve in Fig. 2a was registered using the heat trace region shown in the insert. It can be seen that the *I(z)*-curve displays the maxima corresponding to the increased temperature in the area at the positions of defects (holes shown in Fig. 1b). Whereas, in case of the *I(z)*-curve obtained by using the IR-signal from the region *out of the heat trace* (see Fig. 2b), the intensity of the maxima at the positions of the largest holes are much smaller and no maxima are observed at the positions of the last two holes. It means that the detection of the hidden defects depends on the selected area which is the source of the IR-signal, namely: this area should belong to the heat trace caused by the nozzle.

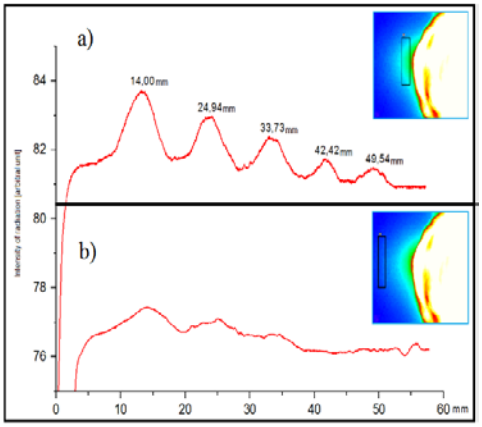



***Fig. 2*** *The I(z)-curves obtained at scanning along the red line (see Fig.2a): a) using the radiation from the region of the heat track, shown in insert; b) using the radiation from the region out of the heat track, shown in insert also.*

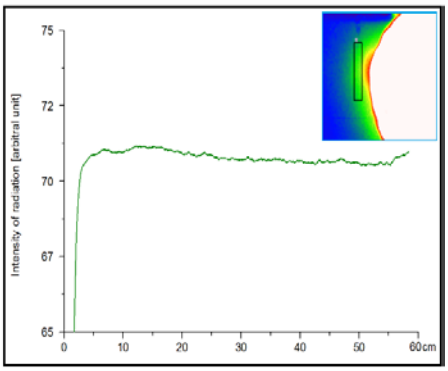



***Fig. 3.*** *The I(z)-curve obtained at scanning along the green line (see Fig.1b) using the radiation from the region of the heat trace, shown in insert*

In the Fig. 3 is shown the *I(z)*-curve obtained during scanning along the green line (see Fig. 1b) which is out of the holes row. No maxima are displayed on this curve.

In order to compare the results obtained using a hot air nozzle, the impulse of the xenon flash lamp as an excitation source was applied to the same sample. In this experiment the impulse with 6kJ energy and 6ms time generated enough power to register the temperature distribution on the surface of the sample and to visualize hidden defects by the IR camera. [13] After the excitation of the sample by the impulse from the xenon flash lamp the IR-camera registered from the back side of a sample only the first three largest holes. The last two smallest holes are invisible using this method. Whereas, scanning by the hot air nozzle allowed to detect all five holes, the minimal size of which was 2 mm. Thus, the proposed method of hot spot scanning is more effective for detection of defects smaller than 2 mm. The method described above enables to deliver energy directly to the defect area what causes higher sensitivity n the material ability to exchange heat with its surrounding determined by the thermal effusivity *e* (see Eqn. 1).

The Eqn. 1 points out that the highest temperature is in the region where more energy Q is delivered. If the nozzle is going along the larger defect, according to the Eqn. 6, the Q is larger too, because one is proportional to *d* – size of the defect. The minimal size of the defect detected by this method appears to be worth analyzing. A hidden hole (existing on the back side of another sample) with a diameter of 0.5 mm was detected experimentally. Theoretically, this minimal size can be calculated taking into account maximal sensitivity of the IR-camera to the temperature

change $\Delta T$ at the registration of the radiation intensity from the sample surface.
At the experiment conditions this maximal sensitivity should be 0.1K according to the documentation of the IR-camera. It is expected however, that the hole with a diameter of 0.2 mm could be registered using the proposed method at the conditions of this experiment.

## *5. Conclusion*

The proposed method of the noncontact and noninvasive control of hidden defects using the scanning hot air nozzle, enables to detect the holes existing on the back side of the steel plate (actually "a hidden defect") of $d \leq 2$mm size. The alternative noncontact and noninvasive method using the xenon flash lamp impulse as a source of excitation enables to detect the holes on the same steel plate with a diameter size of $d \geq 3.5$mm. Theoretically, the minimal size of such kind of a hidden defect which is possible to be detected using the proposed method, is 0.2 mm what will be verified in the future. Therefore, after application of the impulse thermography method for the macroscopic defect control, the some places where the defects of size less than 2 mm could be presented, should be verified by complementary thermography method using the scanning hot spot.

## *Additional information*

Financial support of Structural Funds in the Operational Programme - Innovative Economy (IE OP) financed from the European Regional Development Fund - Project "Modern material technologies in aerospace industry", Nr POIG.01.01.02-00-015/08-00is gratefully acknowledged.

**References**

[1] Vollmer M., Möllman K.-P.: Infrared Thermal Imaging, Wiley-Vch, N-Y, 2010.
[2] X. Maldague, *Theory and Practice of Infrared Technology for Nondestructive Testing*, John Wiley – Interscience, N-Y, 2001
[3] Burrows, S. E., Dixon, S., Pickering, S. G., Li, T. and Almond, D. P., 2011. Thermographic detection of surface breaking defects using a scanning laser source. *NDT & E International*, 44 (7), pp. 589-596.
[4] X. Maldague, S. Marinetti, Pulse phase infrared thermography, *J. Appl. Phys.*, 79 (5), pp. 2694-2698, 1996
[5] S. Marinetti, Y. A. Plotnikov, W. P. Winfree, A. Braggiotti, Pulse phase thermography for defect detection and visualization, *Proc SPIE* (1999).
[6] F. C. Sham, C. Nelson, L. Long, Surface crack detection by flash thermography on concrete surface, *Insight*, vol. 50, pp.240-243, 2008
[7] Masashi Ishikawa, Hiroshi Hatta, Yoshio Habuka, Ryo Fukui, Shin Utsunomiya, Detecting deeper defects using pulse phase thermography, *Infrared Physics & Technology* (03/2013; 57:42–49.
[8] Th. Zweschper, A. Dillenz, G. Riegert, G. Busse Ultrasound Thermography in NDE: Principle and Applications, *Acoustical Imaging* Volume 27, 2004, pp 113-120
[9] A. Gleiter, Ch. Spießberger, G. Busse, Lockin Thermography with Optical or Ultrasound Excitation, *Journal of Mechanical Engineering* 56(2010)10, 619-624
[10] K. Maś, M. Woźny, S. Prochorenko, K. Kashpor, E. Sheregii, „Sposób bezdotykowej kontroli jednorodności ochronnych powłok powierzchniowych, nr P.403346
[11] Carslaw, H.S. and Jaeger, J.C., Conduction of Heat in Solids, 1959 (Clarendon Press: Oxford).
[12] M. Pilla, M. Klein, X. Maldague A. Salerno, "New absolute contrast for pulsed thermography" in D. Balageas G. Busse, C. Carlomagno (Eds.), *Proc. QIRT (Quantitative Infrared Thermography)*, Dubrovnik, Croatia, 2002
[13] O. Wysocka-Fotek, W. Oliferuk, M. Maj "Reconstruction of size and depth of simulated defects in austenitic steel plateusing pulsed infrared thermography", *Infrared Physics & Technology*, 55 (2012) 363 – 367.

# BELT CONVEYOR DESIGN AND ANALYSIS

İ.Gerdemeli [1], S. Kurt [2] and E. T. Dayan[3]

[1, 2, 3] ITU Faculty of Mech. Eng., Mech. Eng. Department, Istanbul, Turkey.

***Abstract:*** *For handling of partial or continuous goods, belt conveyors are very efficient way. Belt conveyors are used in mining, iron and steel plants, thermal power plants, ore, coal, limestone, sinter transmission, automotive and the other sectors. There are several factors that have to be taken into consideration when a belt conveyor being designed. That means belt conveyor design process requires repetitive strength calculations. But analytical calculations are not capable of determine to entire stresses which occured at whole body. During the design process, time can be saved with the assistance of Finite Element Method. In this study; as a result, it has been seen that, F.E.M is the most practical method which can be utilized during belt conveyor design process.*

**Keywords**: BELT CONVEYOR, DESIGN, ANALYSIS, FINITE ELEMENT METHOD

## *1. Introduction*

In this study; belt conveyor which is carrying lignite and has 2.5m/s carrying velocity and 50 meters horizontal length was investigated. (250t/h capacity)

For this purpose, conveyor drums, shafts and belt were chosen by tables. As a first step of projection, belt width was described as 1 meter with using of slope angle of lignite and capacity of belt conveyor. Then, belt mass was taken from table for values of lignite's density and belt width. For idlers, values of mass, diameter and width were taken from table for belt width. With this values, weight of conveyor's moving parts were calculated.

As a second step, necessity of engine power was calculated after the calculations. Then, type of the motor drive was chosen as drive from head. For this selection, friction forces were calculated for idlers and belt. Also, the value of take-up force was described with friction forces which were calculated and the take-up was projected to be connected to tail pulley. Belt deflection was calculated analytically.

As a final step of projection, carcass of belt conveyor and number of plies were described. Then, axle diameters of idlers and pulleys were determined with tables. [1, 2, 3, 4, 5, 6] Also, head drive pulley's width was determined too. Head drive pulley's rotation speed was calculated and the reducer was chosen from the catalogue. [7] The conveyor which was designed during this study is shown in the figure below.



***Fig. 1*** Designed belt conveyor.

## *2. Analytical Analysis of the Belt Conveyor*

Belt conveyor has been analysed analytically, before it was analysed with finite element method. Firstly the total deformation of the belt conveyor was checked. After that, basic conveyor elements and their dimensions have been defined. For analysis of belt conveyor there was not a formula to determine all types of stresses. So, determining of occured stresses was difficult. Some empirical approaches were used to calculate stresses.

After all stresses were determined, shafts diameters were calculated for idlers and drums also bearings were chosen in accordance to idlers and drums diameters.[8]

***Equation 1:*** *Total deformation calculation formula.*

$$f \le \frac{L_T^{\,2}\left(G_B + G\right)}{8T_1} \cong 17.5mm$$

$L_T$ =1400mm, $G_B$ =15daN/m, $G$ =27.8daN/m, $T_1$ =900daN.

***Equation 2:*** *Stress calculation formula.*

$$\sigma_{\max} = \frac{(M_e)_{\max}}{I_x} y_{\max}$$

***Table 2:*** *Values for stress calculation.*

| Part name | $M_e$ [Nm] | $I_x$ [mm$^4$] | $y_{max}$ [mm] | $\sigma_{max}$ [MPa] |
|---|---|---|---|---|
| Idler | 114785 | $\frac{\pi(133^4-125^4)}{64}$ | $\frac{133}{2}$ | 2,26 |
| Idler shaft | 23485,40 | $\frac{\pi.25^4}{64}$ | $\frac{25}{2}$ | 15,31 |
| Tail pulley | 114711,19 | $\frac{\pi(320^4-300^4)}{64}$ | $\frac{320}{2}$ | 0,198 |
| Tail pulley shaft | 44205,04 | $\frac{\pi.20^4}{64}$ | $\frac{20}{2}$ | 56,29 |
| Take-up pulley shaft | 124078,10 | $\frac{\pi.30^4}{64}$ | $\frac{30}{2}$ | 46,8 |
| Diversion pulley | 127167,19 | $\frac{\pi(320^4-300^4)}{64}$ | $\frac{320}{2}$ | 0,174 |
| Diversion pulley shaft | 36180,07 | $\frac{\pi.20^4}{64}$ | $\frac{20}{2}$ | 46 |
| Head drive pulley | 210222,75 | $\frac{\pi(400^4-380^4)}{64}$ | $\frac{400}{2}$ | 0,180 |
| Head drive pulley shaft | 855000 | $\frac{\pi.70^4}{64}$ | $\frac{70}{2}$ | 26 |

## *3. Analysis of the Belt Conveyor with Finite Element Method*

The next stage of the study includes the analysis of the belt conveyor with finite element method. To be able to analyze the belt conveyor by means of this method, firstly 3D solid model of the belt conveyor must be generated.[9]

### 3.1 Modelling of Belt Conveyor

For the design of the belt conveyor, usage of one pulley for tail, one for head, one for take-up and three for diversion was decided. Thicknesses of pulleys were determined for all of them as ten millimeters. Also, usage of sixty seven idlers was decided for the design. Forty six idlers of sixty seven were used to support of belt. Thicknesses of idlers were determined as four millimeters for every idler. With the tables, thickness of the belt was calculated eight millimeters.

For the chassis parts of the belt conveyor, U160 profiles were chosen for main frame, U120 profiles were chosen for supports which are thirty six, and for the connections between main frame parts, square section eighty millimeters profiles were chosen which are forty two.

In this study SolidWorks 3D design software has been used for modelling the belt conveyor. All the belt conveyor components were modelled one by one, and then they were combined.

### 3.2 Analysis of the Belt Conveyor Using ANSYS FEA Software

After the design of belt conveyor, there was a necessity for the analysis of belt conveyor to be sure about the conveyor's safety and capability for usage. For this purpose, finite element method which is one of the realistic approaches to analyze stress, strain, deflection etc. was chosen.

Designed belt conveyor model was transferred to ANSYS Workbench to analyze the belt conveyor. Static structural mode was opened to make linear and static analysis for the conveyor. Engineering data were given to analyze. Then model was being prepared. For the preparation of the model, materials specifications were assigned firstly. Then contacts were determined and contact types were assigned. After that, the model was divided into 804828 elements and 2640145 nodes for application of finite element method. At this point, belt was thought to be shell, and the others solid. Meshed model is shown in figure 2.

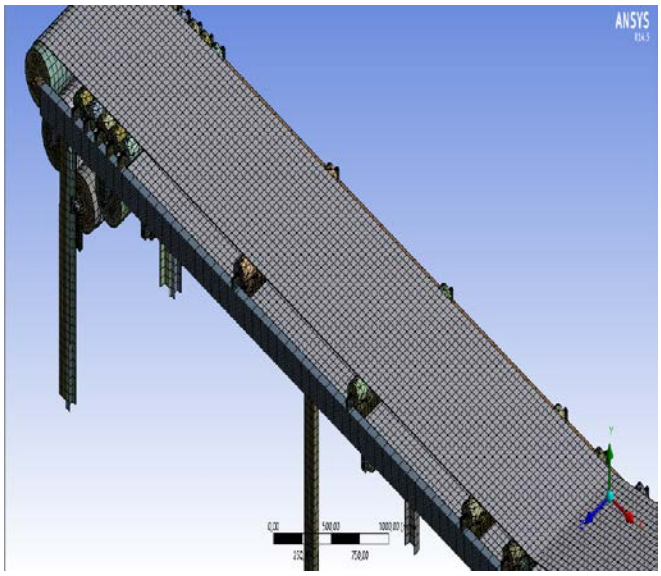



***Fig. 2*** Meshed model.

For finishing of the model preparation, all of the conditions were applied. Gravity were applied to all bodies, rotational velocity(120rpm) was applied to drive pulley shaft, weight of lignite(13900N) was applied to belt, take-up force(7050N) was applied to take-up pulley and finally, fixed supports were applied to all supports' bottom faces. Belt conveyor model is shown in figure 3.

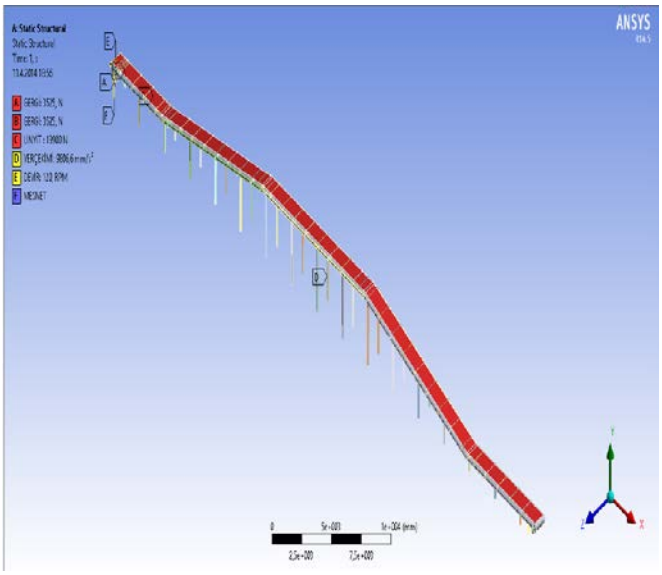



***Fig. 3*** Belt conveyor model.

## *4. Results*

The software was run with these boundary conditions and the load combinations mentioned above. According to this analysis, we can see that maximum total deflection (Fig. 4) is smaller than 17.5 mm which is calculated analytically.

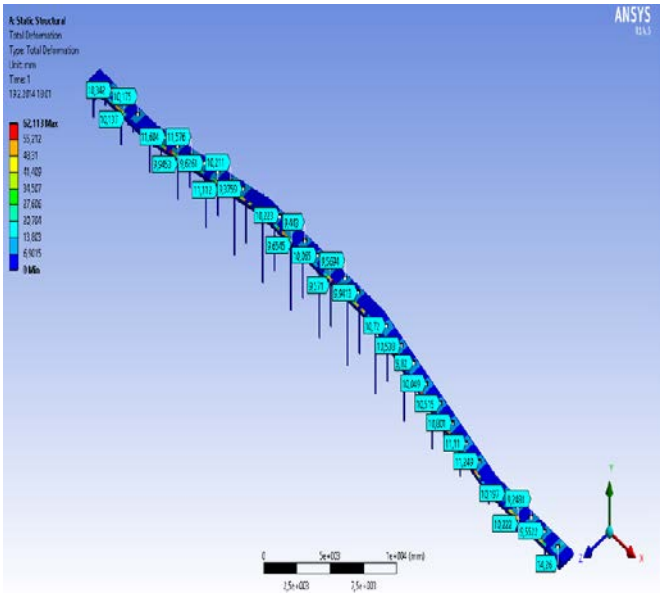



***Fig. 4*** Total deflection.

This result show us, if the analytical formula is customized for belt conveyor, results have proximity between analytical method and finite element method.

Unfortunately, at the belt conveyor topic, we have not any customized stress calculation for belt conveyor parts, only we have generalized stress calculation formula which comes from strength of materials approach.

Analytical approach results is shown in the table 1. For making a comparison between analytical approach and finite element method in this section, we need FEM results. So results are shown in Fig. [5-9]. From this results, we can see that some regions have stress concentrations which depend on design features. These

unpredictable stresses and hardnesses on calculation stage cause diffrences between analytical and FEM results.

Comparison between analytical approach and finite element method is shown table 2.

In accordance to these results, FEM is only way to determine all types of stresses which occur at belt conveyor parts.

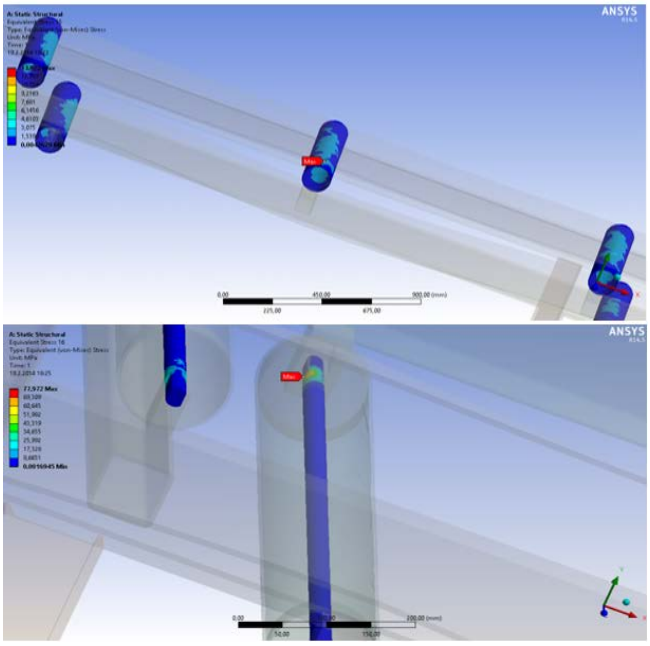


***Fig. 5*** Occurred stresses at idlers and idlers' shafts.

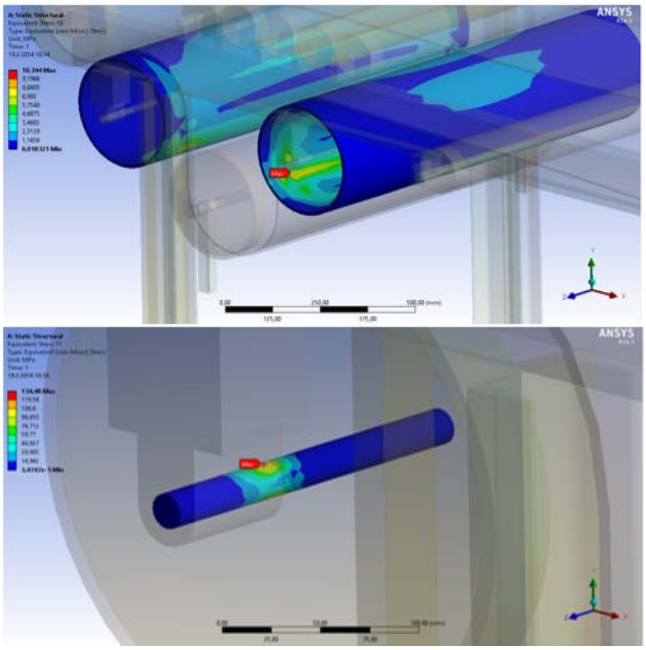


***Fig. 6*** Occurred stresses at diversion pulleys and diversion pulleys' shafts.

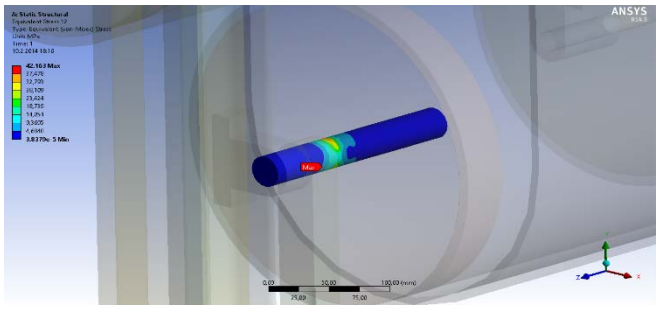


***Fig. 7*** Occurred stresses at take-up pulley's shaft.

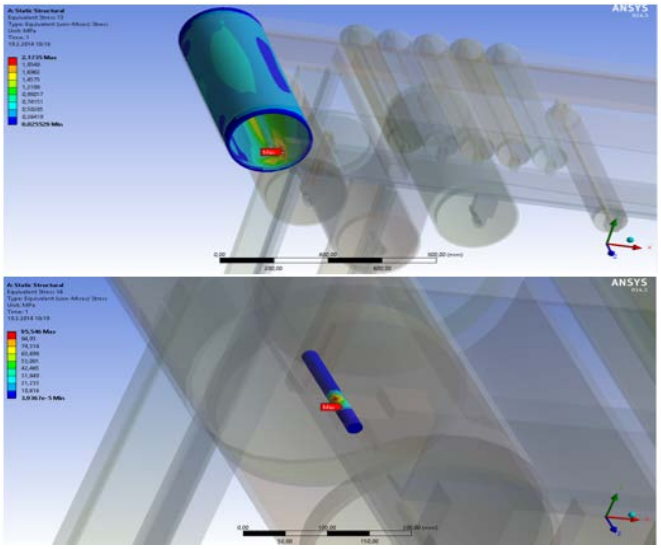


***Fig. 8*** Occurred stresses at tail pulley and tail pulley's shaft.

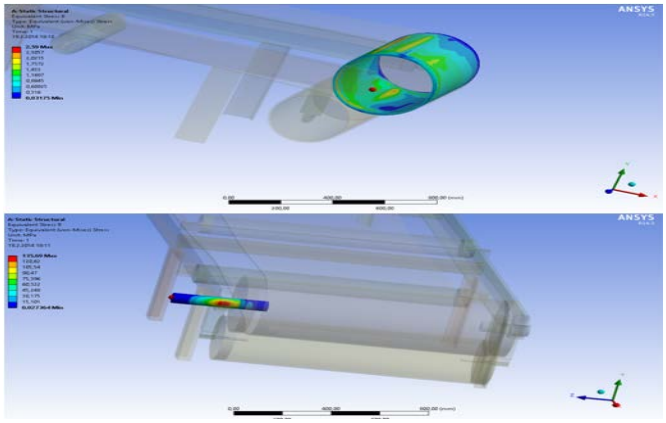


***Fig. 9*** Occurred stresses at head drive pulley and head drive pulley's shaft.

***Table 2:*** *Comparison between analytical approach and finite element method.*

| | Analytical Approach | Finite Element Method | |
|---|---|---|---|
| Part name | $\sigma_{max}$ [MPa] | $\sigma_{max}$ [MPa] | Difference (%) |
| Idler | 2,26 | 13,822 | 83,6 |
| Idler shaft | 15,31 | 77,972 | 80,3 |
| Tail pulley | 0,198 | 2,1735 | 90,8 |
| Tail pulley shaft | 56,29 | 95,546 | 41 |
| Take-up pulley shaft | 46,8 | 42,163 | -10,9 |
| Diversion pulley | 0,174 | 10,344 | 98,3 |
| Diversion pulley shaft | 46 | 134,48 | 65,7 |
| Head drive pulley | 0,180 | 2,59 | 93 |
| Head drive pulley shaft | 26 | 135,69 | 80,8 |

## *5. Conclusion*

During the design process of belt conveyors or the similar structures, it is not enough only system's being safe in terms of strength. The design must fulfil the minimum safety conditions and should be light and cheap as well. Therefore, to be able to reach the optimum design, system should be modified and revised numerous times.[9]

Calculating the system with analytical approaches causes design process to take long and inccorrect. In belt conveyor design process and the similar studies which require repetitive calculations, designers can save time by using finite element method. Constructor can change the model in computer environment and get the results of the new design via finite element method without wasting time. Also, this is the most practical and reliable way to reach the optimum design in terms of strength, weight and cost.[9]

## *6. References*


[1] Demirsoy, M., (2005), Transportation Technic, Vol 2. Birsen Yayınevi, İstanbul.
[2] Curgul, İ., (2010), Handling Technic. Birsen Publisher, İstanbul.
[3] Asik, E., Belt Conveyors. T.M.M.O.B. Mechanical Engineers Chamber, Ankara.
[4] CEMA. (2007), Belt Conveyors for Bulk Materials 6th Ed., Conveyor Equipment Manufacturers Association, USA.
[5] DIN 22101, February, 1982. Belt Conveyors for Bulk Materials - Bases for calculation and design. *DIN*.
[6] Gerdemeli, İ. , İmrak C. E. , Kesikci M. K. , (2005), Continuous Handling Systems. Birsen Publisher, İstanbul.
[7] Yılmaz Reducer, Product Catalogue.
[8] Skf Bearings, Product Catalogue.
[9]Gerdemeli I.,Imrak C.E, (2008) "Modeling of JIB Crane Construction Analysis with Finite Element Method", *The 13th International Conference on Problems of Material Engineering, Mechanics & Design*, 26-29 August 2008, Rajecke Teplice, Slovakia

# LATTICE (CAGE) BEAM DESIGN AND FINITE ELEMENT ANALYSIS OF GANTRY CRANE

İ. Gerdemeli [1], S. Kurt [2] and B. Bige[3]

[1, 2, 3] ITU Faculty of Mech. Eng., Mech. Eng. Department, İstanbul, Turkey.

***Abstract:*** *Gantry cranes are particularly suited to lifting very heavy objects, especially in shipbuilding industry are used massive objects like ships' engines to be lifted and moved over the ship. Capacity of the overhead gantry cranes increased proportionally through the needs. In this study dual-trolley heavy duty overhead gantry crane that can carry loads up to 800 tons was designed and analyzed. Stress and displacement values of main beam were calculated by both Finite Element Method and using mechanical formulas. As a result, it has been seen that, F.E.M. is a quite practical method to handle stress analysis problem of gantry cranes.*

**Keywords**: GANTRY CRANE, CAGE STRUCTURE MAIN BEAM, DESIGN, ANALYSIS, FINITE ELEMENT METHOD

## *1. Introduction*

Because of the fact that overhead gantry cranes are the structures, particularly designed according to the needs of the users, the parameters that are needed to be determined before the design. In this study a dual-trolley (2x400 tons) heavy duty overhead gantry crane that has 102 meters long cage structure main beam, 800 tons lifting capacity and 62 meters effective lifting height was designed and analyzed.

Classifications were made to determine coefficients to be used in analytical calculations by using FEM and DIN norms and the basic structural elements like ropes and pulleys were selected. All loads affecting the crane were determined by taking into consideration the chosen structural elements.

Occurring result of these affecting loads, maximum stresses were calculated analytically by using mechanical formulas. Calculated stresses were checked whether they are under allowable limits or not. For the case calculated stresses were over allowable limits the design was renovated and provided to remain under allowable limits.

All 3-D models were created with the help of the draft drawings which were formed by mechanical calculations and the selection of the structural elements. The gantry crane which was designed during this study is shown in the figure below (Fig. 1).

According to the various loading conditions the generated solid model was analyzed by the finite element method with the help of ANSYS Workbench 14.5.

Finally, the stress and displacement results obtained from analytical calculations were compared with the results obtained from the finite element program and percentages of errors were calculated.

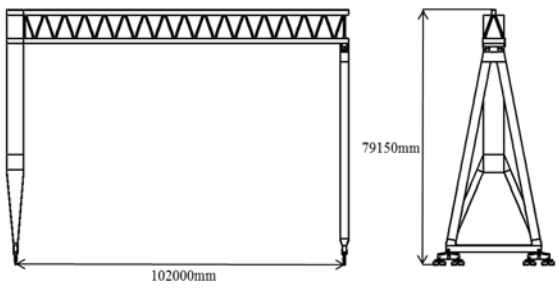



***Fig. 1*** *Designed gantry crane.*

## *2. Analytical Analysis of Gantry Crane*

The free body diagram of the main beam was created as shown in the figure below (Fig. 2). Trolley position creating maximum moment was used in our calculations to see the stresses in the worst case. The loads were increased by the proper coefficients to add dynamic effects. The total load affecting from trolley's wheels (P=5824882N) and the distributed load coming from weight (w=117384N/m) of the main beam were calculated. The maximum moment occurred at 46m far from rigid leg and the moments are calculated as shown in equations below.

***Equation 1:*** *Moment from the distributed load.*

$$M_{dis_{(46)}} = \frac{w.l.c}{2} - \frac{w.c^2}{2} = 151190592\,Nm$$

$l$ =102m, $w$ =117384N/m, $c$ =46m

***Equation 2:*** *Moment from the singular load.*

$$M_{snglr_{(46)}} = 2.P.\frac{c^2}{l} = 241675496.3\,Nm$$

$l$ =102m, $P$ =5824882N/m, $c$ =46m

Also moments coming from rope effect and trolley's braking force were calculated and all moments were summed. Finally, maximum stress values occurring on the main beam by result of total moment was calculated by using mechanical formulas. For the case calculated stresses were over allowable limits the design was renovated.

According to the maximum shear force occurring on the main beam, compressive and tensile forces affecting cross bars that are forming cage structure were calculated individually and then stresses on bars were calculated.

Consequently, displacement occurring on main beam by weight and lifting capacity were calculated. The displacement was checked that it is under allowable limits. Reverse displacement value that will be used at production was calculated.

## *3. Analysis of the Gantry Crane with Finite Element Method*

The next stage of the study includes the analysis of the gantry crane with finite element method which is one of the most common numerical methods that can solve many engineering problems. To analyze the gantry crane by this method, 3D solid model of gantry crane must be generated.

### 3.1 Modelling of Gantry Crane

All parts of the gantry crane were 3-D modeled by using the SolidWorks 2012 drawing program with the help of the draft drawings which had been formed by mechanical calculations and the selection of the structural elements. Then all modeled parts were assembled.

3D modeled gantry crane was shown in the figure below.



***Fig. 2*** *3D modeled gantry crane.*

### 3.2 Analysis of the Gantry Crane by Using ANSYS FEA Software

According to the various loading conditions the generated solid model were analyzed by the finite element method with the help of ANSYS Workbench 14.5 analyzing program. Loading conditions were created by taking maximum effects into consideration. For that reason for 4 different trolley position (left side, right side, center and maximum moment position) 8 different loading conditions were created and also for without trolley situation one more loading condition was created.

Static structural mode which allows static analysis with materials' linear behavior was used to analyze in ANSYS Workbench 14.5. In static analysis which is commonly used in engineering applications, it is thought that forces and supports are applied momentary and calculations are made for this moment. Dynamic coefficients to increase static forces and acceleration/braking forces were used to dynamic analyze in static structural mode.

To prepare finite element model, contacts were determined and *no separation* contact type for flexible joints and *bounded* contact type for fixed joints were assigned. Then the modeled body was meshed by using proper *sizing* as a result 836048 elements and 2492913 nodes were created. Meshed body was shown in the figure 3.

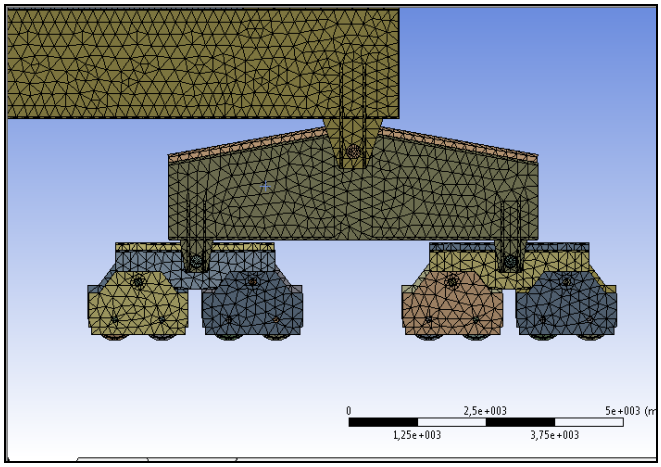



***Fig. 3*** Meshed model.

After meshed body was created, all of the loading conditions were applied. Earth gravity and acceleration coming from crane's move which equals to 1/30 of the crane's weight were applied to whole body. Working load (y direction) and the forces (x and z direction) coming from trolley's move which equals to 1/30 of the working load were applied to the touching points of the trolleys' wheels to the main beam. And also in the calculations the crane's wheels were considered fixed to the ground. Created finite element model was shown in the figure below (Fig 5).

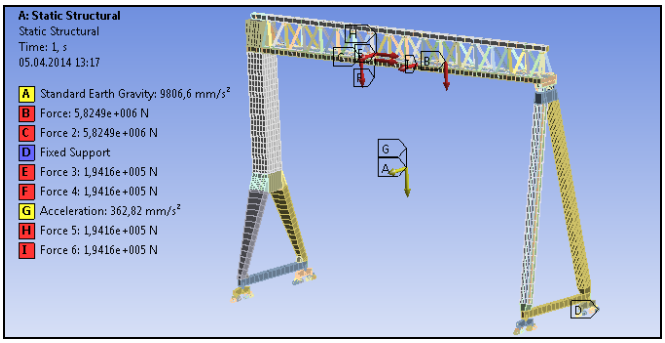



***Fig. 4*** *Finite element model.*

## 4. Results

From these static analysis, stress and displacement values on the crane body were obtained for all loading conditions. To obtain the exact deformation value of main beam, arithmetic mean value of legs' deformation was subtracted and the obtained value was checked that it is under allowable limits. The deformation value occurring as a result of the working load was calculated as 80.68mm. Exact value of deformation of the main beam was calculated as shown in the figure below by using formulas below.

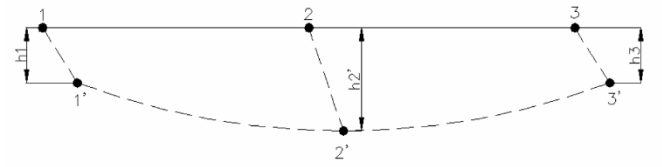



***Fig. 5*** *Deformation calculation.*

***Equation 2:*** *Exact deformation of the main beam.*

$$h_2 = h_2^{'} - \left(\frac{h_1 + h_3}{2}\right)$$

When evaluating the results of the finite element method, point defects occurring on generally corners were neglected. So, it's easily seen that maximum stress (172.67 MPa) occurred at upper beam.

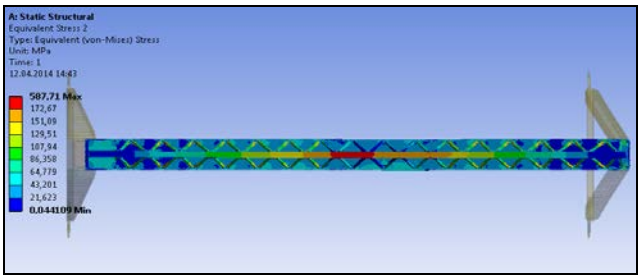



***Fig. 5*** *Stress distribution of main beam.*

When the result of stress distribution was examined in detailed manner, it was seen that high stresses occurred on some local zones at the balancing beams of carrying groups.

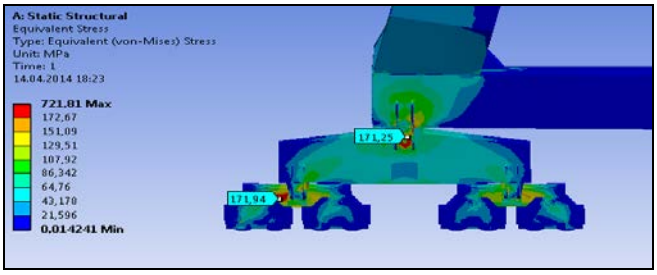



***Fig. 5*** *Stress distribution of carrying group.*

Finally, the stress values on main beam obtained from analytical calculations were compared with the results obtained from the finite element program and percentages of the error were calculated.

***Table 1:*** *Comparison between analytical approach and finite element method.*

| Loading Combination | Analytical Approach | Finite Element Method | |
|---|---|---|---|
| | $\sigma_{max}$ [MPa] | $\sigma_{max}$ [MPa] | Difference (%) |
| 110 | 56.43 | 53.08 | 6 |
| 121 | 134.34 | 142.07 | 6 |
| 122 | 90.43 | 94.78 | 5 |
| 123 | 134.75 | 145.7 | 8 |
| 124 | 86.86 | 89.56 | 3 |
| 131 | 169.56 | 171.91 | 1 |
| 132 | 116.22 | 113.35 | 2 |
| 133 | 170.66 | 172.67 | 1 |
| 134 | 107.6 | 104.32 | 3 |

The basic reasons of the difference occurring between mechanical calculations and finite element method are the acceptances in creating mechanical model and the mathematical approaches in finite element method.

## *5. Conclusion*

It was concluded that St 52-3 which has 210 MPa tensile strength is the proper material for the main beam. Determining nodal stresses provided us that dimensions and thicknesses at excessive safe areas to be simplified in order to reduce the manufacturing cost and at unsafe areas to be strengthened. As a conclusion, finite element method is a very effective and useful way to see applicability of design of gantry crane.

### *6. References*


[1] Bayvas, M.Ş., (1987). General Mechanic, Turkish National Education Association, Istanbul.
[2] Kocaturk, T., (2008). Static Notes. YTU, Istanbul.
[3] Gerdemeli, İ., İmrak, C.E., (2008). Transport Technique Symposium Notes, ITU.
[4] Gerdemeli, İ., (2008). Advance Transport Technique Notes, ITU.
[5] F.E.M., (1987). 1001 3. Association 1987.10.01
[6] Oztepe, H., (1999). Transport Technique, Istanbul.
[7] Curgul, İ., (2010), Transport Technique, Birsen Association, Istanbul.
[8] Suner, F., (1981), Lifting and Handling Equipment, Istanbul.
[9] Kurt, S., Kutay, G.M., Aslan, R., (2008). Steel Construction At Cranes, Vol. II. Chamber of Mechanical Engineers Association, Ankara.
[10] Topcu, M., Tasgetiren, S., (1998), Finite Element Method For Engineers, Faculty of Engineering Association, Denizli.